

Sama Saeid

MODELING OF PROPAGATION AND MEASUREMENT OF NEURONAL ACTION POTENTIALS IN 3D

Master of Science Thesis
The Faculty of Medicine and
Health Technology
Examiner: Jari Hyttinen
Examiner: Pasi Kallio
April 2020

ABSTRACT

Sama Saeid: Modeling of Propagation and Measurement of Neuronal Action Potentials in 3D
Master of Science Thesis
Tampere University
Master's Degree Programme in Biomedical Sciences and Engineering
April 2020

In the past decades, several methods have been developed which facilitate the culture, isolation, and investigation of neuronal networks in vitro. Neuronal networks provide an accessible and economical chance to study complex emanating properties that simulate brain physiology. Micro-electrode array (MEA) technology has emerged into a generally used and powerful methodology to analyze neural network activity. Computational modeling provides an extensive toolset for designing and interpreting neural recording devices. Modeling allows effective examination of large parameter spaces, for which laboratory research would not be feasible. A few studies have been performed in simulating the action potential propagating in an axon and its coupling with the electrodes, however, electromagnetic simulation based comparisons of the standard planar MEA and the 3D MEA by using finite element method have not been published prior to this work.

The objective of this work was to compare the standard 2D MEA and the newer 3D MEA by and interpret the potential factors affecting the recorded signal. The finite element method was used to simulate the propagating action potential along the axon and MEAs coupled to the axon and cell growth medium. Commercial computational software COMSOL, which provides an approximation of finite element method was employed. This software provides a chance to calculate the extracellular field potential distribution around the activated axon and simulate the recorded signals by planar and 3D MEAs from the surrounding environment. FitzHugh-Nagumo equations were used for simulating the traveling pulse along with the axon and other AC/DC modules utilized to define the enclosing domains. The geometrical effect of the standard planar MEA and the newer 3D MEA as well as, various parameters affecting the final recorded voltage have been assessed in detail.

The result of the FitzHugh-Nagumo 3D axon model is quite comparable to the Hodgkin-Huxley action potential model. Furthermore, the simulation results of the MEAs provide detailed spatial and temporal information about the electrical behaviour of the extracellular environment. As it has been observed in the other experimental results, this model also demonstrates that the physical configuration and biological environment of the microelectrodes play a vital role in the results of the neuronal recording. These results confirm the inverse proportion between the electrode-neuron distance and amplitude of the recorded voltage, and the inverse relationship between the surface area and the magnitude of the detected AP. Furthermore, the recorded signals from the multiple axons by considering were been assessed. The results demonstrate complex recorded compound AP waveforms and revealed that the neuronal population can influence the amplitude and shape of the detected signals. It is shown that the fact that 3D microelectrodes have a larger surface area and spatial recording leads to higher voltage averaging from the extracellular medium. This issue demonstrates as the lower amplitude of the recorded APs compared to the planar microelectrode.

Keywords: MEA technology, finite element method, microelectrode array, 3D MEA, neural recording, computational modeling.

PREFACE

This thesis study was conducted in computational biophysics and imaging group at Tampere University. I would like to express my deepest gratitude to Academy Professor Jari Hyttinen for giving me the opportunity to work and study at the group, thank you for your guidance, advice, discussions, kindness and support. Adj. Prof. Jarno Tanskanen, Dr. Kerstin Lenk, M.Sc. Barbara Gennoch are acknowledged for help, advice, and encouragements.

Finally, I would like to thank my family and friends for their motivation and support during the journey of my master thesis work.

Helsinki, 8th April 2020

Sama Saeid

CONTENTS

1. INTRODUCTION	1
2. THEORETICAL BACKGROUND	3
2.1 Nerve cell.....	3
2.2 Cell Membrane.....	4
2.3 Transmembrane and Resting potential	5
2.4 The activation of nerve cell and propagation	7
2.5 Hodgkin-Huxley model	9
2.6 FitzHugh-Nagumo model	11
2.7 Recording techniques	12
2.7.1 Planar MEA.....	14
2.7.2 Pillar 3D MEA	17
2.7.3 Medium-electrode coupling	18
3. FEM SIMULATION AND METHODS	21
3.1 FitzHugh-Nagumo Model of action potential	21
3.2 Simulation of multi electrode arrays	24
3.2.1 Planar MEA.....	25
3.2.2 Multiple axon in the MEA	30
3.2.3 3D MEA	30
4. SIMULATION RESULTS.....	33
4.1 F-N model of action potential	33
4.1.1 3D simulation	33
4.2 2D F-N simulation	37
4.3 Neurons coupled to planar MEA	38
Distance effect	41
4.3.1 Multiple axon.....	42
4.4 3D MEA	45
4.4.1 Electrode geometry effect	46
4.4.2 Distance effect	50
4.4.3 Multiple axon.....	52
5. DISCUSSIONS	55
6. SUMMARY	58
REFERENCES.....	60

LIST OF FIGURES

Figure 1. Main parts of a neuron.	3
Figure 2. Cell membrane structure. [Art]. In thoughtco. Obtained from https://www.thoughtco.com/cell-membrane-373364	5
Figure 3. Diagram of action potential in the neuronal membrane from a resting voltage of -70 mV to +40 mV[47].	8
Figure 4. Hodgkin-Huxley electrical circuit model describing the giant squid axon membrane. V_{Na} , V_K , V_L are the calculated Nernst voltages of sodium, potassium, and chloride (leakage) respectively. g_{Na} , g_K , g_L are the ionic conductivities (ion permeability of the membrane) which are functions of time and transmembrane potential except G_L that taken as constant [58][24].	9
Figure 6. (A) Planar microelectrode recoding neuronal activity. (A) Extracellular microelectrodes at a distance from the active neurons record the action potentials propagating along the axon. The effect of the volume conductor on the extracellular field potential can be seen in this panel. The potential near the microelectrodes can be assessed utilizing volume conductor theory. (B) Scanning electron micrograph of a neuron on a planar MEA. (C) A typical signal recorded from a microelectrode exhibiting spiking activity. The red line illustrates the threshold for detecting spikes (Adapted from [97][6][71]).	15
Figure 7. Illustration of a 3D MEA with straight pillar electrodes. (a) Fabrication of conductive polymer 3D pillars by utilizing titanium/Au-coated microscope slides for photolithographic patterning of each single electrode, onto which conductive polymer is direct write printed. (b) printed 3D MEA. (Adapted from [101] with permission from RightsLink).	17
Figure 8. Medium-electrode interface for a planar microelectrode. Voltage source V_e , which is the average of the surrounding extracellular potential resulting from neuronal activity, is transformed by the electrode-medium impedance called effective electrode impedance Z_e' and the effective input impedance of the amplifiers Z_a' and final measured voltage is V_{rec} . In this model, R_{spread} is the spreading resistance inside the medium, R_e and C_e are the resistance and capacitance of the double electric layer at the medium-microelectrode interface, R_s and C_s are the shunt resistance and capacitance, and R_m is the resistance of the microelectrode (Adapted from [71]).	18
Figure 9. Geometrical model of the axon used in the simulation.	22
Figure 10. Geometrical model of the axon and extracellular medium.	23
Figure 11. Schematic illustration of a 60-electrode MEA layout of a (model 60MEA200/30iR-Ti, Multi-Channel Systems MCS GmbH) from [126].	24
Figure 12. Geometry of the simulated planar MEA and cell culture medium. Close view of the single planar microelectrode demonstrated inside the box.	25
Figure 13. The Geometry of the simulated axon coupled to the MEA.	26
Figure 14. Boundary conditions in different component of the system. Gray color shows the insulation condition and the blue components are defined by distributed impedance condition.	27
Figure 15. Electrical model of the electrode-medium coupling. R_s is the medium resistance, Z_{Elec} is the complex impedance of the electrode-	

medium coupling, and Z is the distributed impedance on the surface of the axon (Adopted from [127]).	28
Figure 16. Element quality histogram of the discretized model.	29
Figure 17. Mesh model of the axon coupled to the MEA and medium.	29
Figure 18. Model of the multiple axon inside the neurochip.	30
Figure 19. Interfacing neuron-laden medium with 3D MEA electrodes (Adapted from [101])	30
Figure 20. Geometry of the simulated 3D pillar electrode MEA and an axon.	31
Figure 21. Closeup view of the FEM model. Element color denotes the element quality based on skewness.	32
Figure 22. Simulated AP pulse on the membrane of the axon.	33
Figure 23. Detected AP at three different points along the axon as the AP propagated through the axon.	34
Figure 24. 2D plot of the axon and the electrical field in the extracellular medium due to AP propagation.	34
Figure 25. AP propagation in an axon (left column) and extracellular field potential (right column) at different times.	35
Figure 26. Membrane voltages based on the amplitude of the applied stimuli.	36
Figure 27. Series of action potential on the axon simulated by MATLAB.	37
Figure 28. Simulated planar MEA coupled to the axon and the extracellular field potential caused by an AP.	38
Figure 29. (a) Y-X cut plane view of the MEA dish with microelectrodes shown as small rectangles coupled to the axon and medium, and the electrical field potential generated by an AP moving to the right. (b) The axon membrane potential and the recorded electrical potential in the extracellular medium due to an AP.	39
Figure 30. Z-Y view of field potential due to AP propagation along the axon simulated in different time points along with isopotential lines. In (a), the reference electrode is marked red.	40
Figure 32. Effects of distance from the axon to a planar microelectrode. The horizontal distance effects on the simulated AP recorded at the microelectrode	42
Figure 33. Z-Y view of the two-axon system coupled to MEA.	43
Figure 34. Simulated measured signals of two axons by different planar microelectrodes. These plots illustrate the recorded signals by corresponding electrodes seen in Figure 32.	44
Figure 35. Signal recorded by the electrode A and the membrane voltages the axon 1 and axon 2.	45
Figure 36. Space view of the 3D MEAs coupled to axon-laden solution.	46
Figure 37. Extracellular electrical field around a single microelectrode due to an AP in an axon. (a) voltage distribution around the planar microelectrode, (b) voltage distribution around the 3D pillar microelectrode.	47
Figure 38. Comparison of the simulated voltage recorded at a single 3D pillar and planar microelectrodes of different surface areas, along with the membrane potential.	48
Figure 39. Iso-surface plot of electrical field in the MEA due to AP in the axon. (a) 3D pillar MEA, (b) planar MEA.	49
Figure 40. Geometry effect of the microelectrodes on the recorded data from AP in an axon. Recorded signal by 3D pillar microelectrode in the MEA dish and the corresponding planar microelectrode recording along with the membrane voltages.	50
Figure 41. Distance effect of the axon from 3D MEA. Plot (a) depicts the effect of vertical distance from the axon to the electrodes and figure (b)	

	<i>shows the effect of horizontal distance on the obtained voltage by the microelectrode</i>	51
Figure 42.	<i>A simulated recorded signal by the 3D pillar microelectrode A (Figure 42) and the corresponding membrane voltage in the axon 1 and axon 2.....</i>	52
	53	
Figure 43.	<i>Two axons coupled to a 3D MEA with pillar electrodes, and the simulated electric field potentials due to the APs. The simulated recordings via the electrodes A, B, C, and D are shown in Figure 43.....</i>	53
Figure 44.	<i>The simulated recorded signals by the 3D pillar electrodes marked in Figure 42 for the two-axon simulation.</i>	54

LIST OF SYMBOLS AND ABBREVIATIONS

FEM	Finite element method
F-N	FitzHug-Nagumo
H-H	Hodgkin and Huxley
MEA	Microelectrode array
CNS	Central nervous system
PNS	peripheral nervous system
AP	Action potential
SNR	signal to noise ratio
HD-MEA	High density MEA

V_m	membrane voltage
W	recovery variable
V_K	Nernst voltage

1. INTRODUCTION

Neurophysiological studies have supreme prominence in explaining the underlying properties and behaviours of the neurons, enhancing the knowledge of the nervous system[1]. Neuronal cultures have continued to be a powerful model for investigating the central nervous system, especially the healthy or diseased human brain[2][3]. Furthermore, brain slices or cultures of dissociated neurons have provided new insights into numerous brain diseases and allowed an accessible, economical, and less complex surrogate for in vivo brain experiments[3]. These biological models offer a more flexible environment for various studies such as drug testing, toxicity testing, and developing functional organs [2][4]. Since 1950s, there is challenge in the neuroscience to reach a high throughput and high-resolution device for observation and manipulation of the neuronal network[1][5]. Microelectrode arrays (MEA) are an essential means in analyzing the electrophysiology of the brain in vitro and used to characterize the cultured neuronal networks[6][7][8]. This tool allows non-invasive recording of electrical signals from neuronal networks[9]. MEAs help researchers to understand brain functioning by investigating the electrical activity of the single cells and the whole population of the cells [10][11][9]. For the first time in 1972, Thomas et al. designed the MEA and used the 30 electrodes array to record the embryonic chick cells[12][1]. Substrate-integrated microelectrodes record the electrical voltage from the extracellular environment simultaneously through a large arranged array of individual electrodes[13][14][15]. Despite the pervasiveness of MEAs, nevertheless, there is a deal of mystery about how to make them efficient and how to explain the signals they record[16]. The targets in making the high throughput MEAs are considered as selectivity, low impedance, High resolution, low signal to noise ratio(SNR)[16]. For this issue, several designs of MEAs have been manufactured consisting of both metallic and nonmetallic components in order to be used as neuronal interfaces[1]. Lately, It has been demonstrated that the structure, surface modifications, surface chemistry, and biotechnology can enhance the performance of the MEAs noticeably[1].

The quality of the MEA recordings is one of the significant factors that define the prosperity of each experiment[6]. Furthermore, this success happens when the networks of neurons are active, and the electrodes are acting efficiently in recording the signals[6]. Appropriate electrical models are required to verify the design of modern microelectrode

arrays[11]. Computational modeling yields an extended toolset for designing and understanding neuronal interfaces [17]. The finite element method (FEM) Modeling supports the effective examination of large parameter spaces, where clinical research would not be achievable[17]. Moreover, 3D FEM modeling can provide a simulation of MEA based on the measurement environment and allow the researcher to interpret the recorded data concerning the measurement geometry [18]. Some research was performed in modeling microelectrode devices [18] and their coupling with active neurons[19][20][21].

Nevertheless, in the literature, nothing mentioned about the comparison of the planar MEA and three-dimensional MEA and studying the factors affecting the recorded voltage in 3D models. This work attempts to interpret how the geometry, neuronal distance and population can change the signals detected by these two types of MEAs in 3D models.

The approach of this thesis was to compare the standard 2D MEA and the newer 3D MEA by utilizing FEM modeling and assess the potential factors influencing the final recorded voltage. Initially, AP propagation along a single scaled axon was simulated based on the FitzHug-Nagumo (F-N) model in COMSOL. Later, a system comprising of an MEA and an axon was simulated. To define the electrical conductivities of the practiced materials and the proper boundary conditions in the medium-electrode interface, electric current physics was employed in COMSOL. The comparison of the planar and 3D MEA based on the geometry effect was accomplished and further studies regarding the physical and biological environment of the microelectrodes were presented.

2. THEORETICAL BAGROUND

2.1 Nerve cell

In living tissue, significant communication control is performed by hormones and nerves[22]. Nerves are fast prewired point-to-point data carriers, whereas hormomes act on a slower time scale and in a broadcast fashion[22]. Neurons are the fundamental units of complex nervous systems [23]. Heinrich Wilhelm Gottfried Waldeyer applied the term *neuron* to the neuronal cell for the first time in 1891 and August Forel, Wilhelm His, and Santiago Ramón y Cajal revealed that the neural cell is the basic component of a neuronal system [24].

There are various types of nerve cells, which perform a diversity of functions in different parts of the nervous system. The major parts of a neuron are the cell body (soma), many short processes (dendrites), a single extended nerve fiber (axon) and chemical or electrical connectors (synapses) (Figure 1). Moreover, neurons exhibit a wide diversity in shape, size and electrochemical properties. Cables containing bundles of axons are called nerves [23].

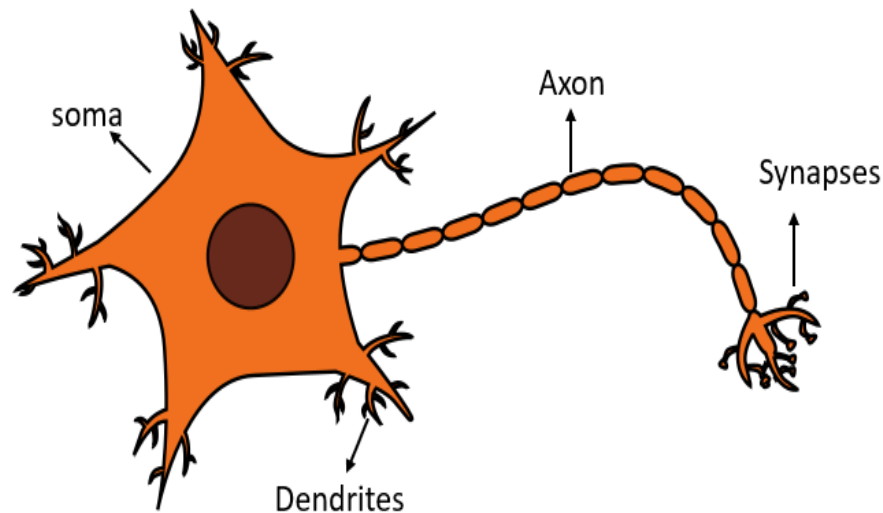


Figure 1. Main parts of a neuron.

The body of a nerve cell is similar to those of all other eukaryotic cells and internal features are nucleus, mitochondria, endoplasmic reticulum, ribosomes, and other organelles which are bond by membrane [25] [26]. Nerve cells are composed by about 70 - 80% of water, whereas the dry material is about 80% proteins and 20% lipids [25]. The organelles or other interior structure sustain all primary life processes as well as support

the functions of receiving, conducting, and forwarding electrochemical signals [25]. The dendrites receive impulses from tens or even hundreds of thousands of neurons and transfer them to the cell body. These impulse can be excitatory or inhibitory[27]. The axon conducts the signal from the cell body to other nerves. Mammalian axons are about 1 - 20 μm in diameter and they may be several meters in length [24].

In some neurons, axons may be covered with an insulating layer called the myelin sheath, which was first observed by Theodor Schwann in 1838 [24]. The myelin sheath, which is composed of lamellar membranes and it plays a key role in the fast propagation of neuronal impulses in the both peripheral nervous system (PNS) and central nervous system(CNS) [28]. Furthermore, the myelin sheath is not continuous, and it is intersected by unmyelinated parts called nodes of Ranvier. Nodes of Ranvier are responsible for the typical fast impulse propagation through saltatory conduction from node to node. this event was observed for the first time by the French anatomist Louis Antoine Ranvier in 1878 [29] [24]. Myelin sheath which is formed by glial cells (oligodendrocytes), efficiently isolates the axon, decreases the transmembrane capacitance, and thus also current leakage [30][31][28].

2.2 Cell Membrane

The cell is surrounded by a plasma cell membrane whose thickness is about 7.5 - 10.0 nm [24]. Cell membrane controls the movement of substances in and out of the cell and its structure and composition resemble a soap-bubble film (fatty acids) [32]. Two layers of lipids (fatty acids) which enclose the cell are called phospholipids [22](Figure 2). The heads of these molecules, the phosphoglycerates, are hydrophilic (attracted to water) and in contact with extra and intracellular fluid [23][24]. The membrane fatty acids have tails containing hydrocarbon chains, which are hydrophobic (water repelling) and pointed toward the middle of the membrane in the intracellular fluid [23]. There are macromolecular protein pores (also called voltage dependent ion channels) embedded on the phosphide bilayer, which are the important part of the cell membrane based on the bioelectric viewpoint and shunt pathway with the bilayer lipid membrane [22][24]. Moreover, the extracellular and intracellular fluid of the cells generally contain some ions which Na^+ , K^+ , Cl^- and Ca^+ are main ions capable of transmembrane flow [24]. Nodes of Ranvier are 1 μm wide which is the lowest involvement to the axonal landscape[33][34]. Nonetheless, the nodes of Ranvier have major effect on neurotransmission due to high densities of voltage dependent Na^+ channels up to 1400 channels per μm^2 [28][35][36].

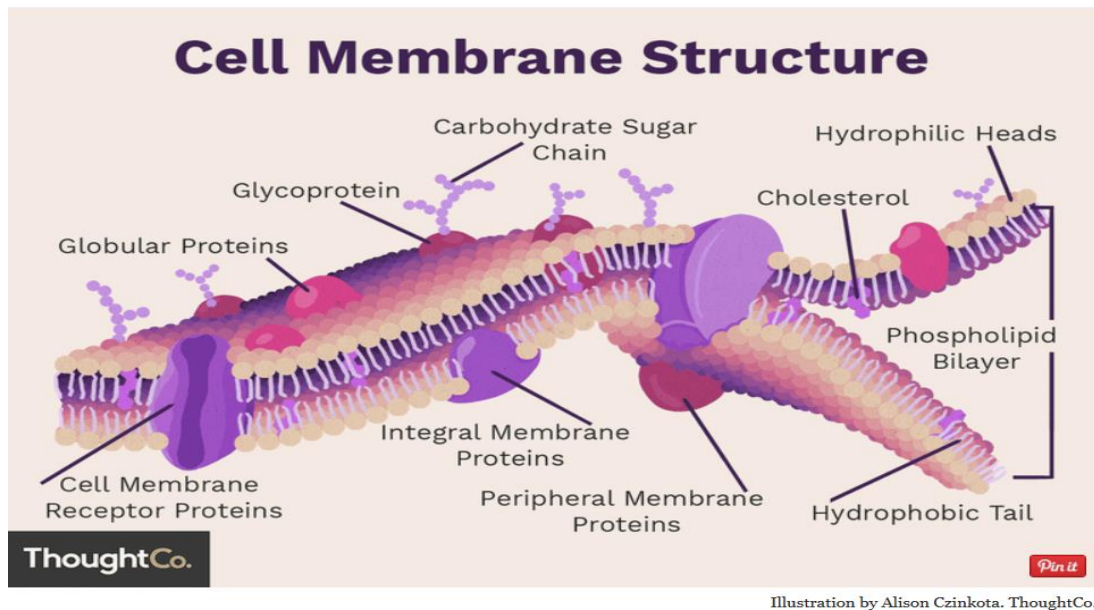


Illustration by Alison Czinkota. ThoughtCo.

Figure 2. Cell membrane structure. [Art]. In thoughtco. Obtained from <https://www.thoughtco.com/cell-membrane-373364>.

2.3 Transmembrane and Resting potential

The cell membrane plays a key role in generating the bioelectrical function of an excitable cell by regulating the movement of ions between the extracellular and intracellular regions. It has been proposed that changes in the cell membrane charge may assist the recruitment of signalling molecules to the inner leaflet of the membrane in cell receptors micro clusters [37] [38]. This issue may leads to a significant impact on cell motility and cell invasiveness, cancer propagation, apoptosis and scar development [39] [40] [41]. The concentration of sodium (Na^+) ions in the extracellular fluid of the cells is approximately 10 times higher than the intracellular fluid [24]. On the other hand, potassium (K^+) ions' concentration is 30 times higher inside the nerve cells [24]. Moreover, chloride (Cl^-) ions is at high concentration in the extracellular region and low inside the cell [23]. The cell membrane receptor proteins acts as selective transporter to these ions [23]. The ease with which, or more specifically, the rate at which an ion traverses the membrane is called the *membrane permeability*, which differs among ion species. Ion-selective properties and activation mechanisms of the ion channels embedded in the membranes affect the ionic composition inside and outside the cell [42]. Also, the concentration gradients of ions across the membrane contribute to the ion movement through the cell membrane [24]. This phenomenon is called ion diffusion and the result of this flow is the tendency of ions to store inside or outside regions of the cell [24]. Accumulation of ions on different sides of the membrane leads to *membrane potential*, which is defined as the

potential at the inner surface relative to that at the outer surface of the membrane (1) [23][24] [42]. The magnitude of the transmembrane potential depends on the membrane selective properties as well as ion concentration in both sides of the membrane [43].

$$V_m = (\Phi_i) - (\Phi_o), \quad (1)$$

In this equation, V_m is the membrane voltage, Φ_i is the inner surface potential and Φ_o is the outer surface potential. In the movement of ions the diffusional force as well as electric field force should be considered and the equilibrium is obtained when the diffusional force counteracts the electric field force for all ions [24]. At this point, which is called resting potential or Nernst potential, the net flow of a specific ion is zero [24]. In a resting state, the intracellular region of a neuron is negatively charged relative to the outside region, which leads to resting transmembrane potential around -75 mV, which varies for different types of cells [23][2].

As it mentioned before, the relationship between the membrane potential and ionic flow is of great significance. For a membrane that is permeable just only to one specific ion, equilibrium state needs that the force due to the electric field be to the opposite direction and equal in magnitude with the force due to diffusion [24]. Nernst equation demonstrates the equilibrium voltage based on the given ionic concentrations [24]. Equation (2) is the Nernst equation derived by Walther Hermann Nernst in 1888 and by allocating 37 °C for the temperature, given in Kelvin, and ± 1 for the valence [44]. In this equation V_k is the Nernst voltage [V] across the membrane, R is the gas constant [8.314 J/(mol·K)], T is the absolute temperature [K], z_k is the valence of the k^{th} ion, F is the Faraday's constant [96485 C/mol], $c_{i,k}$ is the intracellular concentration of the k^{th} ion, and $c_{o,k}$ is the extracellular concentration of the k^{th} ion [24].

$$V_k = \frac{-RT}{z_k F} \ln \frac{c_{i,k}}{c_{o,k}} \quad (2)$$

However, not only the assumption that the cell membrane is permeable to single ion is not valid, but also low permeability may have important effect [24]. For this issue, the straightforward extension of the Nernst equation has been derived, called *Goldman-Hodgkin-Katz* equation, which gives the steady-state value of the membrane potential when there are other types of ions in the intracellular and extracellular regions (see equation 3) [24].

$$V_m = -\frac{RT}{F} \ln \frac{P_K c_{i,K} + P_{Na} c_{i,Na} + P_{Cl} c_{o,Cl}}{P_{o,k} c_{o,k} + P_{o,Na} c_{o,Na} + P_{Cl} c_{i,Cl}} [mV] \quad (3)$$

where V_m denotes the transmembrane potential, C_i is the measurable intracellular ionic concentration, C_o is the measurable extracellular ionic concentration, and P is the permeability constant of an ion.

Based on the equation (2) the resting potentials of sodium and potassium ions are respectively 55 mV and -75 mV. Due to high concentration of Potassium ions inside the cell, the resting potential across the membrane is considered to be -70 mV [23].

2.4 The activation of nerve cell and propagation

Bioelectrical sensitivity of living organisms initiates from selective membranes [42]. Neurons can react to stimuli (such as touch, sound, light, and so on), transfer impulses, and communicate with each other and with other types of cells like muscle cells [45]. These stimuli directly or indirectly affect the ion channels, transporter or in the other way pump activation/inhibition [46]. This issue leads to transiently change in ion-specific permeability of the membrane and membrane potential variation [46]. This stimulation can be *excitatory* or *inhibitory*. For an excitatory (*depolarizing*) stimulus, a change of the potential happens inside the cell region compared to the outside region in the positive direction as well as a reduction in the resting voltage [24]. On the other hand, for an inhibitory stimulus (*hyperpolarizing*) an alteration happens in the potential inside the cell compared to the outside fluid in the negative direction which leads to an escalation in the magnitude of the membrane voltage [24]. If the excitatory stimulus is sufficient for the specific neuron, membrane depolarization causes the membrane potential to reach a threshold potential, and the membrane produces a rapid rise and fall of membrane potential, which is called *nerve pulse*, *spike* [23]. The recorded electrophysiological data from the neuronal pulse is called the *action potential (AP)* [24]. In this work, AP refers also to a simulated recording of a neuronal pulse. An AP exhibits depolarization from the resting potential to a peak and decays back down to the equilibrium resting voltage in the repolarization phase [47] [42] (Figure 3). This reversal of polarity moves through the cytoplasm and activate the voltage dependent sodium channels along the length of the nerve fibre [48]. This Signal can propagate through the long axons, allowing conduction of information from sensory organs to the brain [47]. Furthermore, it is considered that the AP follows an all-or-nothing law and has a specific form regardless of the magnitude of stimulus [46] [42]. APs propagate systemically with a regenerative property and a specific velocity [48] [49] [46] [50]. When the stimulus reaches the dendrites of the neuron, and the threshold voltage dependent Na^+ channels become fully activated and the Na^+ influx develops the internal fluid of the cell [2] [48]. This issue reverses the polarity and cause more positive potential

in the inside region of the cell [48][2]. Accordingly, this activation process leads the membrane voltage to change from -70 mV to peak value up to $+40$ mV [51].

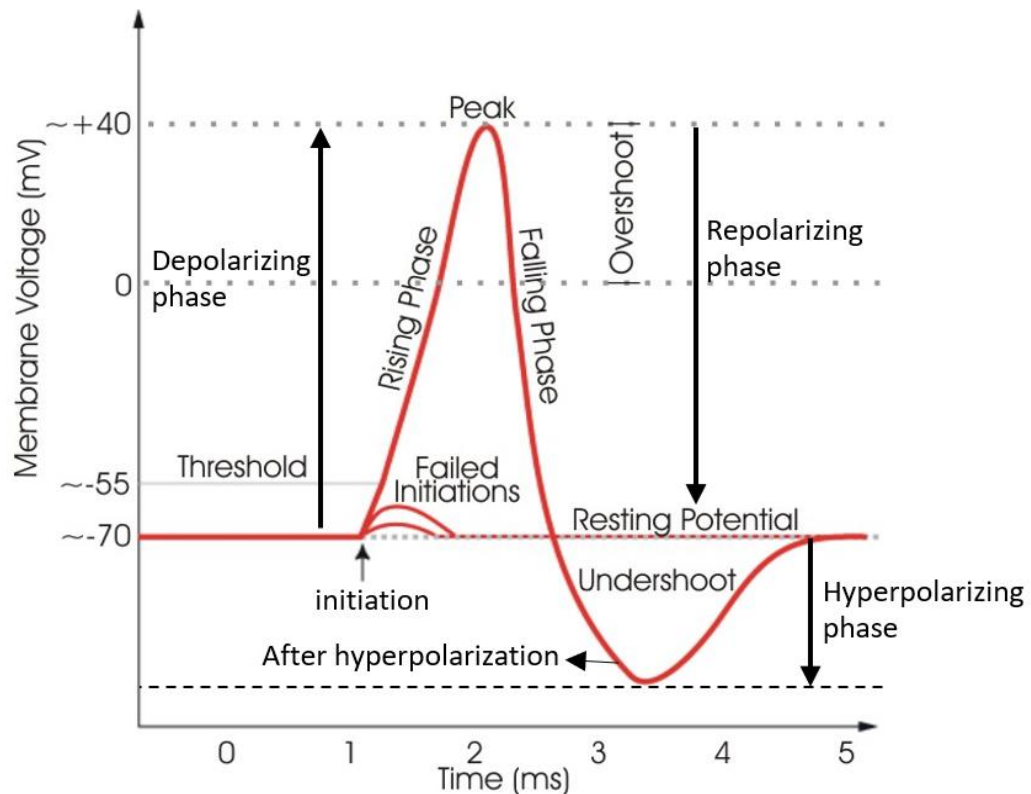


Figure 3. Diagram of action potential in the neuronal membrane from a resting voltage of -70 mV to $+40$ mV[47].

The part of an action potential above the 0 mV is recognized as *overshoot* [47] (Figure 3). The approximately $+30$ mV is close to the Nernst potential for Na^+ corresponding to electrochemical equilibrium with the membrane completely permeable for Na^+ [48]. Following sharp upstroke activation, a slower recovery phase to restore the resting potential starts when the intercellular potential reaches approximately $+20$ mV and voltage dependent K^+ channels are slowly increasing the permeability [47][42] [24]. K^+ flow from inside to outside of the cell and the closing of Na^+ channels serve to stabilize the transmembrane potential [52] [28]. Potassium ion channels have small effect on repolarization owing to their slow kinetics of activation whereas, have an effect on the characteristic after hyperpolarization formed when the repolarized transmembrane voltage exceeds the resting voltage (Figure 3)[53][52][28]. In the repolarization phase, membrane potential may also undershoot to more a negative voltage than the resting potential before returning back to the resting voltage (Figure 3)[47]. This undershoot is called *afterhyperpolarization* [47]. Another important point about the inactivation of Na^+ voltage dependent channels is that the channels will not reopen until the transmembrane voltage returns back to the resting potential [54].

2.5 Hodgkin-Huxley model

Already based on the early studies on neuronal activity, it has been known that the recorded action potentials are dependent on the influx of Na^+ and efflux of K^+ [55][56]. The landmark voltage clamp experiments of the Hodgkin, Huxley, and Katz on the giant squid axon were the basis of the first model for neuronal cell membrane excitation under both subthreshold and suprathreshold situations [51][24][57]. Their model describes the ionic basis of neuronal activity. Hodgkin and Huxley received the Nobel Prize in Physiology or Medicine in 1963 [24] and Katz in 1970. Their analysis supports the presence of independent potassium and sodium channels [51]. The Hodgkin-Huxley model simulates the current (I_m) passing through the cell membrane; the model is a *parallel conductance* model and includes four current elements: current which is carried by Na^+ ions (I_{Na}), current conducted by K^+ ions (I_K), capacitive current (I_C), and the current which is carried by the other ions (I_L)(leakage current) (Figure 4) [24][58]. In this model, the lipid membrane is modeled as an isolator which acts as a capacitor C_m [23].

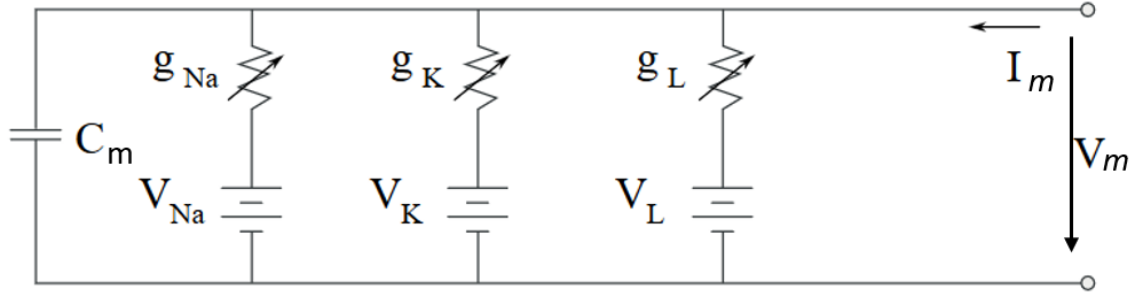


Figure 4. Hodgkin-Huxley electrical circuit model describing the giant squid axon membrane. V_{Na} , V_K , V_L are the calculated Nernst voltages of sodium, potassium, and chloride (leakage) respectively. g_{Na} , g_K , g_L are the ionic conductivities (ion permeability of the membrane) which are functions of time and transmembrane potential except G_L that taken as constant [58][24].

By employing the Kirchhoff's law on this circuit, the time-dependent membrane current can be obtained (4)[58].

$$I_m(t) = C_m \frac{dV_m}{dt} + g_{Na}(V_m - V_{Na}) + g_K(V_m - V_K) + g_L(V_m - V_L) \quad (4)$$

As it mentioned, g_{Na} , g_K are the conductance of the ion channels and they can be characterized based on the m , n , and h which are called *gating variables* (equation 5,6)[59][58]. Each of these variables defined in the simple linear equations (equation 7)[23].

$$g_{Na} = \bar{g}_{Na} \cdot m^3 \cdot h \quad (5)$$

$$g_k = \bar{g}_k \cdot n^4 \quad (6)$$

$$\frac{d\omega}{dt} = \alpha_\omega \cdot (1 - \omega) + \beta_\omega \cdot \omega \quad , (\omega \text{ is } m, n, h) \quad (7)$$

In these equations, \bar{g}_k and \bar{g}_{Na} are constant, α_ω denotes the rate of transfer from outside of the membrane to intracellular medium whereas, β_ω denotes the rate to the opposite direction for the same ion [58]. The cable theory considers the axon as series of upper RC network models which are distributed uniformly[60]. By combining equation 4 with the cable theory, the concluding equation for the even propagation of the neuronal pulse can be calculated (8) [60][59][58].

$$\frac{a}{2R_i} \frac{\partial^2 V_m}{\partial x^2} = C_m \frac{dV_m}{dt} + g_{Na}(V_m - V_{Na}) + g_K(V_m - V_K) + g_L(V_m - V_L) \quad (8)$$

In this equation R_i is the resistance of the intracellular medium, a is the radius of the axon[60].

The Hodgkin-Huxley model and other models that calculate the action potential can be expressed as equation 9 and 10 by assuming distance and time as dimensionless variables x and T [60]. These variables can be calculated by dividing exact distances by a specific length or space constant and an RC time constant respectively [60].

$$\frac{\partial^2 V_m}{\partial x^2} - \frac{\partial V}{\partial T} = f(V, M_1, \dots, M_n) \quad (9)$$

$$\frac{\partial M}{\partial T} = f_i(V, M_1, \dots, M_n) \quad \text{for } i=1, \dots, n \quad (10)$$

Although the Hodgkin-Huxley model provides a broad range of information from squid axons such as propagation and the shape of the pulse, this model has complexity and 10 differential equations [23][60]. Besides, this model needs three extra variables ($M_i = m, n, \text{ and } h$) which rise the computational times and power in the simulation software[60][61]. Several simplified models are widely employed in modelling the neuronal network such as FitzHugh-Nagumo, which only utilizes two variables in the mentioned equations (8) and (9)[60][61][62][63].

2.6 FitzHugh-Nagumo model

The FitzHugh-Nagumo (F-N) model is one of the popular standard models for APs utilized in computational and theoretical neuroscience studies [63][64][65]. FitzHugh et al. established the two-dimensional (two variables in the system) neuronal model of the basic qualitative characteristics of neuronal oscillations by utilizing the simple polynomial ordinary differential equations (ODEs) instead of complicated ODEs of the Hodgkin-Huxley (H-H) model [61][65][58]. Their discussion was built on the point that the time scale for the gating variables (m , n , and h) in the H-H equations were not all of the same order, therefore, the four variables of the H-H model could be ordered into a two-variable (V , ω) model (FitzHugh is also called the Bon Hoeffler-Van der Pol model)[63].

Equations 11 and 12 can be utilized for mathematically revealing the reaction-diffusion systems for wave propagation in excitable media [66][67][62].

$$\frac{\partial u}{\partial t} = f(u, v) + D_U \nabla^2 u \quad (11)$$

$$\frac{\partial v}{\partial t} = g(u, v) + D_v \nabla^2 v \quad (12)$$

In these equations, u and v are dependent variables, ∇ is the Laplacian operator, D_U and D_v are diffusion coefficients of two elements, $g(u, v)$ and $f(u, v)$ are the functions which governing the kinetics of the reaction [66]. By eliminating the diffusion of v and normalizing D_U , FitzHugh-Nagumo equations (13 and 14) can be obtained, which are utilized extensively for modelling the reaction-diffusion systems and usually for modelling the propagation of the action potentials in the neuronal tissues [62][68][69].

$$\frac{\partial V_m}{\partial t} = V(a - V)(V - 1) - W + \nabla^2 V \quad (13)$$

$$\frac{\partial W}{\partial t} = \varepsilon (V_m - b - cW) \quad (14)$$

In this model, V simulates the membrane voltage and also is called excitation variable, W is the recovery variable which imitates the outward currents [61]. ε is excitability and commonly is accepted to be constant, a is the excitation threshold where $0 < a < \frac{1}{2}$, $\nabla^2 V$ is the diffusion expression, and b, c are the system parameters influencing the dynamic of the model [23][64].

2.7 Recording techniques

Neuronal networks perform intricate operations which arise from the orchestrated interactions of different neurons [14]. Neurons receive inputs from other neurons, and encode and relay the data from the soma by propagation of action potentials along the axon [14] to the synaptic terminals, and thereafter to subsequent connected neurons. The extracellular field potentials (also called local field potentials) manifest the spike activity of different neurons, synaptic potentials, superposition of action potentials, and slow glial potentials in time and space [70]. It is amenable to record the electrical fields and signals on the electrodes at distances from the source due to the electrical nature of the neuronal activity [71]. Besides, the amplitude range of the field potential varies between 10 μV to 1 mV, therefore, great computational power is needed to acquire the information and classify the recorded voltage [72][73]. Changes in the membrane potential can be measured by recording the voltage between an extracellular microelectrode in the vicinity of the neuron and a reference electrode, which is further away [47]. Extracellular recording is a non-invasive tool which supports long term recording despite of poor quality recorded signals [1][70][13].

MEAs allow us to monitor neuronal activity with high time resolution and over extended periods of time. Research methods include recordings of spontaneous activity, electrically stimulated activity, and activity of neurons exposed to chemical compounds, e.g., for drug screening and toxicology [1][4]. Thomas et al. designed the MEA for the first time in 1972 [12]. Thomas et al. utilized 30-electrode MEA to record the embryonic chick heart cells [1]. Thereafter, Gross succeeded to record action potentials from dissociated brain ganglia of the snail *Helix pomatia* by utilizing MEAs with 36 microelectrodes [74]. Pine correlated the intracellular and extracellular processes in 1980 from the rat superior cervical ganglion cells by employing the MEAs in a study of extracellular and intracellular signal [7]. Consequently, this successful effort allowed MEAs to become an accepted electrophysiological method to analyze neurophysiology and neuropharmacology [1][75], and MEAs have been used to study the pharmacological and toxicological effects of the several compounds on the electrical activity of the neuronal networks [4].

Substrate-integrated microelectrodes record the electrical changes from the extracellular medium simultaneously through a large arranged array of individual metal electrodes both *in vivo* and *in vitro* applications [4] [14] [76]. This recorded data can be acquired across the morphology of the nearby neuron and from the other cells [71] [76]. Commercially available MEAs are a well-known technology for studying the electrical activity of neuronal networks. However, MEAs do not target the individual networks and they still suffer from the poor spatial resolution and low signal-to-noise ratio (SNR) [77][78][79].

MEAs can be used to study the electrical activity of neurons either acutely, for instance from the retina or tissue slices, or during prolonged culturing, e.g., to study network maturation over several weeks [4]. A MEA system can be connected to a stimulus generator in order to record evoked neuronal activity and analyze synaptic plasticity [80][81][82][83][84].

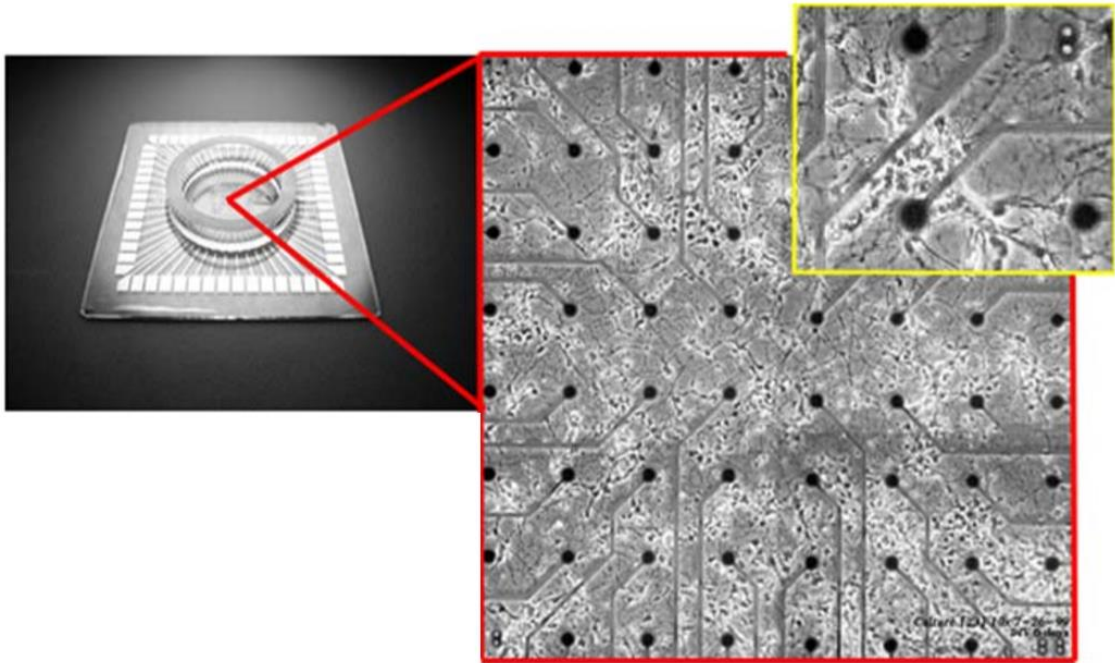


Figure 5. A planar MEA with an integrated culture dish. The glass-integrated MEA is surrounded by medium that contains rat cortical neurons (Adapted from[85]).

Moreover, the recording proficiencies, restrictions of the used device, and the factors affecting the recorded signals should be highlighted to understand how the neuronal signal is transduced to the final output [71][14] [27]. For instance, the magnitude of membrane voltages, polarity, and the position the neuronal cell with respect to the location of the microelectrodes have strong effect on the dissimilarities of the amplitude and the shapes of the recorded extracellular signal [14][15][29]. In order to investigate and manipulate the neuronal networks and individual neurons, CMOS (complementary metal oxide semiconductor) high-density microelectrode arrays (HD-MEAs) are being utilized for high spatiotemporal resolution [86][87][88][77]; HD-MEAs may consist of over 10,000 electrodes [89][90][77][6][87][70]. The quality of electrical stimulation and recording with MEAs depends on the electrical coupling coefficient between the neurons and microelectrodes, and SNR remained low [70]. In [53], action potential propagation and *in vitro* recording by various types of MEAs is discussed deeply.

Various design of MEAs have been fabricated consisting of either metallic and nonmetallic components to be used as neuronal interfaces [1] (Figures 6 and 7). Recently, It has been shown that the structure, surface modifications, surface chemistry, and the biotechnology can improve the performance of the MEAs noticeably [1]. Commercially available MEAs have been constructed mainly of a glass plate or “chip” and an integrated array of microelectrodes, which have been photoetched, insulated from each other, and coated with conductive materials [4] to improve electrode impedance beyond that achieved by the electrode base conductor material alone. One of the crucial issues in designing MEAs is selecting the materials for the insulator, conductor, and electrode and the selected materials should be tested for the toxicity and biocompatibility for extended periods of time [1], alike for implants [91]. For fabricating microelectrodes, many materials such as gold, stainless steel, platinum, tungsten, iridium oxide and titanium nitride have been employed [92][1].

MEA technology allows platform for simplified model of the neuronal network in the order of a single cortical column rather than a comprehensive brain [1]. Before the any biological experiments, the type of MEA should be considered [86]. For instance, if a MEA is employed for the stimulation, the charge capacity of the electrodes is a vital aspect and the electrodes should be able to facilitate the reactions in the interface of the electrode-medium in order to tolerate the ionic flow in the medium towards the targeted cells [93].

2.7.1 Planar MEA

Typical planar MEA electrodes are made of nontoxic and high corrosion resistance metal and their electrode diameters range from 10 to 30 μm implemented on grid of 0.2-2 mm^2 [4][1]. As the size of neuronal cells is of the order of micrometers or tens of micrometers in diameter, the mostly used fabrication method for the MEAs is microfabrication. During the last 45 years several microfabricated planar MEAs have been reported for extracellular recordings and stimulation [94][95][96].

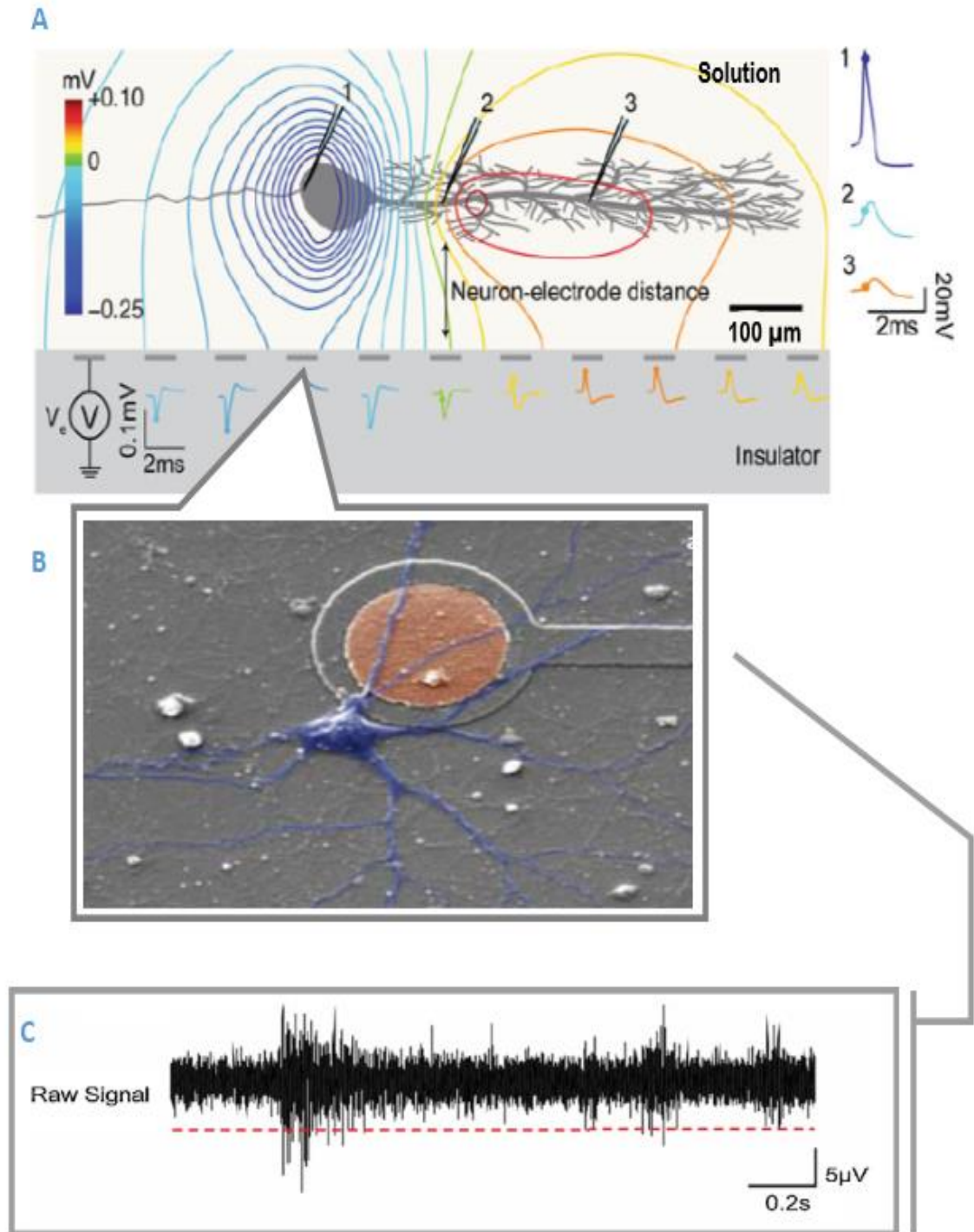


Figure 6. (A) Planar microelectrode recoding neuronal activity. **(A)** Extracellular microelectrodes at a distance from the active neurons record the action potentials propagating along the axon. The effect of the volume conductor on the extracellular field potential can be seen in this panel. The potential near the microelectrodes can be assessed utilizing volume conductor theory. **(B)** Scanning electron micrograph of a neuron on a planar MEA. **(C)** A typical signal recorded from a microelectrode exhibiting spiking activity. The red line illustrates the threshold for detecting spikes (Adapted from [97][6][71]).

Generally, these type of microelectrodes include an integrated cell culture dish and are utilized, for example, to understand neuronal activity and the plasticity of the networks [6]. For isolating the microelectrodes from each other as well as cell culture medium, organic or non-organic materials such as silicon oxide, silicon nitride, polyamide, or epoxy resin have been used [6]. Based on the application and goal of the measurements, MEAs with different numbers, sizes, and arrangements of microelectrodes can be used [4]. Leads of microelectrodes are, for example, embedded on glass wafer substrate in order to see the cultured cells using light microscopy [1]. Each microelectrode is connected to contact pad at the border of the chip with a thin conductor lead, and via the contact pad to an external amplifier in order to transmit the signals to an amplifier and analog-to-digital converter, and thereafter to a computer for further processing, e.g., filtering, signal detection, sorting, and other possible analysis [4]. Moreover, the instrumentation systems are also used in the multichannel analog and digital signal processors due to the multiple electrodes[6].

Usually, before plating the cells on the MEAs, the glass substrate is coated with the common substances such as polylysine, laminin, and collagen in order to escalate the sealing resistance between the glass and culture medium and improve the cell attachment and growth [6][1]. Sealing resistance is noteworthy in the stimulation of the neuronal culture as it decreases the stimulation threshold [98]. This glass substrate contains 1 to 100 microelectrode sites which are implemented in 100 μm distance per each other [1]. Monolayer of cells can grow on the top of the planar MEA and later, they can be removed from the chip for reusing the MEA several times in future by applying special maintenance [4].

Important information regarding the neuronal networks' structure and function can be acquired by MEA technique by revealing the spatiotemporal aspects of the electrical activity of the neurons [4]. For instance, rate of the action potentials (spike rate), rate of groups of intense spiking (burst rate), burst duration, interspike and interburst intervals and the number of spikes in each burst can be assessed from the neuronal MEA [4]. Mentioned parameters can provide information regarding the drug and chemical influences on synchronicity, consistency of oscillation, network connections, and burst structure [4]. Synchronicity and oscillation of the electrical activity of a neuronal network are also important characteristic phenomena, and the effect of the substances on these phenomenon is a subject of numerous studies [4].

2.7.2 Pillar 3D MEA

In the recent years, dissociated neuronal cultures have become widespread in the physiological research owing to their high performance in electrical recording, stimulation, imaging, and pharmacological manipulation compared to the in vivo models [99]. 3D pillar MEAs [94] have been utilized in the neuronal recording and stimulation due to the insufficiency of the planar MEAs in recording or stimulating 3D cell constructs such as tissue slices or 3D dissociated cultures. This limitation happens due to the reduction of the electrical signals from the neurons as the distance between the cell and microelectrode is large when measuring 3D cultures with 2D MEA [94], unless cell density is sufficiently high. Pyramid-shaped 3D MEAs can penetrate better to the neuronal cultures and tissue slices which leads to the high amplitude and SNR in the recorded signals [84][100]. Also straight pillar electrodes have been proposed [101]. For example, the height and diameter of the 3D pillars can be 80 μm and 14 μm , respectively, allowing for the high aspect ratio of 5.7 for the mechanical solidity [101]. Mechanical stability is necessary to sustain the exposure of the pillars to, e.g., a biogel and the cell culture medium, and to maintain the interactions between the pillars and the cells [101].

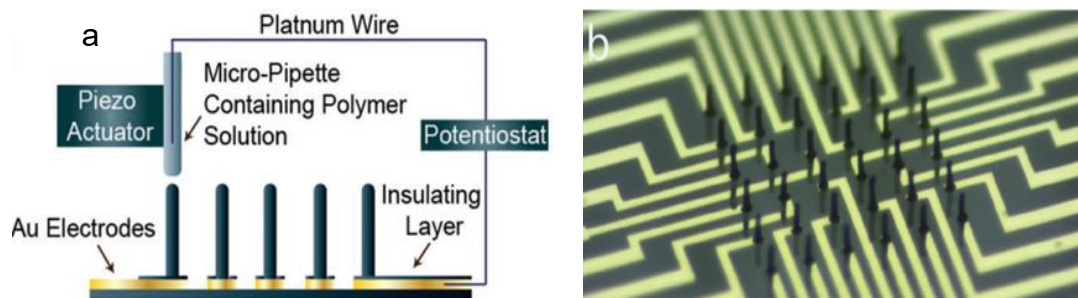


Figure 7. Illustration of a 3D MEA with straight pillar electrodes. (a) Fabrication of conductive polymer 3D pillars by utilizing titanium/Au-coated microscope slides for photolithographic patterning of each single electrode, onto which conductive polymer is direct write printed. (b) printed 3D MEA. (Adapted from [101] with permission from RightsLink).

Beside the three-dimensional microelectrodes provide a larger surface contact to the medium compared to the planar 2D MEAs [96]. Moreover, recorded voltage is the spatially averaged voltage of the extracellular medium surrounding the microelectrode [19]. In the recent research, it has been demonstrated that by applying some specific conductive polymer the electrochemical behavior and electrical performances of the 3D pillars are enhanced noticeably [101][102][103] (Figure 7).

2.7.3 Medium-electrode coupling

Although MEAs are usually used for recording the electrical signal, they can turn out to be to a part of the extracellular medium during the neuronal growth phase [6]. After a few days to weeks that the neurons are cultured on the MEA, new developed condition inside the dish can have an influence on the recording performance of the microelectrodes [6]. For instance, growth of neuronal somata, which includes extension of axons, development on the surfaces which have tight coupling to the rough and adhesive surfaces [6][104]. On the other hand, growth of supporting astroglia in the cultures can insulate neurons from the microelectrodes or can couple them tightly [105]. The first model for the interface between microelectrodes and neurons was proposed by Robinson in 1968 [106]. This model has been modified later for substrate integrated MEAs in order to compare the electrodes with field effective transistor-based devices in the simulations by Grattarola and Martinoia in 1993 [107]. The point contact model, which assumes a tight seal between the neuron and microelectrode, was proposed in 1997 by Weis and Fromherz [108]. However, in the real situation, that tight contact between the neurons and extracellular planar electrodes does not exist and microelectrodes sometimes record electrical field potential changes from neurons that do not have tight seals with and are located far from the microelectrodes, as observed in acute tissue and in vivo experiments [1][109].

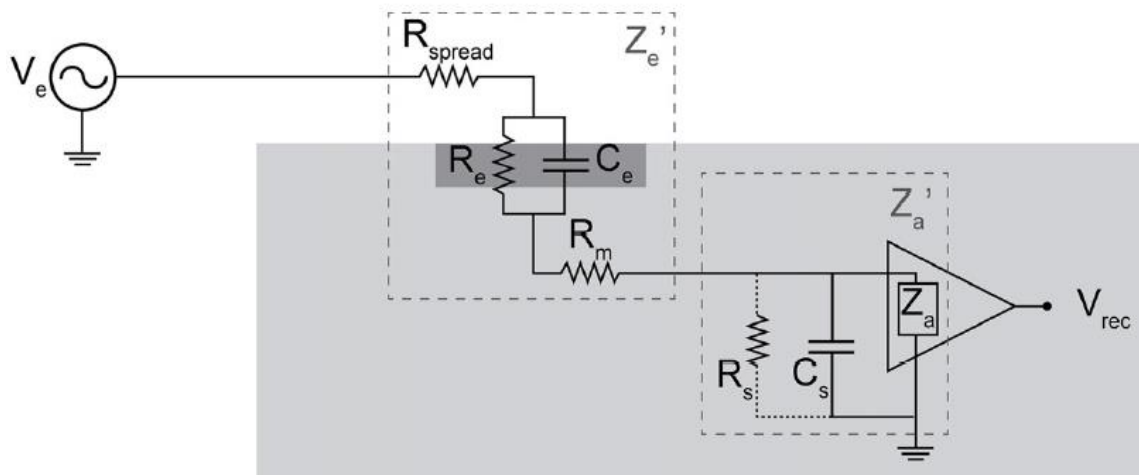


Figure 8. Medium-electrode interface for a planar microelectrode. Voltage source V_e , which is the average of the surrounding extracellular potential resulting from neuronal activity, is transformed by the electrode-medium impedance called effective electrode impedance Z_e' and the effective input impedance of the amplifiers Z_a' and final measured voltage is V_{rec} . In this model, R_{spread} is the spreading resistance inside the medium, R_e and C_e are the resistance and capacitance of the double electric layer at the medium-microelectrode interface, R_s and C_s are the shunt resistance and capacitance, and R_m is the resistance of the microelectrode (Adapted from [71]).

Figure 8 depicts the generalized model of the interface through which a microelectrode can record the average voltage inside the extracellular medium based on the volume conductor theory, and models also how the detected voltage is influenced by the characteristic of the interface [71][106][110][27][111]. The extracellular space is considered as homogenous, isotropic, resistive medium with respect to the volume conductive theory, Kirchhoff's current law or based on the Ohm's law and charge conservation [27][71]. Moreover, recorded signals from various locations of the active neurons show differences in the waveforms due to the source contributions biased contrariwise proportional to their distances [27] (Figure 6A). For a single point current source, equation 10 can be rewritten based on the Maxwell's equations of electromagnetism with respect to the Laplace boundary condition, which holds for the voltage at the microelectrode (V_e) [27][71][112][113].

$$V_e = \frac{I}{4\pi\sigma r} \quad (15)$$

In this equation I is the source point current, r is the distance between the microelectrode and point source, and σ is the conductivity of the extracellular medium. Since the membrane currents are distributed over the cable-like morphology of the neurons, method of the mages is applied to the equation (15) to obtain the V_e at each microelectrode (equation 6)[71][114].

$$V_e = \frac{I}{2\pi\sigma} \sum \frac{I_n}{r_n} \quad (16)$$

In this equation, $n = 1 \dots N$, is the number of each point source, I_n is each point current source, and r_n is the distances between the each point source and the microelectrode [71]. V_e is obtained at different locations of the microelectrode and then averaged. Consequently, if the electrode surface area is larger, the averaging effect is higher at each microelectrode [115].

Figure 8 depicts the electrical circuit model for the medium-microelectrode interface which is adapted from [106][111][116][117]. The potential from the source comes cross the spread resistance inside the extracellular medium until reaching the microelectrode (R_{spread}), which depends on the conductivity of the medium (σ) and geometry of the microelectrode [71]. Another important element of the effective electrode impedance are the R_e and C_e which represent the resistance and capacitance of existed double electrical layer at the interface of the medium-microelectrode. In this model, the effective input impedance is the input impedance of the amplifier and shunting paths to ground, is implemented in series to the effective electrode impedance [71].

Based on the conductive volume theory, the spread resistance, anisotropy, and inhomogeneity of the extracellular medium have effect on the signal's amplitude and shape which reaches the microelectrode surface [71]. Consequently, the distance between the neuron and microelectrode and the orientation of the neuron influence the signal recorded by MEA [86]. Another factor which is affecting the recorded signal is the geometry of the microelectrode, which causes various interactions and couplings between the electrode and extracellular media [6]. Larger effective surface area of an electrode reduces the impedance at the medium-microelectrode interface and consequently higher amplitude spikes are recorded [70][1]. For instance, conical and pillar 3D electrodes have larger surface areas than planar microelectrodes used in general *in vitro* neuronal studies. Studies have also showed that neurons can grow directly on 3D microelectrodes and achieve tight physical coupling and sealing, which leads to low impedance and increase in the amplitude of the recorded neuronal signals [6]. Besides, the electrodes with larger surface areas have higher chances to get closer to the neurons and detect signals from more neurons in a brain slice or in a 3D cell culture [118][119][120][121]. However, the fact that the microelectrodes record the averaged spatial voltage inside the extracellular medium, leads to a decrease in the amplitude of the recorded signals as the microelectrodes surface area increases [19][71].

3. FEM SIMULATION AND METHODS

FEM is one of the promising methods owing to the implementation of physical components as well as defining extracellular space which are significant for the neural recordings [20]. COMSOL Multiphysics® version 5.5 was utilized to perform the simulations in this work. This software is based on the piecewise approximation of the FEM and the domains are divided into the finite sum of elements. Furthermore, the functions are applied to these elements by polynomials and the boundary conditions are approximated locally at the edge of the elements and globally along the field boundary [61]. This simulation is started with defining the F-N equations for modeling the AP propagation along the axon with utilizing partial differential equation (PDE). Moreover, for simulating the 3D extracellular environment, AC/DC module's "Electric Currents, Electrostatics" components were employed. It should be highlighted that these simulations computed by time-dependent solver.

3.1 Fitzhugh-Nagumo Model of action potential

The numerical simulation of the action potential propagation in an axon is carried out by F-N model which is a second-order polynomial nonlinear differential equation [122][61]. Equations (13) and (14) are rewritten based on the allocated parameters ($b = 0.7$, $c = 0.8$, $\epsilon = 0.08$) mentioned in [65] (equation (17),(18)).

$$\frac{dV_m}{dt} = V_m - V_m^3/3 - W \quad (17)$$

$$\frac{dW}{dt} = 0.08(V_m + 0.7 - 0.8W) \quad (18)$$

This part of the simulation was divided into two parts, in first ne, simulation of F-N model using COMSOL Multiphysics software, and in section two, MATLAB software was recruited for the F-N axonal action potential model. The F-N equations (17)(18) are solved in the coefficient form PDE interfaces of COMSOL Multiphysics, found under the Mathematics physics, which contains many well-known PDEs [123]. Many PDEs initiating from physics interfaces and other fields can be studied into a general form comprising derivatives up to second order in both time and space without mixed derivatives [123]. The subdomain equation which COMSOL utilized in a coefficient form PDE with one dependent variable u is:

$$e_a \frac{\partial^2 u}{\partial t^2} + d_a \frac{\partial u}{\partial t} + \nabla \cdot (-c \nabla u - au + \gamma) + \beta \cdot \nabla u + au = f \quad (19)$$

This PDE formulation can solve a variety of problems [123]. In equation (19) e_a is the mass coefficient, d_a is a damping coefficient or mass coefficient, c is the diffusion coefficient, β is the convection coefficient, γ is conservative flux source, and f is the source term. Parameters of the F-N model are arranged in the software based on the equation (19). In this case, e_a and d_a are set to 0 and 1 respectively. Besides, the diffusion coefficient is taken to 1, and the right-hand side of the equation (17)(18) as the source term f .

The geometry of the axon is taken as a 3D cylinder with a scaled radius due to numerical limitation in the F-N modeling in COMSOL (Figure 9). The original diameter of axon is 20 μm [21], but in the simulation it is scaled up to 0.4 m.

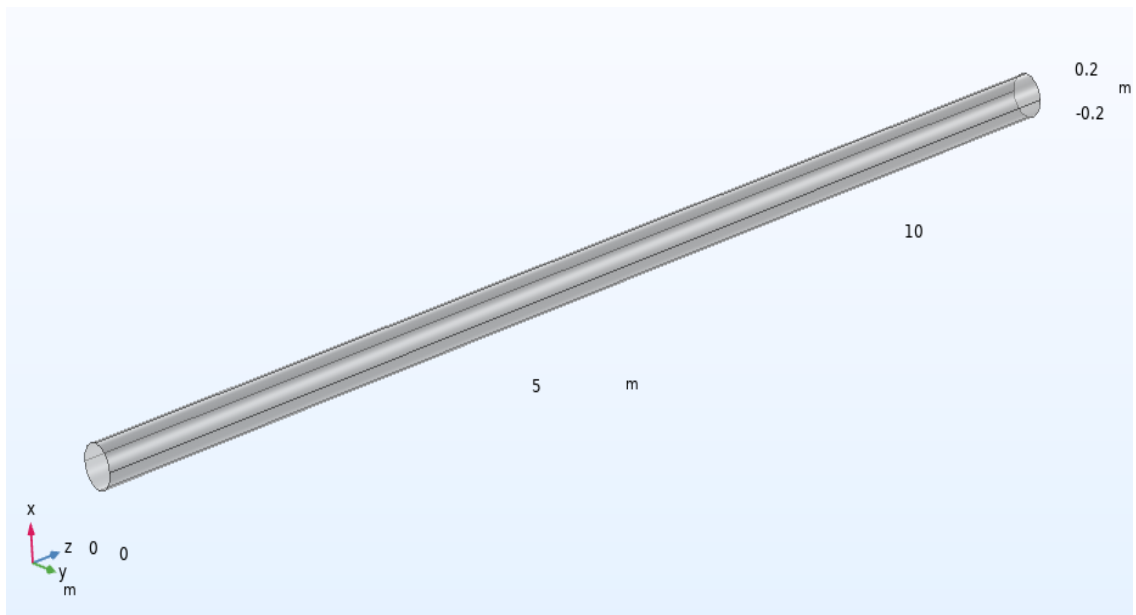


Figure 9. Geometrical model of the axon used in the simulation.

This simulation was done with time dependent solver and the initial values of the variables were $V_m = -1.2 V$, $\omega = -0.62$. The Neumann boundary condition (equation (20)) was defined to zero flux at the boundaries of the axon except at one end of the axon, which was selected as the starting point for the stimulus, by setting the left hand side of the equation (20) to zero [123].

$$-n \cdot (-c\nabla u - au + \gamma) = g - qu \quad (20)$$

In this equation u is the dependent variable, .In this work, the required excitation stimulus for action potential was defined by giving rectangular pulse (a combination of COMSOL's rectangle and analytic functions) at one end of axon , g (Boundary flux) was set to the stimulus pulse, and q which is the boundary absorption was set to zero in the Neuman equation (20). It should be highlighted that the propagation of the action potential was

along the z-axis (Figure 9). Moreover, feasibility of the F-N model in the axon with original size was analysed by allocating various amplitudes to the stimulus.

For the defining the surrounding environment of the axon, a solid block with physical properties of NaCl was utilized for modelling the extracellular medium surrounding the axon (Figure 10). The conductivity and relative permittivity of the extracellular medium were taken as 3 S/m and 80 respectively. The conductivity and relative permittivity of the extracellular medium were taken as 3 S/m and 80 respectively [98][124][110]. Besides, the resistance per unit and the relative permittivity were set to the 0.2 M Ω m and 6, respectively [125].

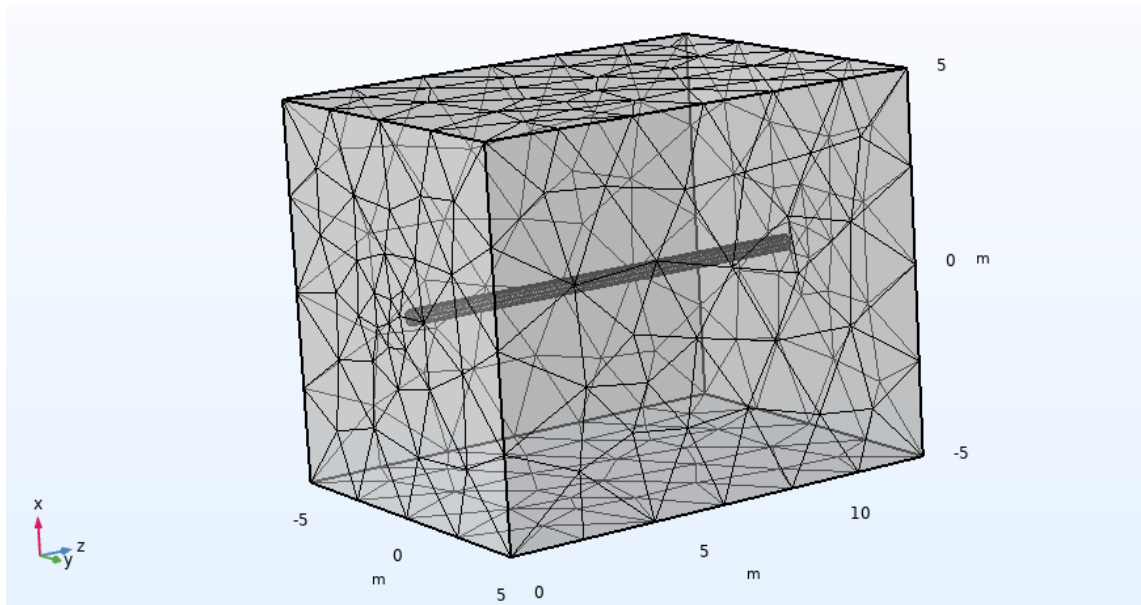


Figure 10. Geometrical model of the axon and extracellular medium.

Electrostatic physics was utilized for coupling the axon and external domain (NaCl) and computing the potential distribution around in the solution. This physics solves differential form of Gauss's law for the electric field, by using V (electrical potential of the solution) as the dependent variable (Equation (21)(22))[123]. In these equations, $\nabla \cdot E$ is the divergence of the electric field, ϵ_0 is the electric constant, ϵ_r is the relative permittivity of the material and ρ_V is the total electric charge density. Electrical potential source of this physics is set to the boundaries of the axon inside the medium ($V = V_m$) and zero charge boundary condition was applied to all the external boundaries of the extracellular medium.

$$E = -\nabla V \quad (21)$$

$$\nabla \cdot (\epsilon_0 \epsilon_r E) = \rho_V \quad (22)$$

Due to some low-quality elements, triangular mesh with minimum 0.135 m element size was used in the axon and the rest of the geometry was meshed with coarser elements. The total number of elements of this simulation was 18639 with 11228 degrees of freedom.

As it mentioned before, this simulation can be implemented in the MATLAB software by writing the equations (17) and (28) of F-N model and applying the system parameters, excitability value, and initial values, the action potential can be acquired on the axon.

3.2 Simulation of multi electrode arrays

In order to have a realistic FEM model for recorded voltages by microelectrodes with different geometries and properties from a neuronal axon, a MEA was simulated.

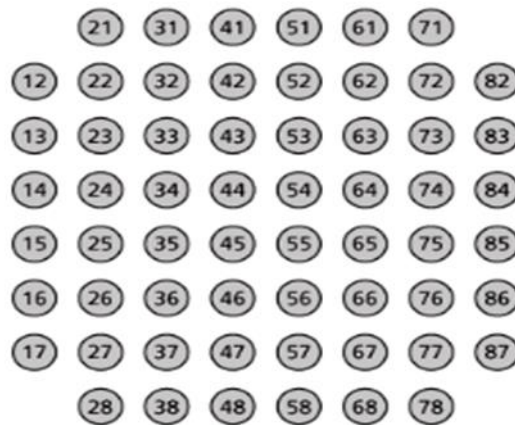


Figure 11. Schematic illustration of a 60-electrode MEA layout of a (model 60MEA200/30iR-Ti, Multi-Channel Systems MCS GmbH) from [126].

The procedure computes the potential field generated by the F-N model of the axon. In this study, planar and 3D MEA models were built in the COMSOL Multiphysics software utilizing coefficients from PDEs and Electric Current physics in AC/DC modules by time-dependent solver. The electric current physics interface can compute the electrical field, current, and potential distribution in conducting media [123]. Moreover, in this physics current conservation equations are solved based on the Ohm's law by defining the electrical potential as dependent variable [123].

3.2.1 Planar MEA

The simulation model of the single axon described in section 3.1 was simulated inside MEA culture dish (MEA model: 60MEA 200/30iR-Ti, Multi-Channel Systems MCS GmbH (MCS), Reutlingen, Germany) [18]. The base material of the simulated MEA dish is glass, and the electrode and insulator materials are titanium nitride and silicon nitride, respectively.

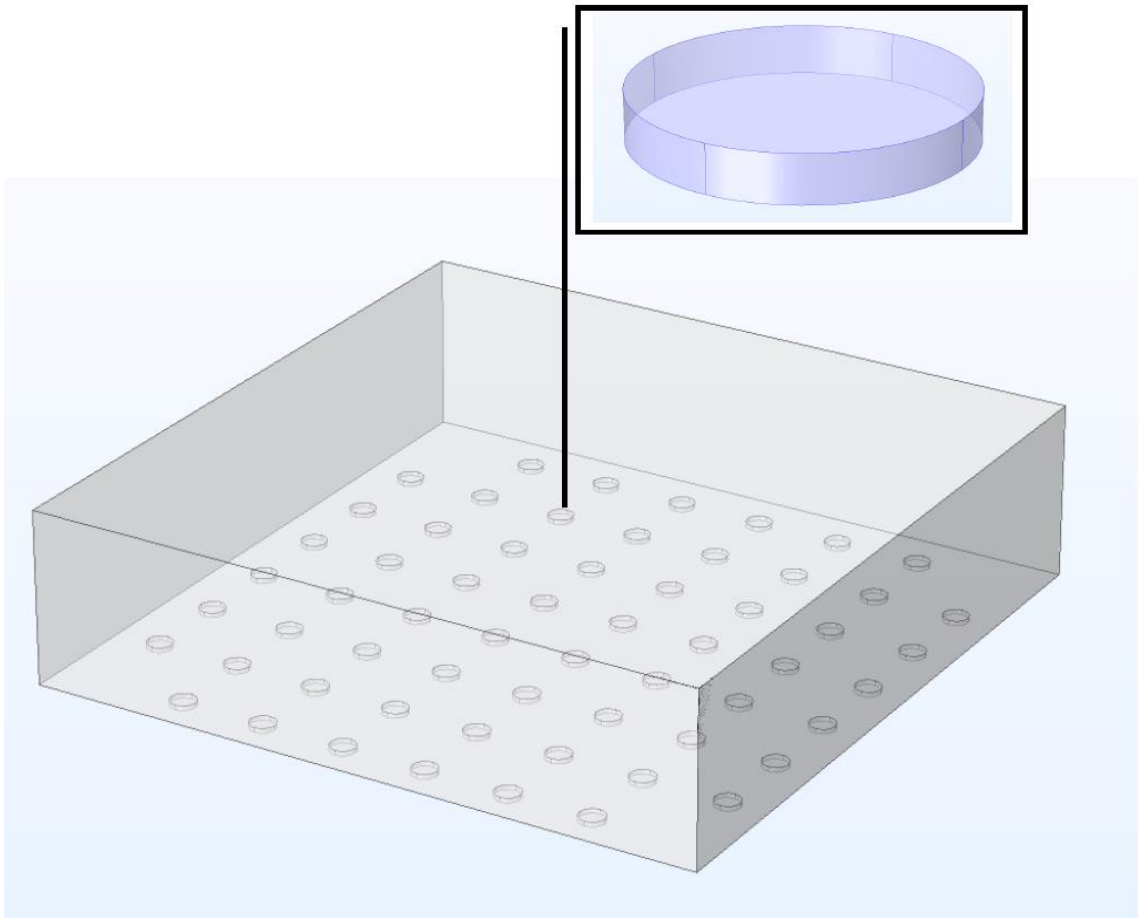


Figure 12. Geometry of the simulated planar MEA and cell culture medium. Close view of the single planar microelectrode demonstrated inside the box.

The MEA-medium system was scaled up with the same factor as the neuronal axon was scaled. The medium was considered to be phosphate buffered saline solution [18]. Besides, solution selection can have effect on the magnitudes of the results, however, the qualitative outcomes and conclusions would not change noticeably [18].

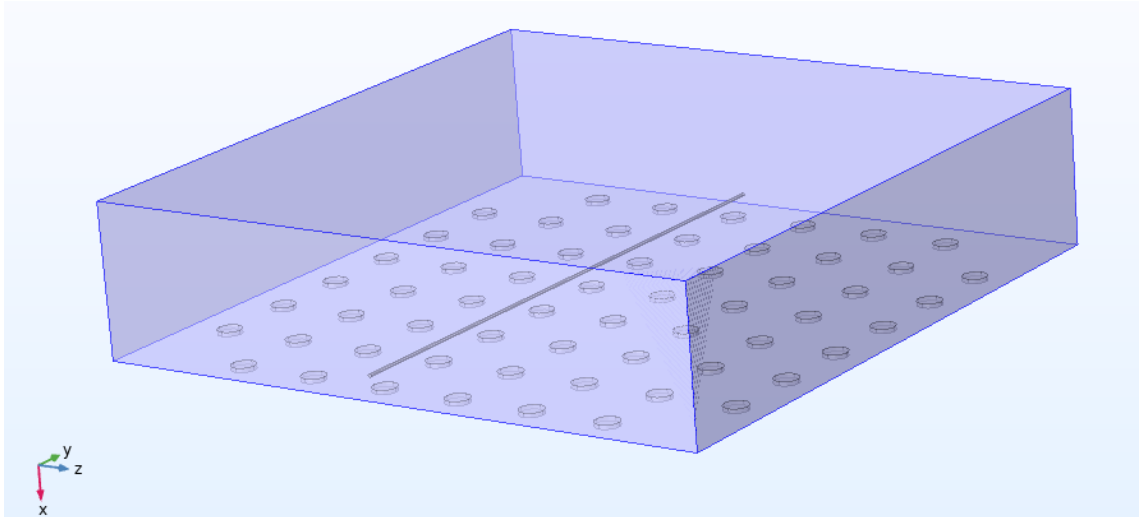


Figure 13. The Geometry of the simulated axon coupled to the MEA.

For numerical modeling of the coupling between the axon and the MEA, the Maxwell's equations were used in this simulation. These equations are represented in the differential form of the Gauss's law for the distribution of the electric charge and electrical field in the medium[123]. The utilized physics solves the equations based on the Ohm's law using the electrical potential as dependent variable.

Gauss's law for electric charge distribution:

$$\nabla \cdot J = Q_{j,v} \quad (23)$$

Ohm's law:

$$J = \sigma E + \frac{\partial D}{\partial t} + J_e \quad (24)$$

Dielectric model for macroscopic properties of the model:

$$D = \epsilon_0 \epsilon_r E \quad (25)$$

In these equations, J is total current flux, j_e is the externally generated current density, Q is the total charge enclosed within the V , σ is the electrical conductivity of the material, and D is the electric displacement. Based on the Gauss's law for electrical field and Ohm's law, electrical potential distribution in each domain of the system was calculated by the COMSOL software.

Electrical insulation boundary condition is defined for the trough and the bottom of the trough (Figure 14):

$$n \cdot J = 0 \quad (26)$$

and the initial value of electrical potential in saline medium was set to $V_0 = 0$. Table 2 lists the used materials and their properties for each simulated domain.

Table 1. Defined materials for each component of the simulation and related physical properties.

Component	Material	Relative permittivity	Electrical conductivity(S/m)
Electrodes	Titanium	6.1589	$182 \cdot 10^4$
Medium	NaCl	80	0.3
Axon	-	6	$1.025 \cdot 10^{-4}$

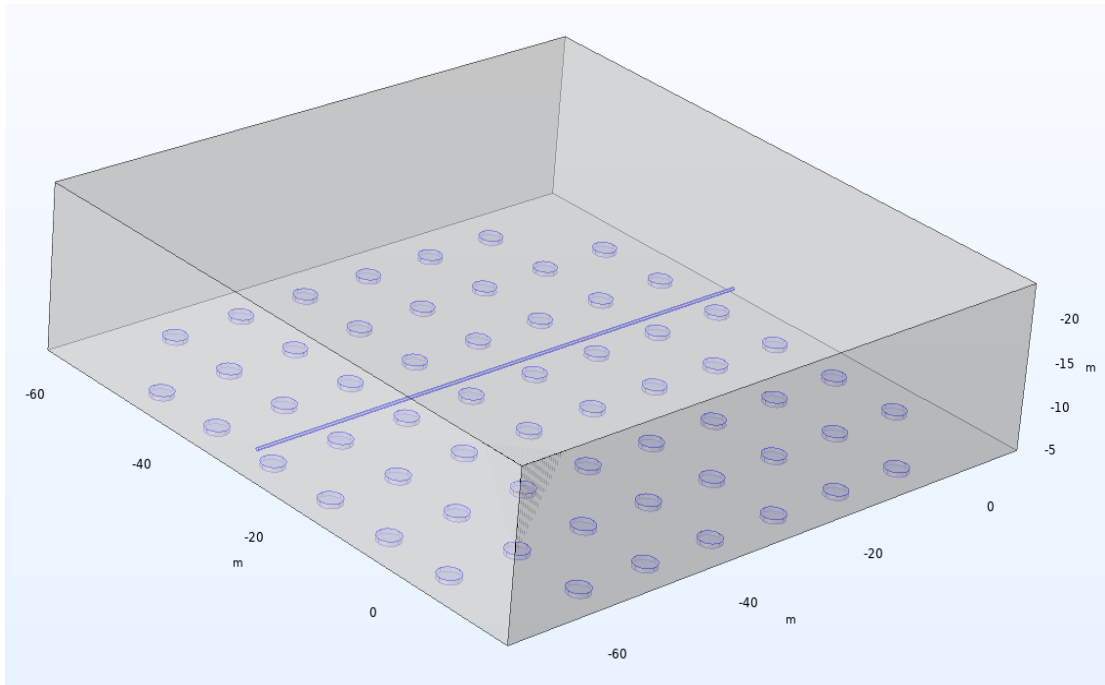


Figure 14. Boundary conditions in different component of the system. Gray color shows the insulation condition and the blue components are defined by distributed impedance condition.

In order to apply the electrical field inside the extracellular medium due to AP propagation along the axon Distributed surface impedance condition defined around the axon's boundary[23]:

$$n \cdot J = \left(\frac{1}{\rho_s} + c_s \frac{\partial}{\partial t} \right) (V - V_{ref}) \quad (27)$$

Where V_{ref} is the membrane voltage (V_m), surface resistance (ρ_s) is $1000 \text{ } (\Omega \cdot \text{cm}^2)$, and the surface capacitance (c_s) is $1 \text{e-}6 \text{ } (F/\text{cm}^2)$.

The final step in defining the boundary conditions is implementing the double electrical layer of the electrode-medium interface (Figure 15). For this issue, distributed surface impedance in the boundaries of the electrode- medium is defined (equation 14). V_{ref} was set to V (potential inside the medium), surface resistance and capacitance were set to $10^{-8} \Omega.cm^2$ and $0 F/cm^2$ for analyzing the ideal condition. However, for assessing the realistic condition, surface resistance R and capacitance C were selected to $462.6 \Omega.m^2$ and $2.59 \cdot 10^5 nF/m^2$, respectively based on the scaling factors in equations (28) and (29) [18].

$$R = \rho \frac{L}{A} \quad (28)$$

$$C = \varepsilon \frac{A}{d} \quad (29)$$

In these equations, ρ is the electrical resistivity of the material, L is the length of the conductor, A is the surface area of the conductor, ε is the electric constant, d is the separation between the capacitor plates.

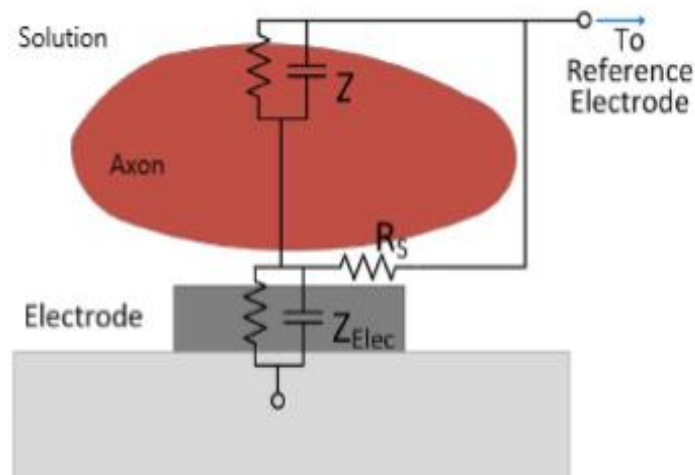


Figure 15. Electrical model of the electrode-medium coupling. R_s is the medium resistance, Z_{Elec} is the complex impedance of the electrode-medium coupling, and Z is the distributed impedance on the surface of the axon (Adopted from [127]).

FEM, free triangular mesh was utilized for the axon simulation with the minimum element size of $13.5 \cdot 10^{-2} m$ and free tetrahedral mesh was used for the rest of the system with $25 \cdot 10^{-2} m$ minimum element size.

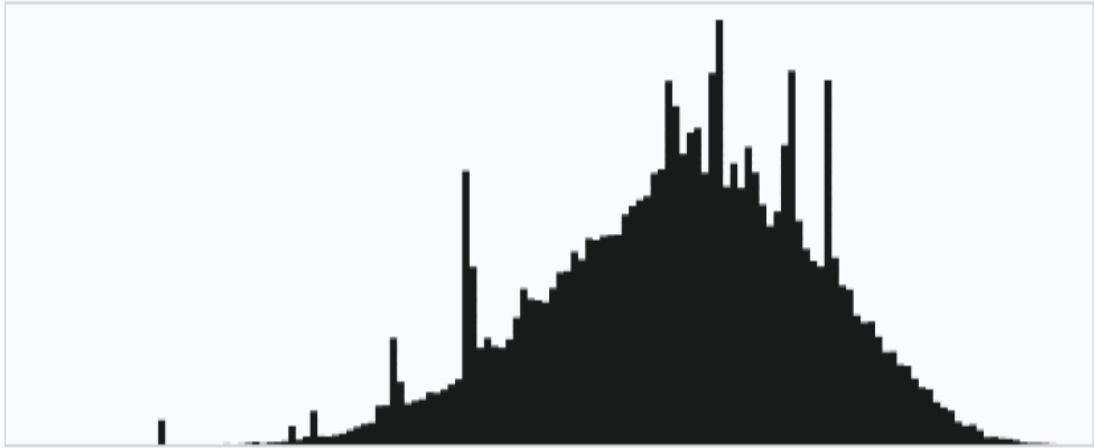


Figure 16. Element quality histogram of the discretized model.

Utilized meshes discretized the simulated system to 121508 elements with minimum element quality of 0.145 and 121800.0 m^3 mesh volume (Figure 17). For decreasing the run time of the simulation, coefficient form PDE and Electric current physics were solved in two different time-dependent solvers and the total runtime was 30 minutes.

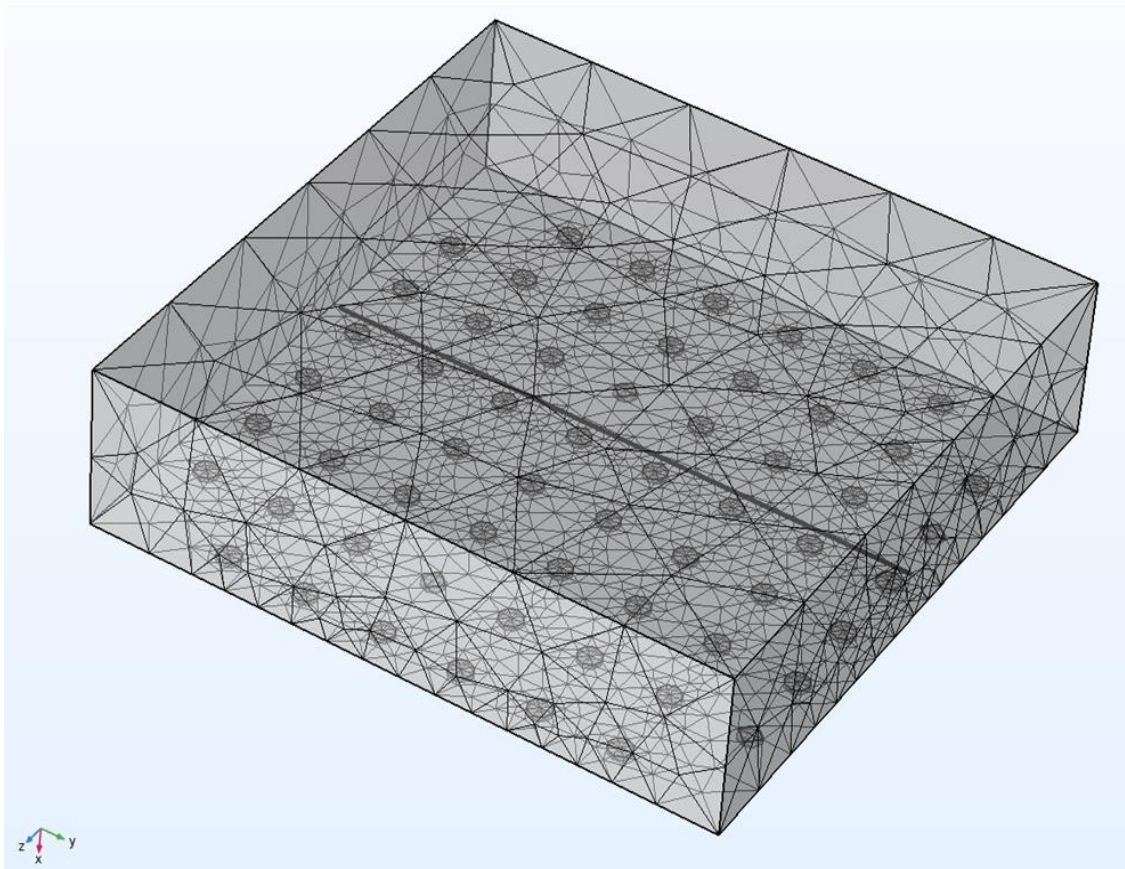


Figure 17. Mesh model of the axon coupled to the MEA and medium.

3.2.2 Multiple axon in the MEA

One of the objectives of this study was to analyze recorded voltages from multiple axons in the medium. For this, two axons in different position were simulated (Figure 18) with the same F-N coefficient form PDEs but with various model input stimulation times.

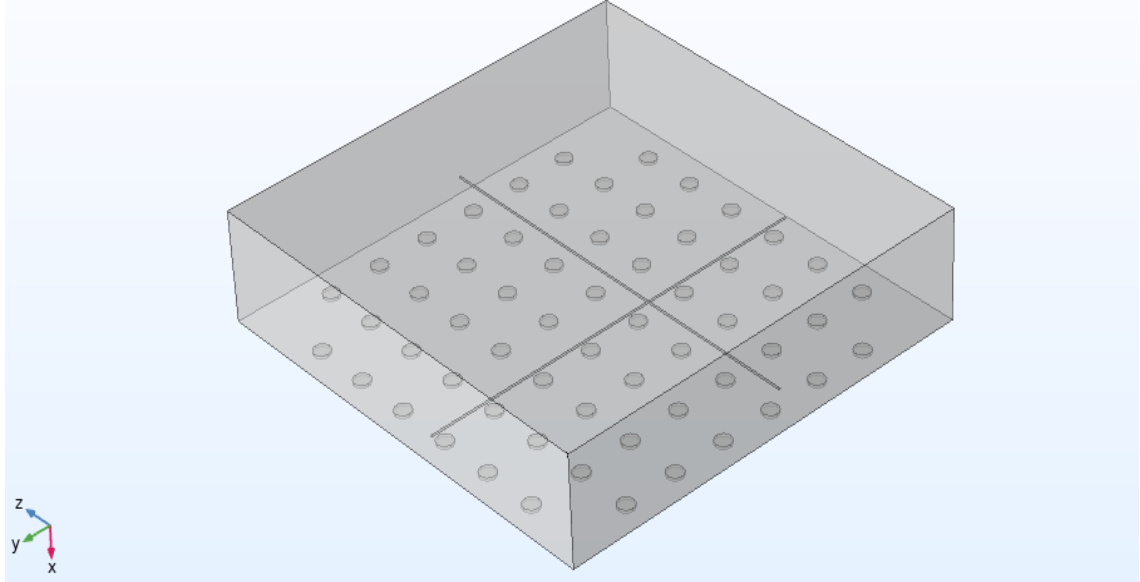


Figure 18. Model of the multiple axon inside the neurochip.

3.2.3 3D MEA

The FEM model of the 3D MEAs with pillar electrode included the same complex impedance in the interface of the medium-microelectrode interface as the planar MEA model. The geometry effects of the microelectrodes on the recorded signals from axons were simulate with the same materials and medium as the planar MEAs and considering ideal interface between the 3D electrodes and the medium.

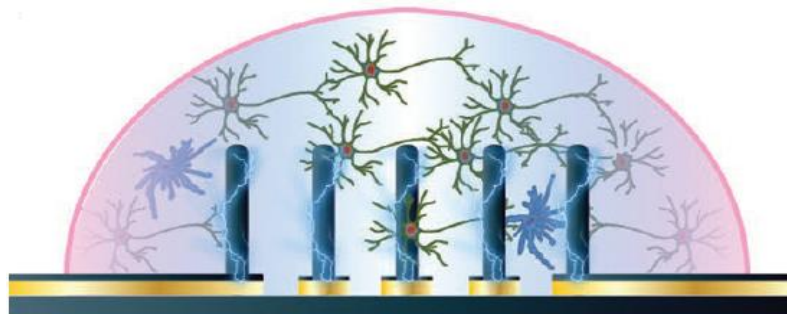


Figure 19. Interfacing neuron-laden medium with 3D MEA electrodes (Adapted from [101]).

Consequently, 6×6 array of 3D titanium pillar electrodes were considered with height and diameter of 100 and 15 μm , respectively (Figure 20)[101]. Furthermore, an axon was placed in the phosphate buffered NaCl solution (medium) at various distances from the microelectrodes. In this work, the pillars electrodes were modelled as scaled cylinders with the same scaling factor as used for the planar MEA simulations. Also, conductive polymer pillars (CP pillars) with multiple axons was studied.

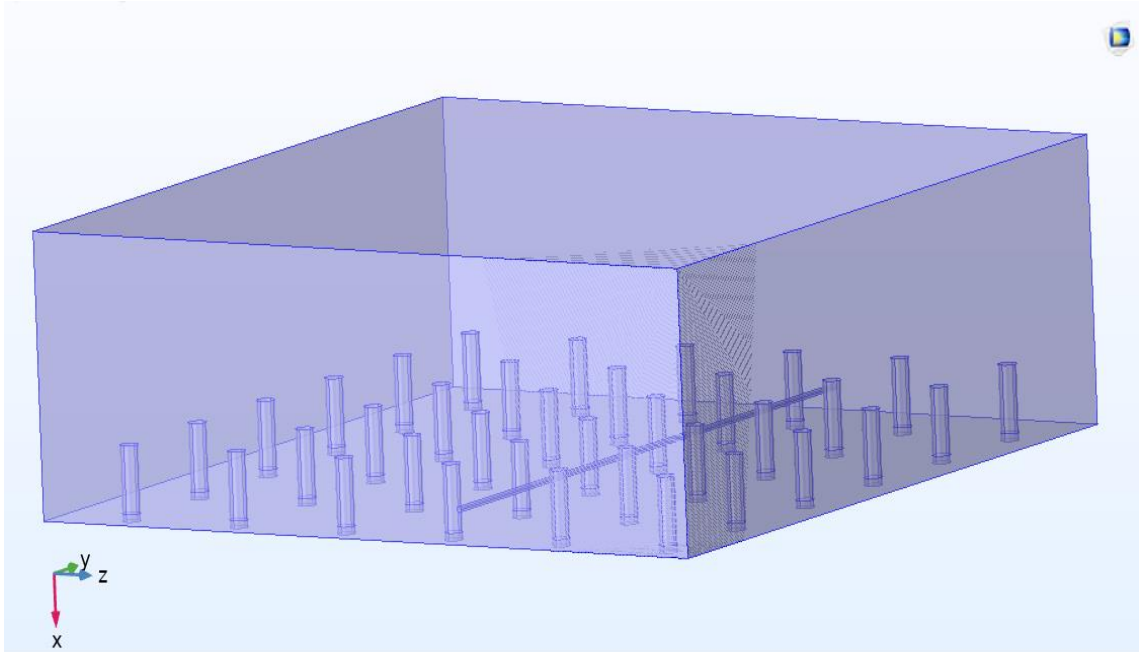


Figure 20. Geometry of the simulated 3D pillar electrode MEA and an axon.

The same boundary conditions as for the planar MEA simulations were defined in this system and free tetrahedral mesh was used for the system with 25×10^{-2} m minimum element size. The system discretized to 89641 elements with average element quality (skewness) of 0.619 (Figure 21). As the size of the pillars are small, finer mesh was defined in pillars and figure 21 demonstrates the low skewness for the pillars. The lower skewness can increase the accuracy of the simulation[128]. The simulation run time was 25 minutes.

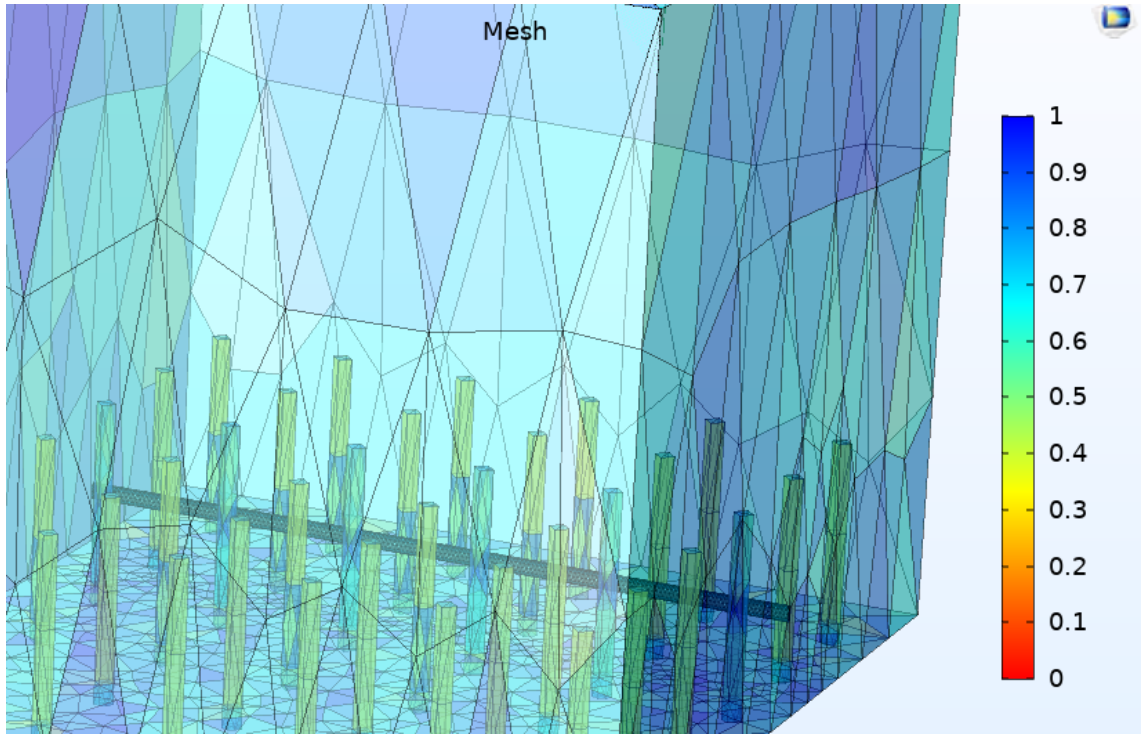


Figure 21. Closeup view of the FEM model. Element color denotes the element quality based on skewness.

4. SIMULATION RESULTS

4.1 F-N model of action potential

4.1.1 3D simulation

Figure 22 depicts typical neuronal action potential gained from the specific point along the axon concerning spatial and temporal dynamics. The membrane voltage demonstrated a depolarization from the resting voltage (Which defined as -1.2 V in this simulation) to the peak and repolarized back to the equilibrium value (-1.2 V). Figure 23 visualize the probe plot in three different domain point probes along the axon. Each probe was implemented in a 10-meter distance from each other along with the propagation of the AP. Consequently, the speed of the propagating AP was obtained based on the equation (17). This result complies with the speed of real neuron AP without myelin sheaths (approximately $0.5\text{--}2.0\text{ m/s}$) [129].

$$V = \frac{x}{t} = 0.789\text{ m/s} \quad (30)$$

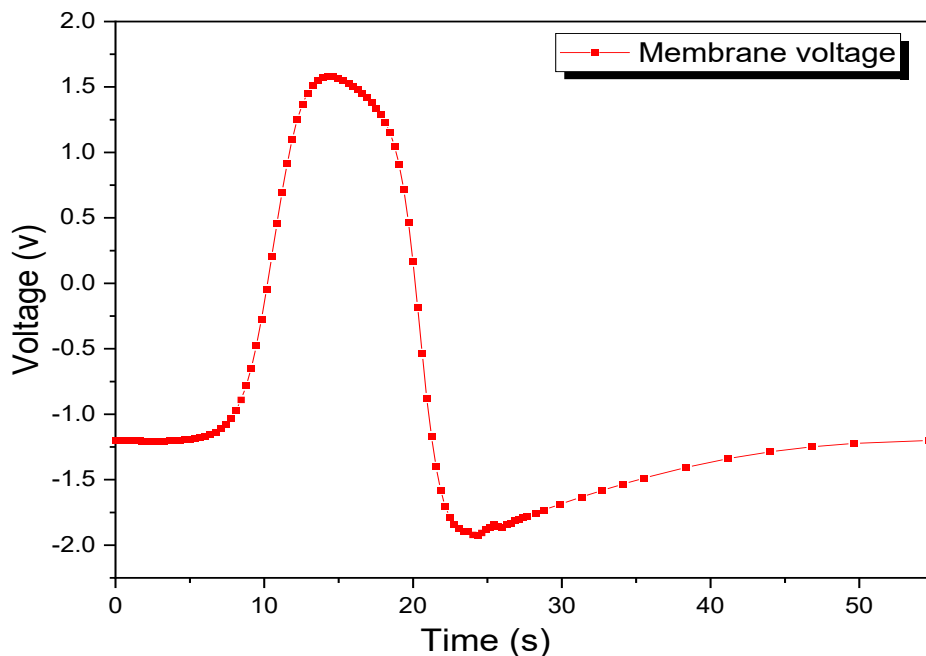


Figure 22. Simulated AP pulse on the membrane of the axon.

Figure 24 illustrates the electrical field around the activated axon in the extracellular domain, which was simulated by utilizing electrostatic physics. The arrow surface plot

shows the vector quantity and voltage distribution in the medium. Figure 25 is the series of the plots obtained at different times and visualizes AP propagation along the simulated axon on the left side and the field potentials on the right.

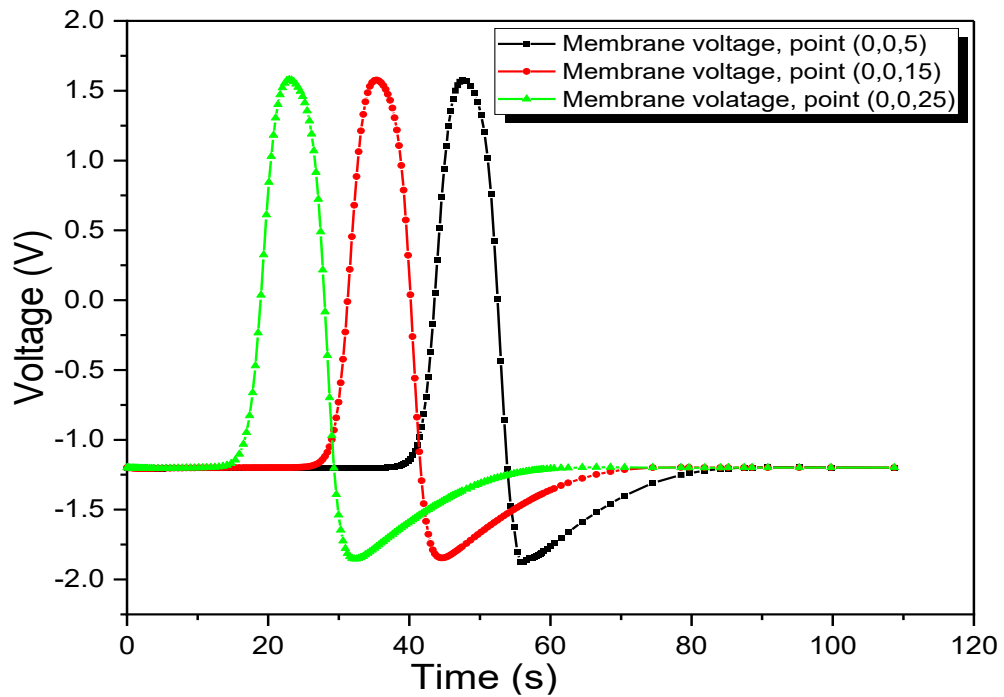


Figure 23. Detected AP at three different points along the axon as the AP propagated through the axon.

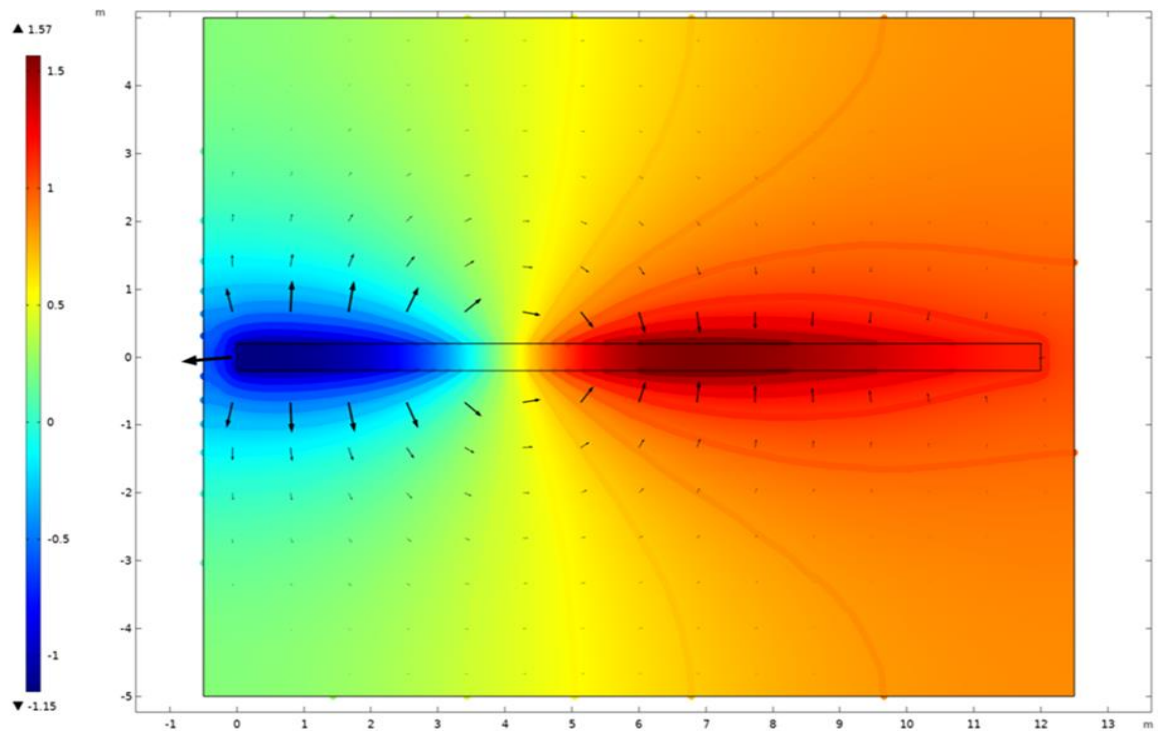


Figure 24. 2D plot of the axon and the electrical field in the extracellular medium due to AP propagation.

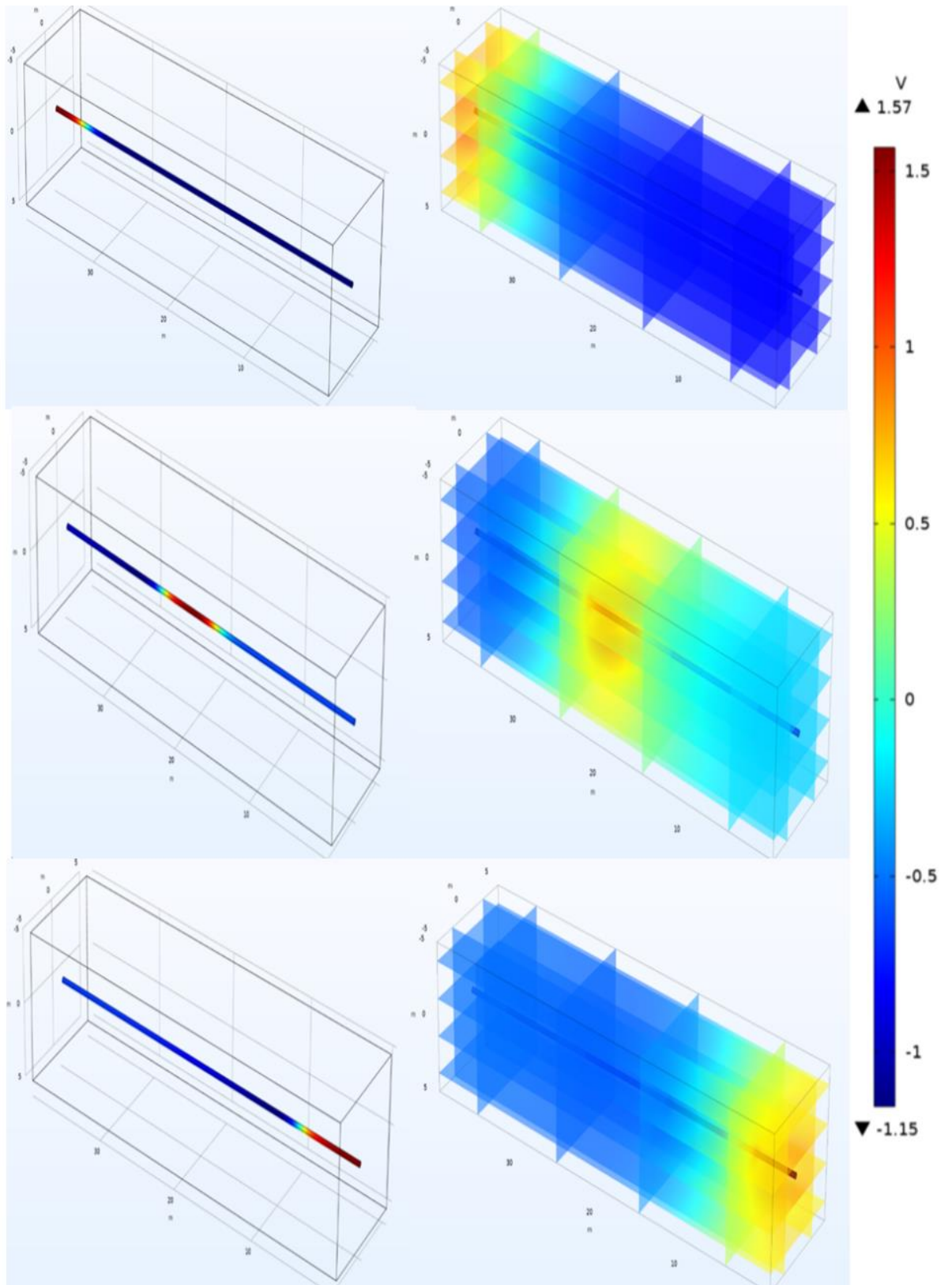


Figure 25. AP propagation in an axon (left column) and extracellular field potential (right column) at different times.

Figure 25 shows how the voltage of the extracellular which coupled to the activated axon (left column) has been changed by propagating the pulse along the axon at different times. In order to show the feasibility of the F-N model in the axon with the natural size, multiple stimuli with various amplitudes were applied to the axon. figure 26, illustrates the effect of the stimulus's amplitude on the formation of the action potential in the axon with the original size. The stimulus with the highest amplitude (1 V) showed a quick depolarizing, however, repolarizing and hyperpolarizing durations lasted same time as the axon with scaled size. Other stimuli caused slow polarization in all the phases except stimulus with 0.01 (V), which was lower than the excitation threshold of the membrane and the action potential no longer formed.

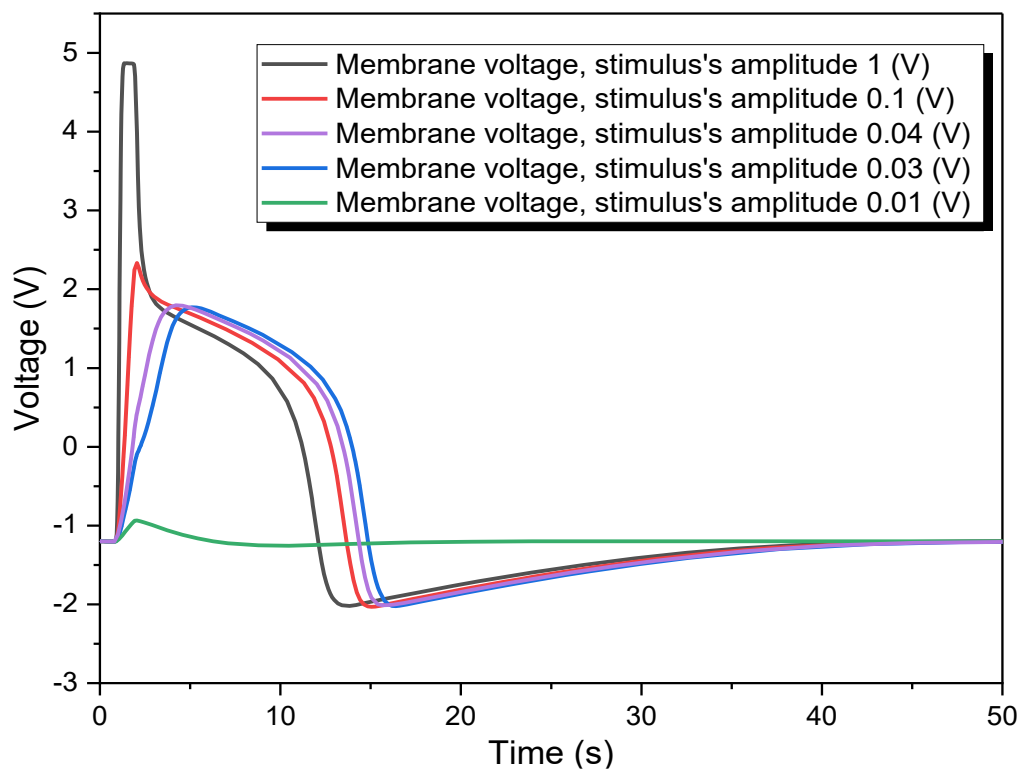


Figure 26. Membrane voltages based on the amplitude of the applied stimuli.

4.2 2D F-N simulation

For comparison, MATLAB software was employed to build the F-N model based on the same parameters and initial values that were utilized in the COMSOL simulation. Figure 27 demonstrates a series of simulated AP waveforms on the axon. This figure shows approximately the same waveform, amplitude, and the duration of the AP as given by the simulated F-N model in COMSOL.

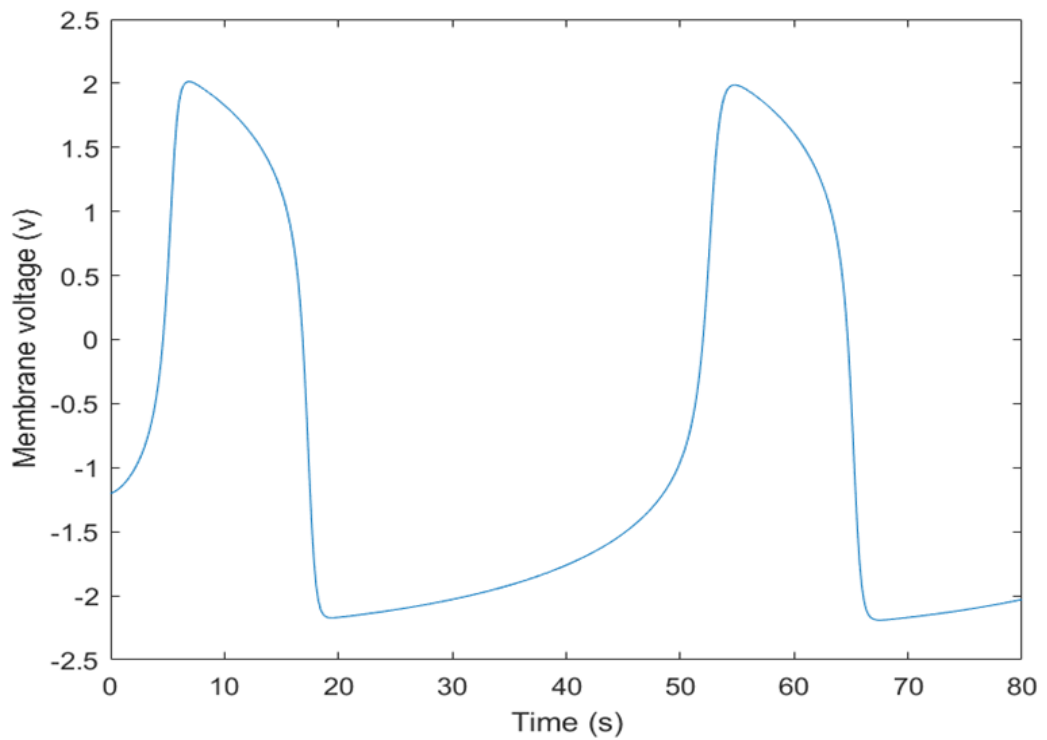


Figure 27. Series of action potential on the axon simulated by MATLAB.

4.3 Neurons coupled to planar MEA

In this part, the action potential of the axon which has been recorded by planar MEAs is demonstrated. Figure 28 depicts the voltage distribution inside the extracellular medium by a multislice plot. A 2D view of the model has been demonstrated in figure 29 (a). Axon has been placed at 2.5-meter vertical distance towards the microelectrodes. The red part of the membrane illustrates the depolarizing phase of the AP and following that the repolarizing phase was shown with the blue color. This figure shows that voltage of the extracellular medium decreased by increasing the distance from the AP. This happened due to the defined electrical conductivity inside the medium. In Figure 29 (b), membrane potential and recorded signal in one of the microelectrodes have been illustrated. Figure 29 (b) demonstrate that the maximum recorded value of the AP is around 1 V. Figure 29 (a) has two scale for the membrane voltage and solution potential. This figure also illustrates that the voltage distribution at the selected microelectrode is around 1 V.

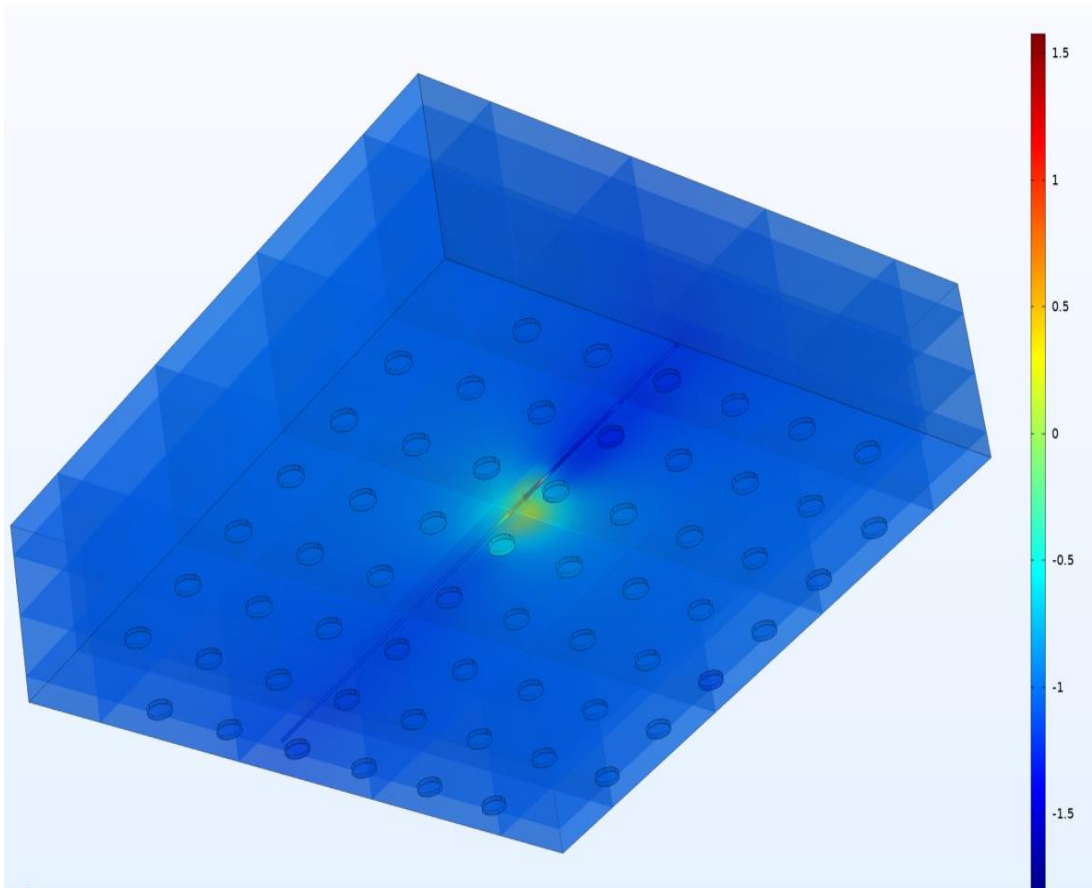


Figure 28. Simulated planar MEA coupled to the axon and the extracellular field potential caused by an AP.

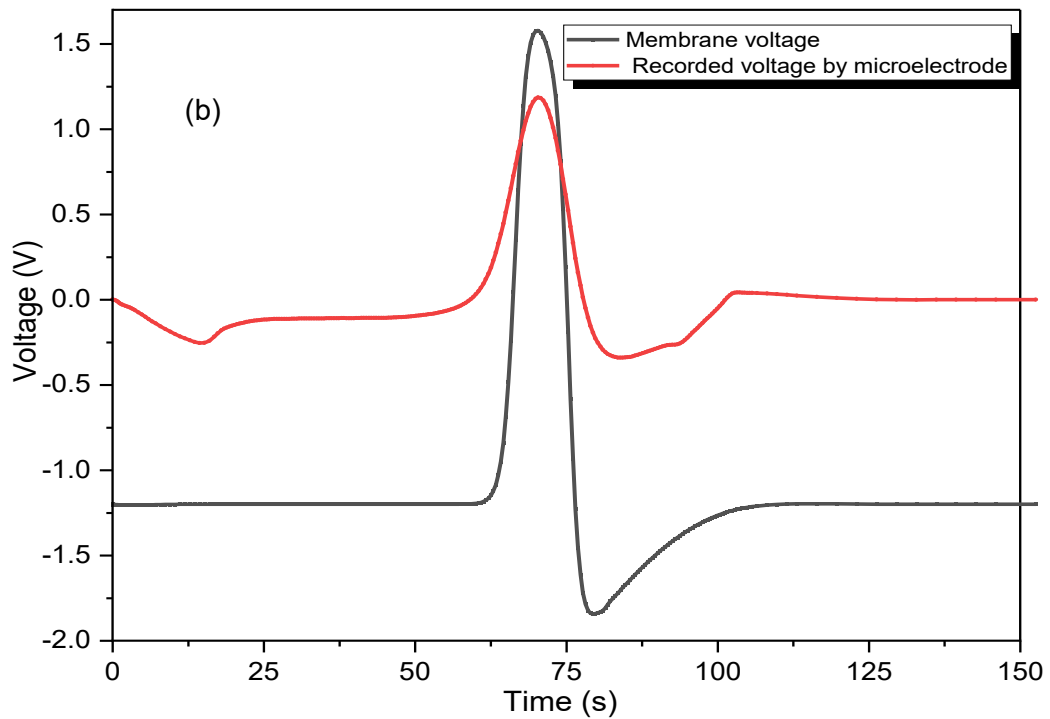
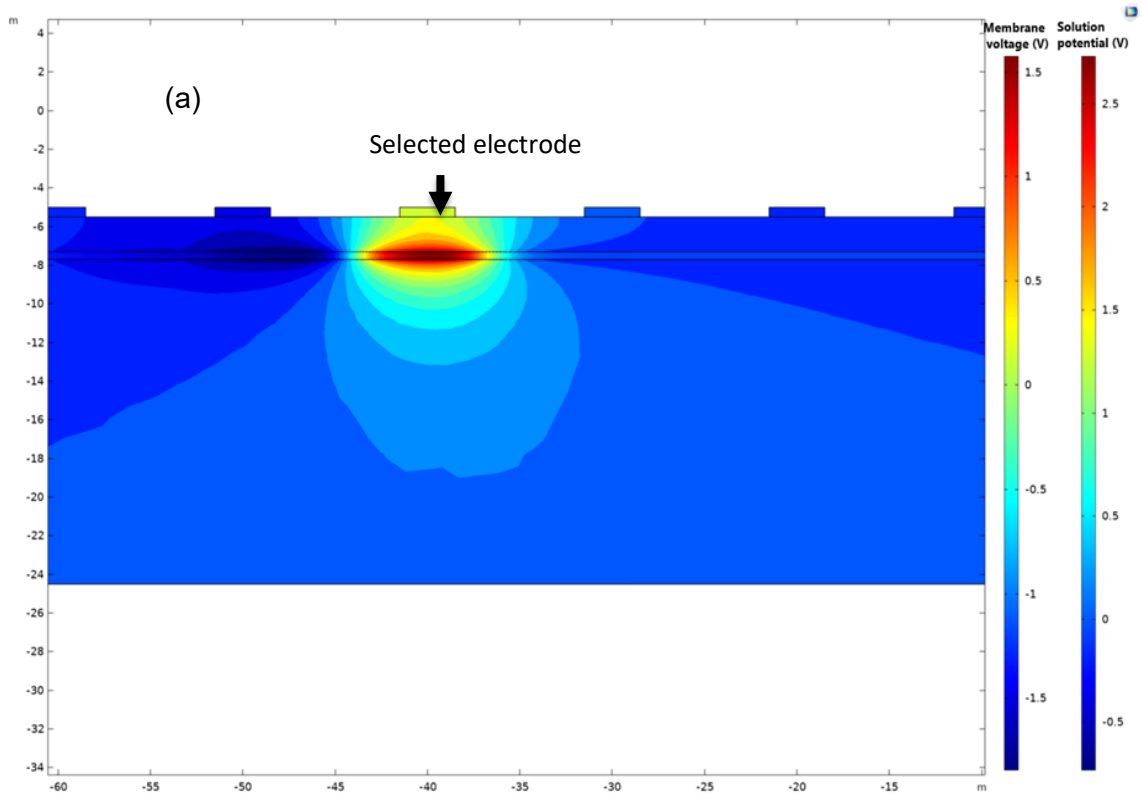


Figure 29. (a) Y-X cut plane view of the MEA dish with microelectrodes shown as small rectangles coupled to the axon and medium, and the electrical field potential generated by an AP moving to the right. (b) The axon membrane potential and the recorded electrical potential in the extracellular medium due to an AP.

Figure 30 depicts the action potential propagation along the axon inside the solution coupled to the planar MEAs at different times. Figure 31a shows the initial potential and electric field inside the medium with the coupled reference electrodes marked red. In this figure the stimulus was applied to the left side of the axon and stimulus generated the AP. Figure 30 b, c, and d visualize the AP moving along the axon and the electrical field around the moving AP along with isopotential lines.

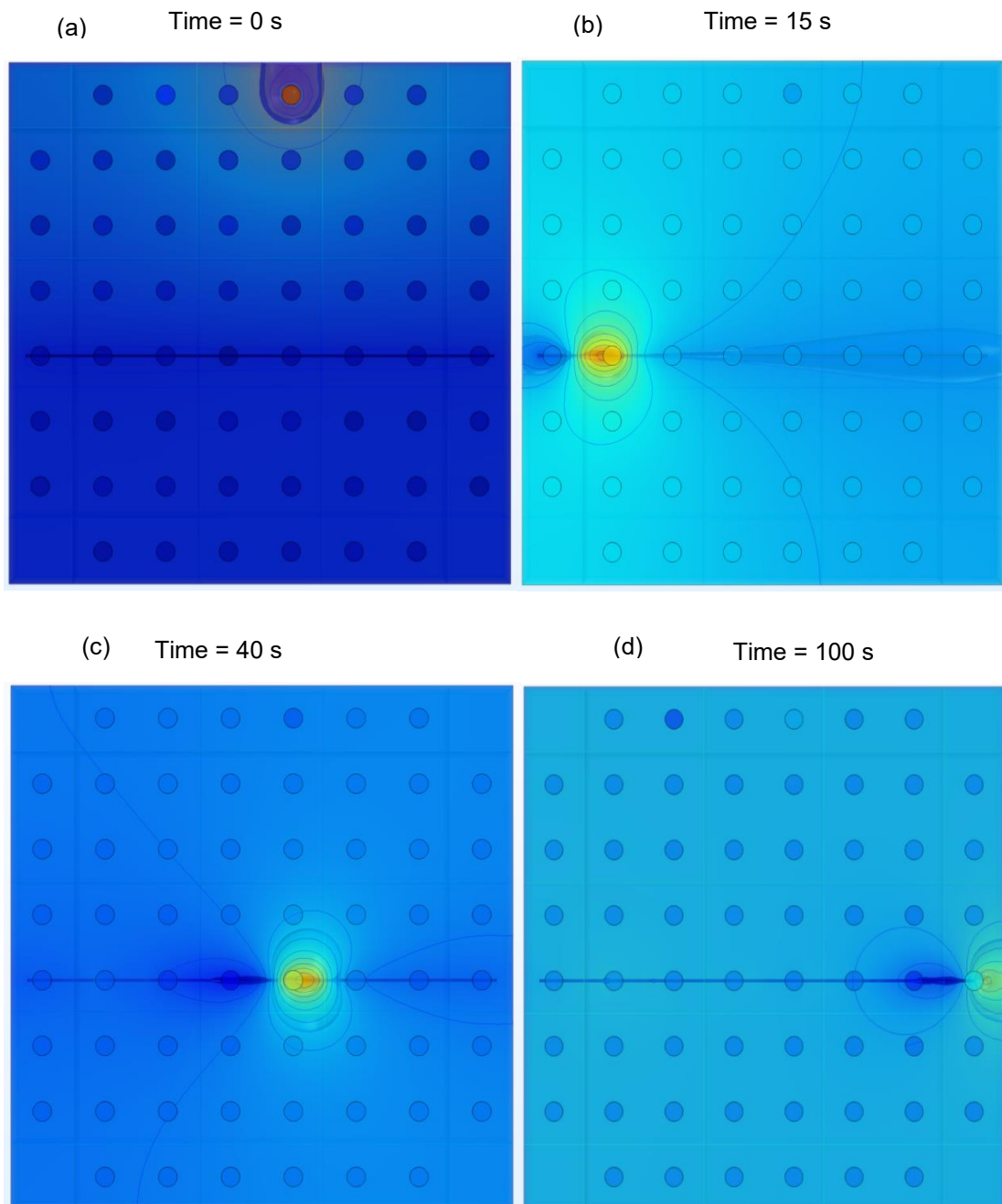


Figure 30. Z-Y view of field potential due to AP propagation along the axon simulated in different time points along with isopotential lines. In (a), the reference electrode is marked red.

Distance effect

Figure 31 and 32 illustrates the influence of distance and direction from the axon to the microelectrode on the simulated AP waveform and amplitude. First, the axon was placed at different vertical distances from the electrode, and the results of each simulation are shown in Figure 31. This figure reveals that the axon, which is in the 0.05 meter vertical distance, detected a signal with the highest amplitude. Next, the horizontal distance effect of the axon toward the microelectrode was investigated in several simulations (Figure 32). The results in Figure 31 and 32 show that the amplitude of the detected APs is inversely proportional to the distance of the axon from the microelectrode. Increasing the distance in the horizontal direction shows higher amplitude reduction of the simulated AP compared to increasing the vertical distance. Due to a meshing problem in the simulation and low-quality discretized elements, the voltage recorded at 0.05 m vertical distance is distorted (Figure 31).

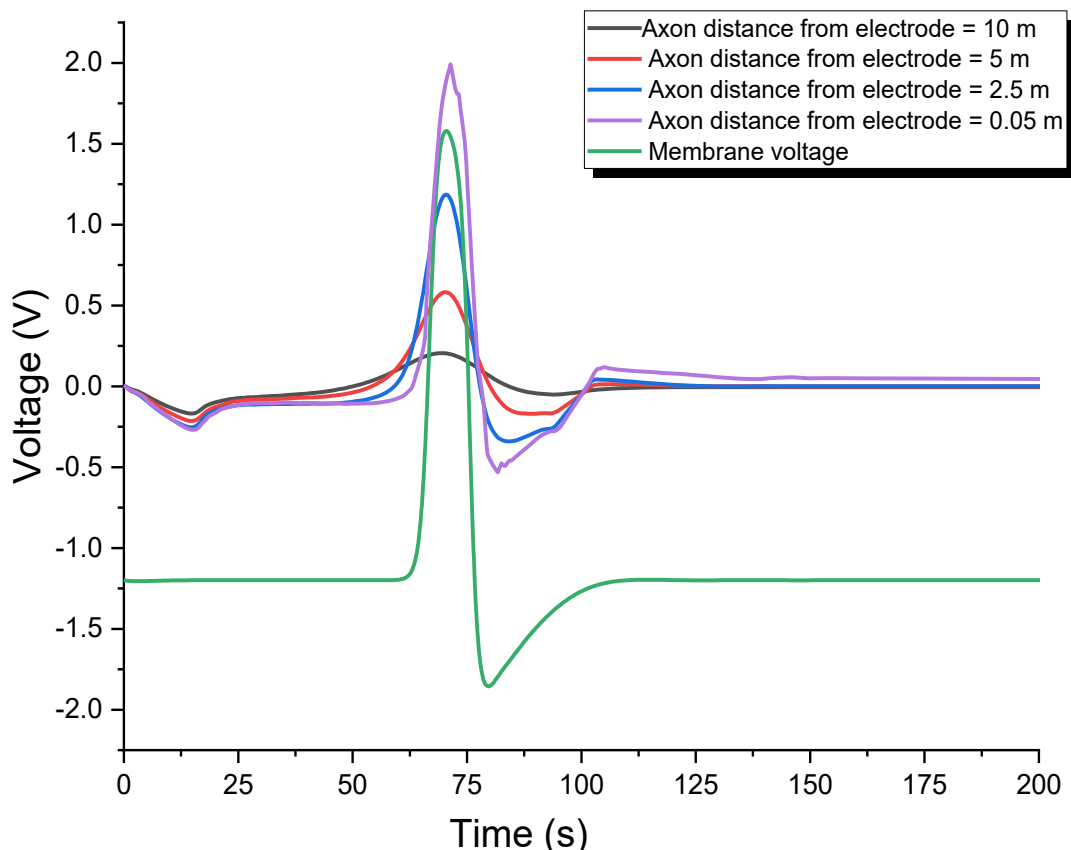


Figure 31. Effects of vertical distance from the axon to a planar microelectrode.

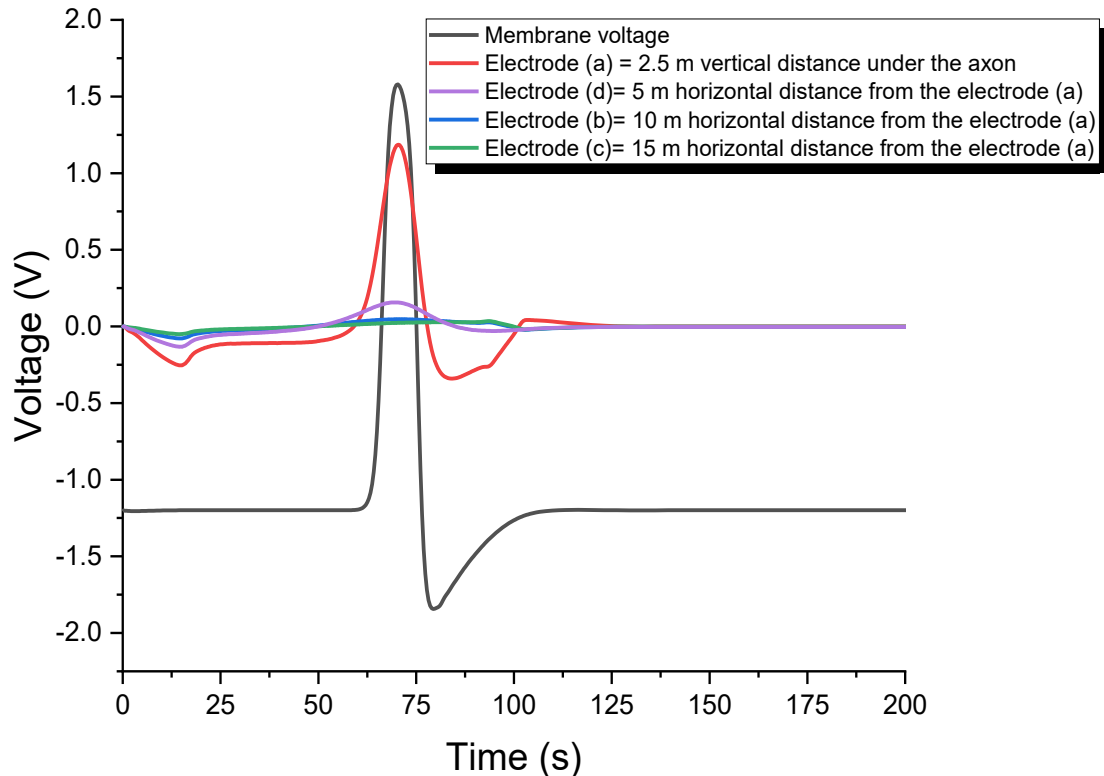
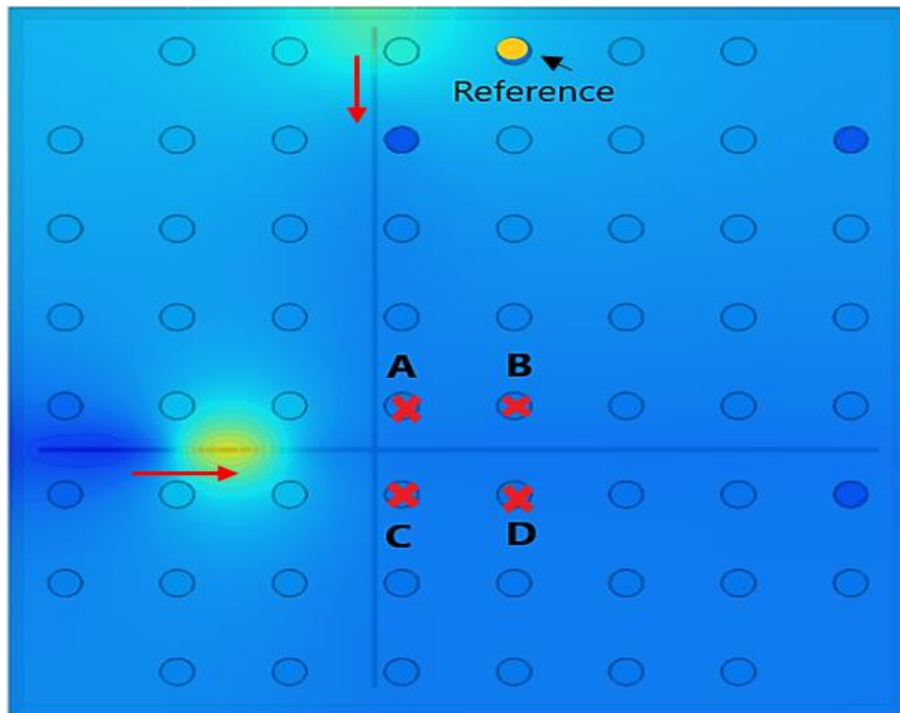


Figure 32. Effects of distance from the axon to a planar microelectrode. The horizontal distance effects on the simulated AP recorded at the microelectrode

4.3.1 Multiple axon

Figure 33 visualizes the MEA dish in which two axons in different vertical distances from marked microelectrode implemented. First, Axon 1 from the left side was activated by applying the stimulus. This neuron was implemented in 2.5-meter vertical distance from the bottom of the MEA. Subsequently, the upper axon was stimulated with 25 seconds delay from the first stimulation and 2.5-meter vertical distance from axon 1. Figure 33 is the Z-Y view from the bottom of the MEA. The AP of the axon 1 (the closest neuron to MEA) demonstrated with higher voltage value compared to the axon 2. The final obtained signals from both axons by various selected microelectrodes were illustrated in figure 34. Although all the marked electrodes were in the same distance towards the axon1, the signals measured via the electrodes A and C exhibited reduction in the first recorded action potential. This issue happened due to the interference by the effects of the membrane voltage of axon 2, which was placed at a close distance from the observed electrodes.

Time = 27 (s)



Time = 90 (s)

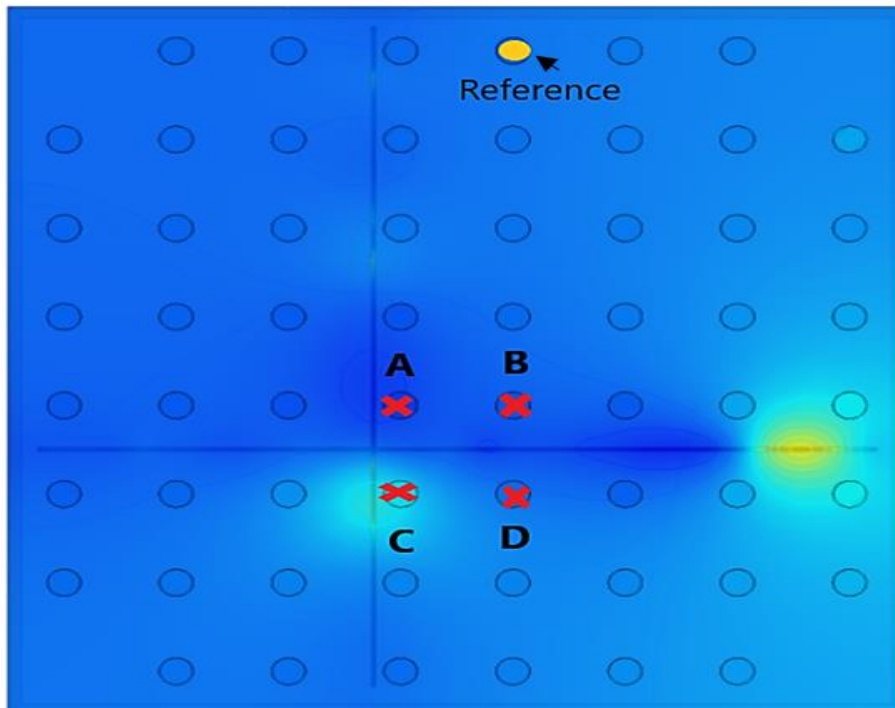


Figure 33. Z-Y view of the two-axon system coupled to MEA.

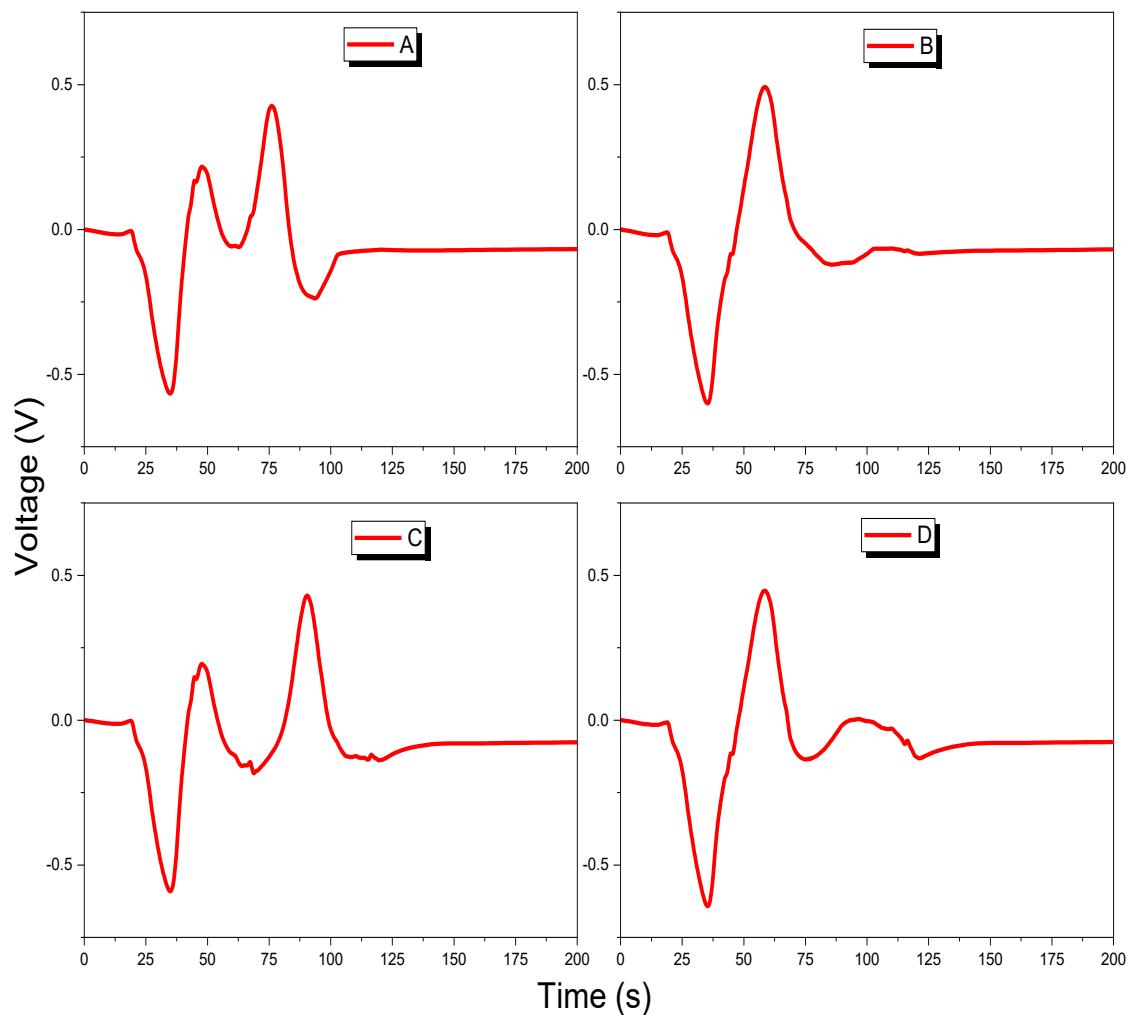


Figure 34. Simulated measured signals of two axons by different planar microelectrodes. These plots illustrate the recorded signals by corresponding electrodes seen in Figure 32.

The distance effect of the axon on the recorded voltage can be seen in the second detected AP in electrodes A and C. As the initial voltages of the medium and electrodes were set to the 0 V and -1.2 V for both axons, a downstroke in the recorded voltage was observed during the 25-5 seconds (Figure 34). Figure 35 shows the recorded voltage by single microelectrode (A) and the corresponding membrane voltages. Moreover, Figure 35 show that the hyperpolarization phase of first AP was reduced due to the second AP. Figure 34 depicts that how other active axons can result in quite complex compound waveforms.

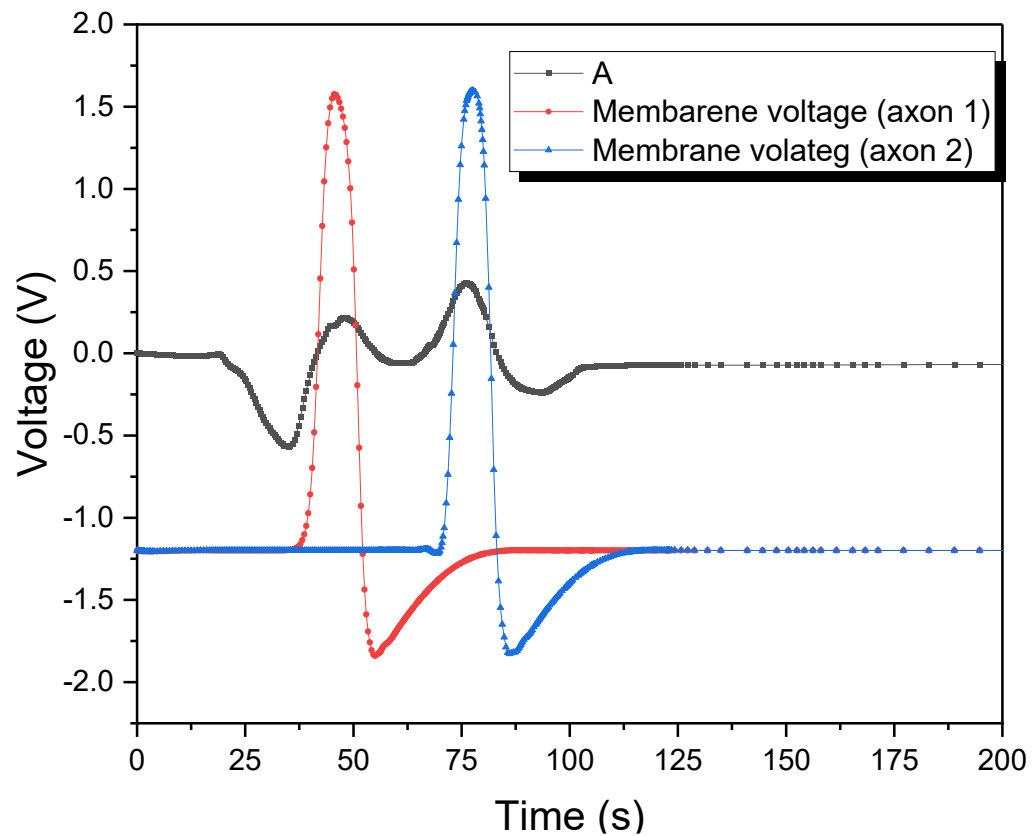


Figure 35. Signal recorded by the electrode A and the membrane voltages the axon 1 and axon 2.

4.4 3D MEA

In this section, the simulation results of the 3D pillar microelectrodes coupled to the medium and two axons are given (Figure 36). Figure 36 shows the potential distribution in the medium due to an AP with isocontours at the bottom of the MEA. Later, a comparison of the planar MEA and 3D MEA based on the geometry effect is analysed with a single microelectrode and surrounded with other microelectrodes (Figures 37-39). In the following figures (41, 42), the distance effect of the neuron-electrode and the multiple axons inside the medium on the simulated measured signal are illustrated.

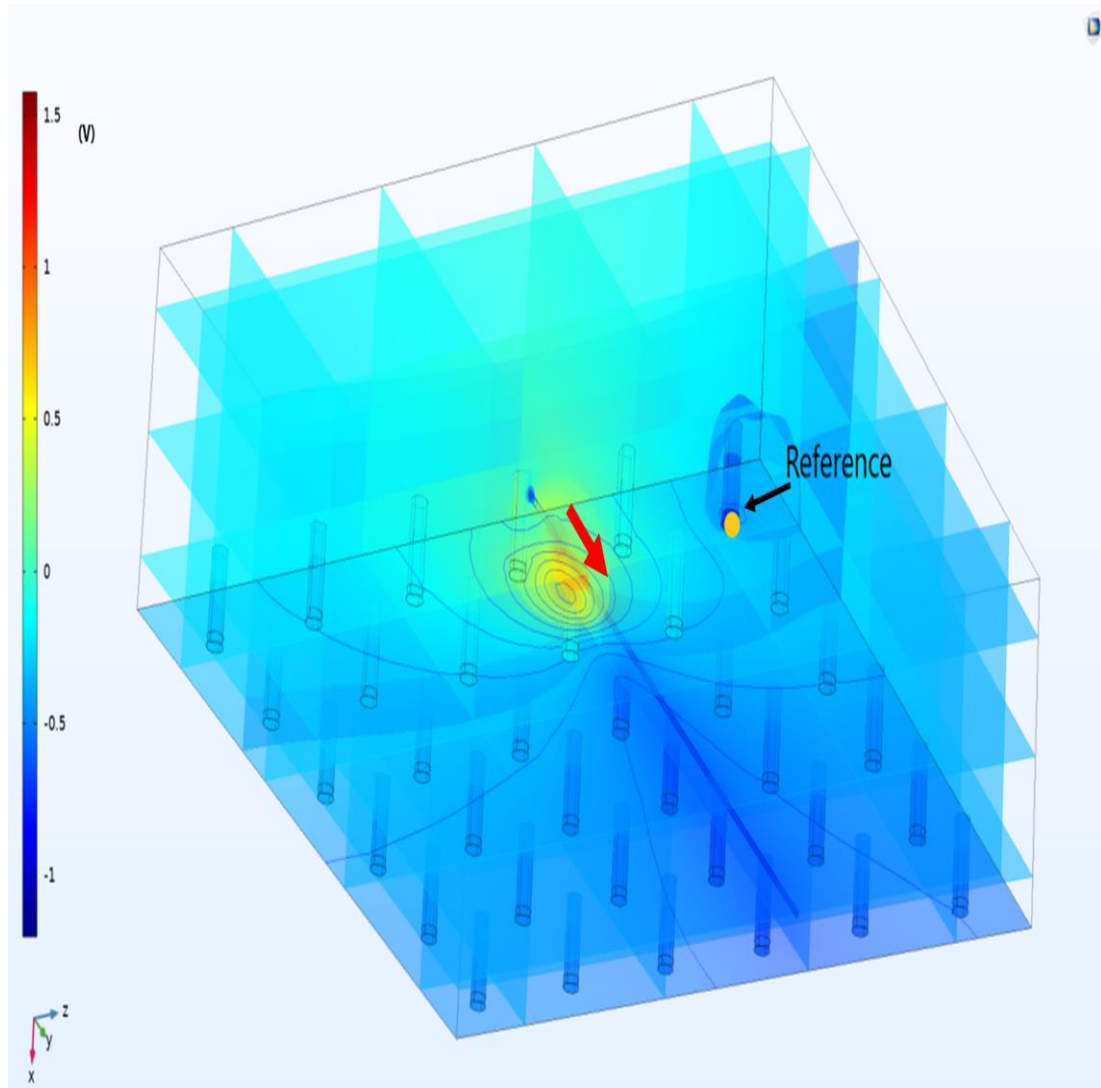


Figure 36. Space view of the 3D MEAs coupled to axon-laden solution.

4.4.1 Electrode geometry effect

For comparing the planar and 3D pillar electrodes based on the geometry effect, the materials, electrode distance from the axon, and the contact impedance in the interface of the electrode and medium were set with the same values. The comparison was accomplished in two parts. In the first part, only one single 3D or planar microelectrode was simulated near the activated axon (Figure 37). Moreover, the influence of the planar microelectrodes surface area was investigated in this part.

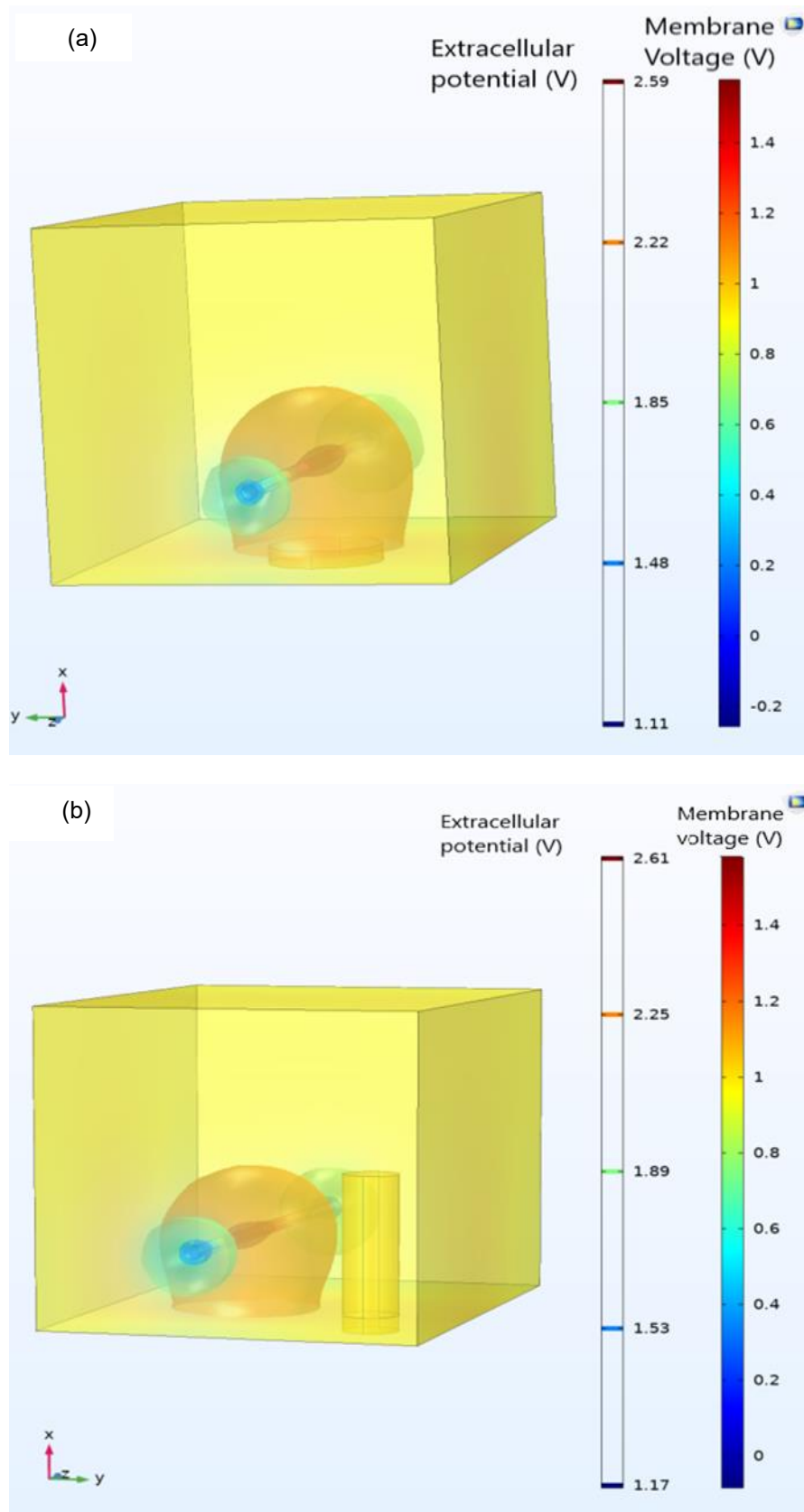


Figure 37. Extracellular electrical field around a single microelectrode due to an AP in an axon. (a) voltage distribution around the planar microelectrode, (b) voltage distribution around the 3D pillar microelectrode.

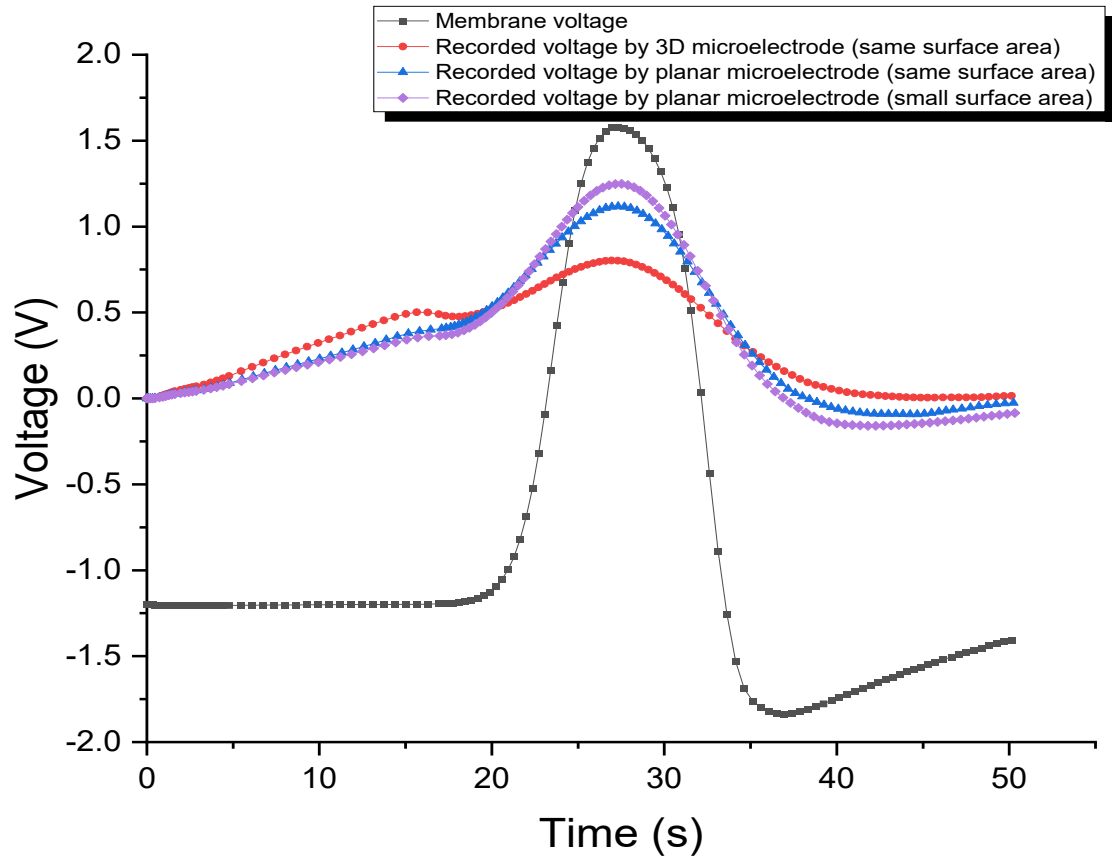


Figure 38. Comparison of the simulated voltage recorded at a single 3D pillar and planar microelectrodes of different surface areas, along with the membrane potential.

Figure 38 reveals that the simulated recorded voltage by the planar electrode, which had a smaller surface area than the 3D pillar electrode, detected higher amplitude AP voltages, due to less averaging than the 3D pillar microelectrodes. 3D pillar microelectrode recorded the signal with the lowest amplitude due to the bigger surface area and spatial averaging of the voltage distribution around the microelectrode.

In the second part of the evaluation of geometry effects, 3D pillar and planar MEAs were analyzed with the same materials, distances from the axon, and distributed resistance value at the interfaces (Figure 39). Figure 40 reveals that the 3D pillar microelectrode recorded AP signals that were a lower in amplitude than the corresponding AP recording from the planar microelectrode. Larger surface area and spatial averaging of the 3D pillar microelectrode led to higher averaging from the voltage distribution around the electrode.

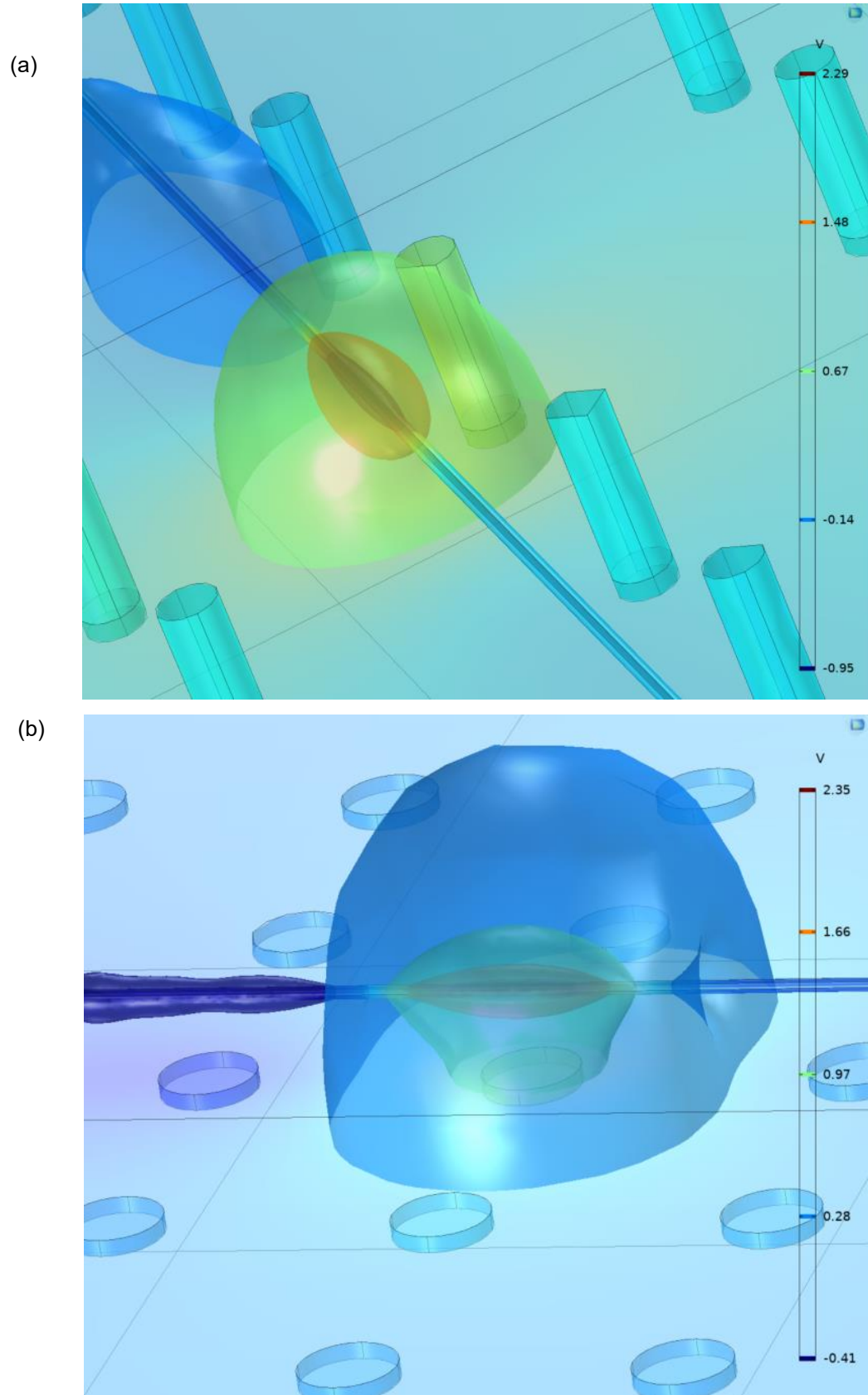


Figure 39. Iso-surface plot of electrical field in the MEA due to AP in the axon. (a) 3D pillar MEA, (b) planar MEA.

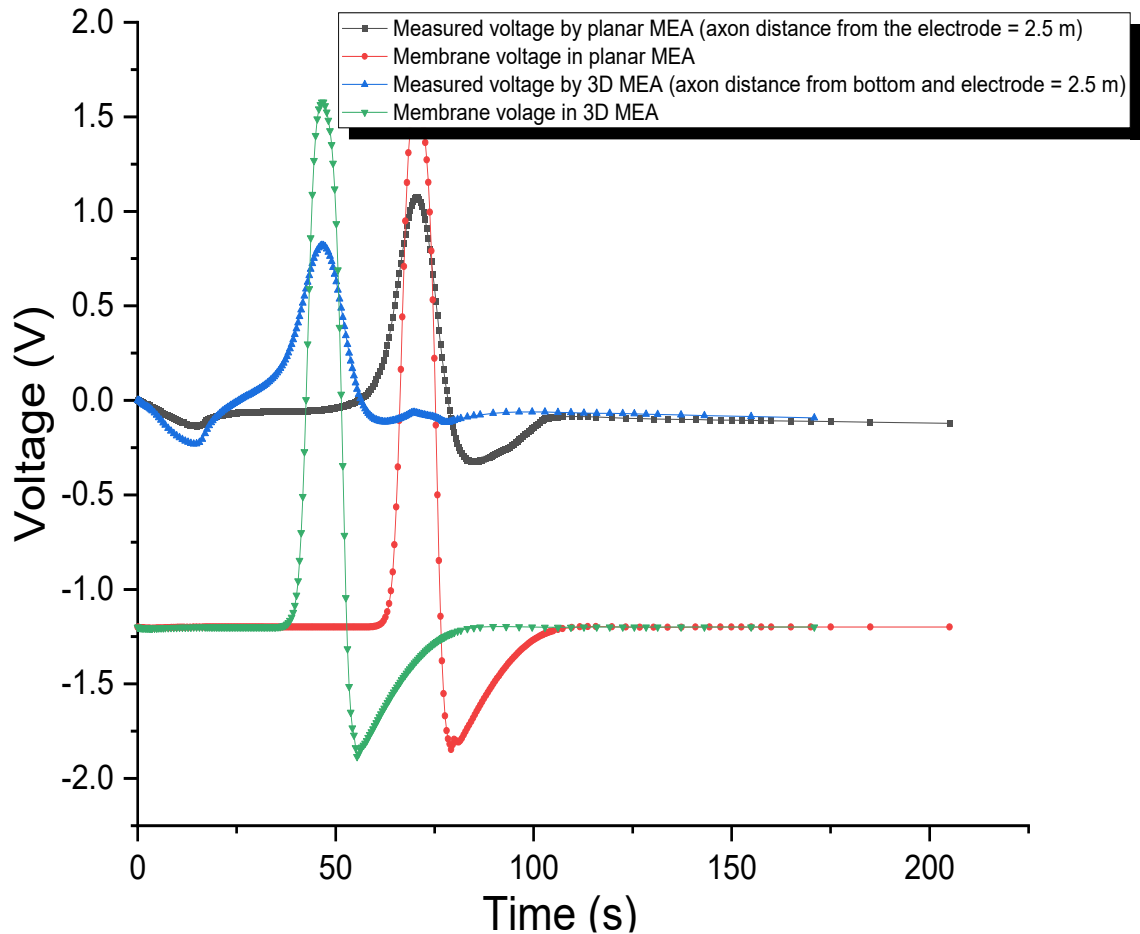


Figure 40. Geometry effect of the microelectrodes on the recorded data from AP in an axon. Recorded signal by 3D pillar microelectrode in the MEA dish and the corresponding planar microelectrode recording along with the membrane voltages.

4.4.2 Distance effect

Figure 41 shows the effects on the simulated recorded signal of the distance from an axon to a 3D pillar microelectrode to various directions. This part was simulated the same way as the distance effect on the simulated recorded signal by planar microelectrode presented earlier. When analyzing the horizontal distance effect, first, the axon was placed at a 2.5-meter distance from the bottom and then at the same distance from the middle point along with the pillar's height (electrode a). By increasing the distance in both directions, the reduction in the amplitude of the obtained signal was revealed. However, by comparing these two plots, the amplitude of the simulated recorded signal in the case where the axon was at the 2.5-meter distance from the tip, exhibited lower amplitude compared to the signal from the electrode in the second plot. This issue has happened due to the electrical conductivity of the pillars and distributed impedance in the interface of the microelectrode and medium.

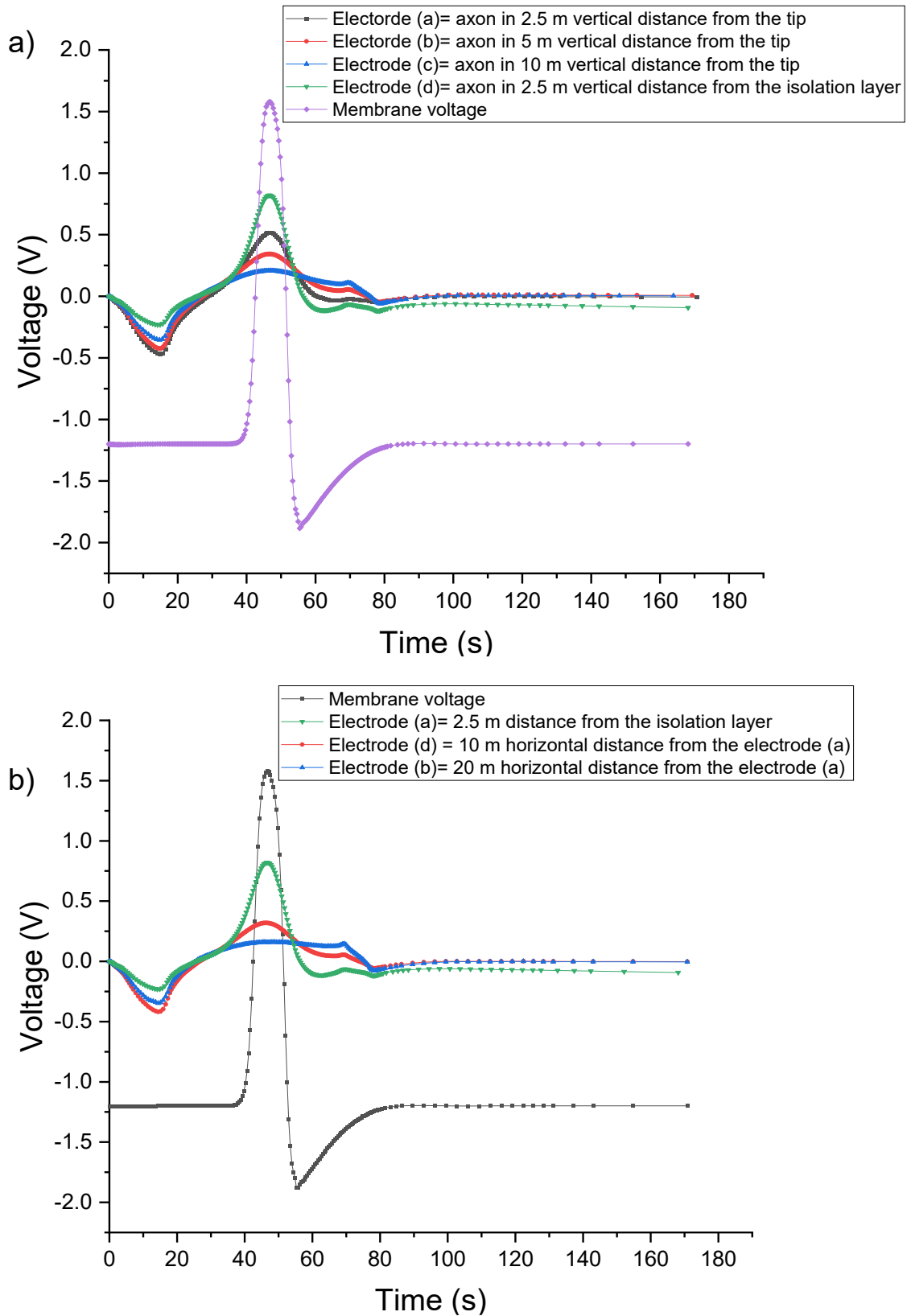


Figure 41. Distance effect of the axon from 3D MEA. Plot (a) depicts the effect of vertical distance from the axon to the electrodes and figure (b) shows the effect of horizontal distance on the obtained voltage by the microelectrode

4.4.3 Multiple axon

Figure 43 depicts the simulation model of a 3D MEA dish with pillar microelectrodes and two axons at different vertical distances from the bottom of the MEA dish, and the AP simulation results. The neuron from the left side was stimulated by applying the stimulus which has been at 2.5-meter vertical distance from the bottom of the MEA. The upper axon was stimulated with a 20-second lag from the first axon stimulation and the axon 2 was placed at 5-meter vertical distance from the bottom, as illustrated in Figure 42. The simulated signals resulting from APs in both axons recorded by the different selected microelectrodes are illustrated in Figure 44. Although all the labeled electrodes were at the equal distance from the primary axon, the signal recorded via the electrodes A and C exhibit a lower amplitude of the first recorded action potential. This occurred due to the initial membrane potential of the second axon (-1.2 V) which is located near distance to the designated electrodes. The effect of the distance of the axon from the electrode on the detected voltage can be seen in the second recognized AP in electrode A and C (Figure 44). Figure 42 presents the recorded voltage by single microelectrode (A) and the corresponding action potential on the axon. As the initial voltages of the solution and microelectrodes were selected to the 0 V and -1.2 V for both axons, a down-stroke in the recorded voltage has occurred at the beginning of the recording.

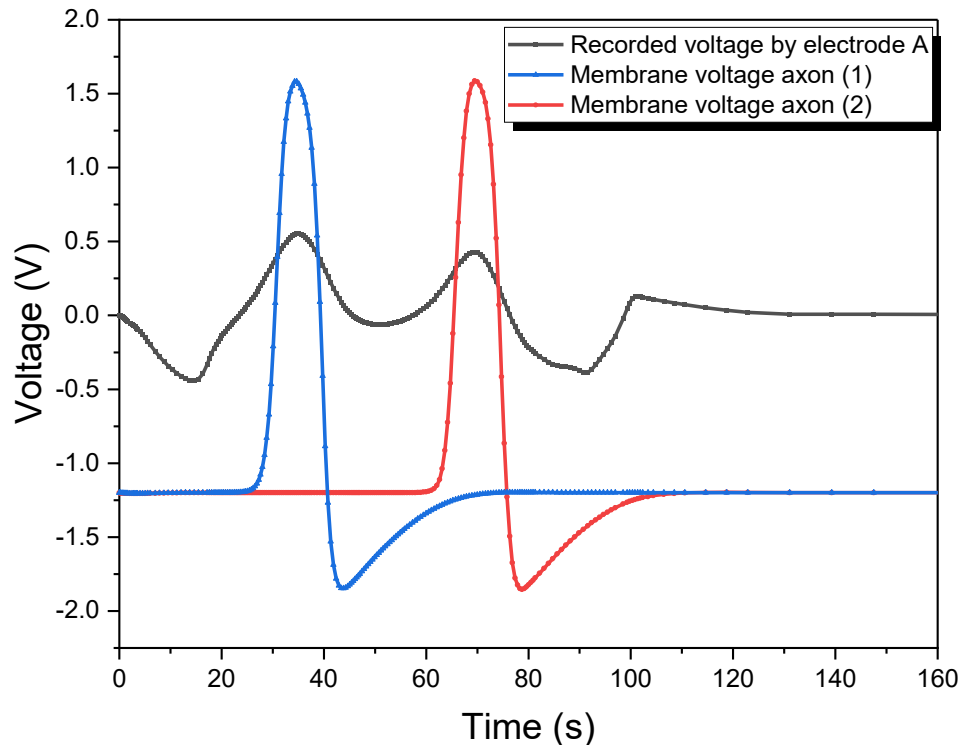


Figure 42. A simulated recorded signal by the 3D pillar microelectrode A (Figure 42) and the corresponding membrane voltage in the axon 1 and axon 2.

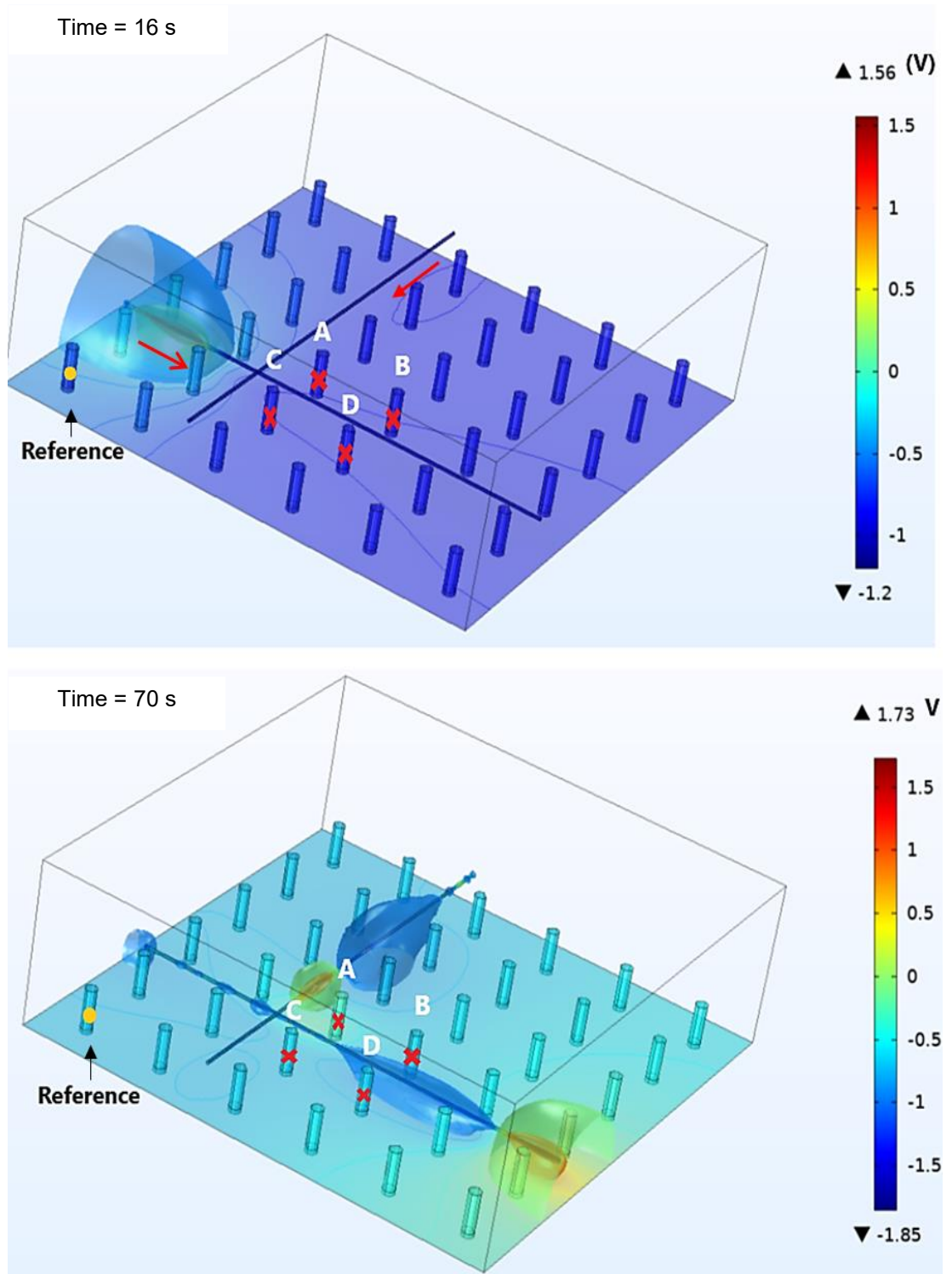


Figure 43. Two axons coupled to a 3D MEA with pillar electrodes, and the simulated electric field potentials due to the APs. The simulated recordings via the electrodes A, B, C, and D are shown in Figure 43.

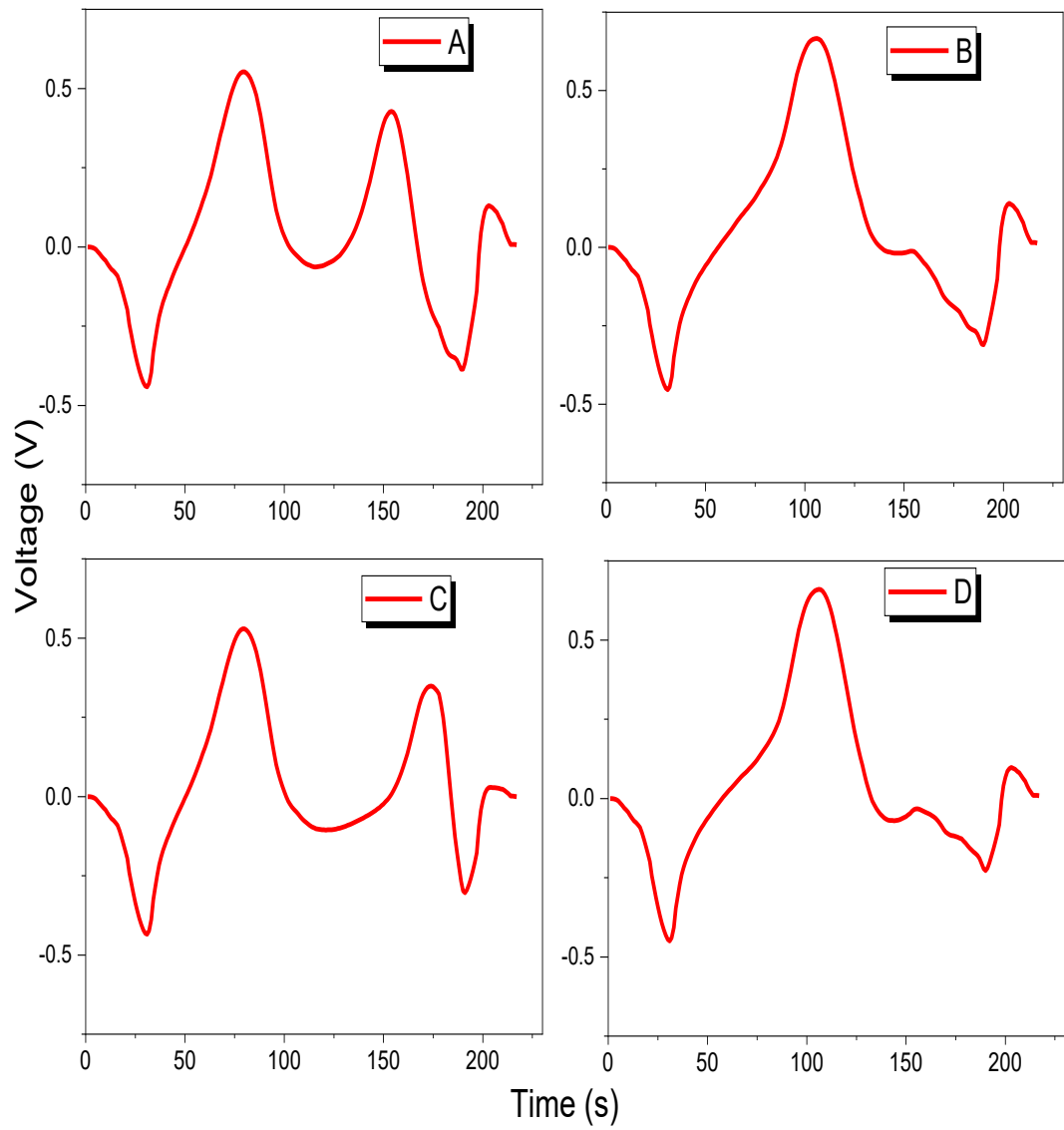


Figure 44. The simulated recorded signals by the 3D pillar electrodes marked in Figure 42 for the two-axon simulation.

5. DISCUSSIONS

This work aimed at constructing a simulator to compare the standard 2D MEA and the newer 3D MEA by utilizing FEM modelling, as well as the factors influencing the final recorded signal. In the beginning, AP propagation along a single scaled axon was simulated by employing the F-N equations in COMSOL. The simulated AP propagating along the 3D cylindrical axon exhibited the known dynamics of the APs such as initial depolarization and repolarization (Figure 22)(Figure 3) [42][47]. The speed of the AP was calculated based on the time difference between observing an AP at different locations on the axon (Figure 23). This speed showed an agreement with the signal speed in the unmyelinated axon, which is around 0.5-2.0 m/s [130]. To include the effects of the surrounding extracellular medium in this simulation, electrostatic physic was recruited. Figure 24 depicts the gradient of the electrical field inside the NaCl solution based on Gauss's law (equations (23), (24), and (25)). Figure 24 depicts the variation of voltage concerning the distance, charge density, and defined relative permittivity inside the solution as expected.

Several stimuli with different amplitudes were applied to the axon with the natural size to assess the feasibility of the F-N model with the defined system parameters [65]. The high amplitude stimuli generated APs with the same amplitude and duration of the AP pulse as obtained in the scaled axon. However, the real duration and amplitude of the neuronal action potential is around 0.4 ms and 35 mV, respectively[131]. Moreover, the lower stimulus could not succeed to activate the axon (Figure 26). These issues were due to that the F-N model is a simplified and dimensionless version of the H-H model, which focuses mostly on the dynamics of the AP on the unmyelinated giant squid axon[64][63]. An essential part of work was confirming the F-N 3D simulation results by executing the F-N model in the MATLAB with the same parameters and the initial conditions as used in the 3D model in COMSOL. The MATLAB results in Figure 27 are in quite good agreement with those given by the three-dimensional COMSOL model (Figure 22).

In the next phase, a system consisting of a MEA and an axon with a propagating AP was simulated. Initially, for making the simulation more realistic and compatible with the F-N equation, all the elements and the electrical properties were scaled proportionally to their original values by considering equations (28) and (29). To be able to define electrical conductivities of the used materials and the appropriate boundary conditions in the medium-electrode interface, electric current physics was used in COMSOL. In this physics, an electrical double layer was established by using distributed impedance (equation 27) and implementing the corresponding impedance and capacitance values represented in

Figure 15. In Figure 29 is shown one of the main results of this work. This signal is the averaged voltage from the surrounding environment of the microelectrodes, obtained by placing the domain point probes at the 2D MEA with respect to the reference electrode. Recorded voltage has the same dynamic as the corresponding membrane voltage. Figure 29a reveals the sudden upstroke voltage change and following that, a depolarization in the membrane which changed the other coupled element's voltage. Recorded pulse has a lower amplitude due to the distance between the axon and the electrode, the electrical conductivity of the solution, the resistance of the electrode, and the impedance of the electrical double layer in the electrode-medium interface (which all these components called effective electrode impedance in [71](Figure 9)).

One of the factors affecting the simulated recorded voltage that we examined with this model was the neuron-electrode distance. The results of these simulations showed agreement with the Ohm's law and volume conductor theory inside the extracellular medium [86](Figures 31,32,41,42).As the neuron-microelectrode distance increased (in both vertical and horizontal), the intensity of the recorded signal decreased. Based on Maxwell's equations of electromagnetism inside the solution with respect to the Laplace boundary condition, recorded voltage have an inverse relation with neuron-medium distance [71][86] (equations (15), (16)).

Following these investigations, a simulation of the 3D MEA was implemented in COM-SOL with pillar electrodes corresponded to those constructed in [101]. Comparative results between the planar and 3D pillar electrodes based on the geometry effect have been executed in two sections; (a) with single microelectrodes, and (b) microelectrodes in full MEA models. The reason that this part was studied in two sections was to focus on the geometry effect of the microelectrodes and neglect the other potential factors which can modify the signal. In the single microelectrode study, physical and electrical properties were considered the same for both types of microelectrodes. Figures 39 and 37 demonstrated that how the 3D microelectrodes surrounded spatially with extracellular medium compared to the planar MEA. From both simulation cases (a) and (b) it was concluded that 3D electrodes with larger surface area than that of planar electrodes lead to reduction in the recorded signal (Figures 38 and 40). This is due to the direct relationship between the bigger surface area and spatial averaging from the larger extracellular medium volume with wider variety of the voltages (equations (15) and (16)) as expected [71][19][70][1].

Another topic that was studied in this work was implementing multiple axons in the vicinity of microelectrodes. In Figures 34 and 44, it is seen that such cases can result in complex recorded compound AP waveforms. After analysing these two figures, it can be

understood that not only the geometry and neuron distance but also the number of simultaneously active nearby neurons can modify the shapes of the detected APs. This topic confirmed that how the population of the neurons can make the measurements more complicated to analysis and influence the specificity and selectivity of the MEAs [9]. The aforementioned parameters are the critical issues in studying the brain mechanisms and assigning recorded spikes to their source neurons (called spike sorting)[1][132].

In nutshell, the simplicity, predictive power, and acceptable computational power requirements make this 3D model suitable to study the extracellular medium and microelectrodes. Moreover, this model provided the freedom to change the biological and physical properties of the elements, allocate different materials and study their effects on the electrical recordings from the neurons. Subsequently, these simulations can help in the optimization of the microelectrodes [61].

One of the primary limitations which has been experienced in this work was the extensive run-time of the simulation. This problem occurred due to using electric current physics and F-N simulation in the whole physical dimension of the system, combined with high-quality elements in the meshing. Also, fine size meshes were employed in this work due to some low-quality elements in the meshes with coarser size. Furthermore, the defined physics was solved fully coupled in one study in COMSOL, which caused the runtime to exceed three days. To solve this problem, the COMSOL model was set up to solve the F-N equations and electric current physics in two separate studies in one simulation. Although finer-element meshes were defined in both 2D and 3D MEA simulations, the runtime decreased to 30-60 minutes. Another limitation that was faced in this simulation was the scaled-up geometry due to the F-N model. Moreover, the expanded surface area at the interface of the medium electrode decreases the impedance of a double electrical layer. Consequently, the effect of the double electrical layer at different electrode-medium interfaces have not revealed big differences in the results.

In future studies, the implementation of the H-H model can be considered to scale down the whole system to the real size and study the AP with the real duration and amplitude. Moreover, noise models and effective impedances can be studied in the frequency domain of the COMSOL.

6. SUMMARY

One of the objectives of this work was to assess the performances of the MEAs with respect to differences in the recorded AP waveforms via the different electrodes by employing 3D FEM modeling. First, F-N equations were employed for simulating the traveling AP along the scaled axon. Next, the F-N model for the AP propagation along the axon with the natural size was studied. The results confirmed the inapplicability of the F-N model in the neuron with the natural size. Consequently, all the elements and the electrical properties were scaled up. AC/DC modules were utilized for modeling the extracellular medium coupled to the MEA. Appropriate electrical properties and boundary conditions were defined by employing electric current physics. A fine mesh was established to the whole geometry; however, the runtime was kept noticeably low by utilizing separate solvers for the equations and physics. COMSOL solves the action potential at each discretized element of the system and electrodes measure the spatially averaged potential across all surrounding environment. Electrical double layer at the interface of the electrode-solution was assigned by using a distributed impedance boundary condition. The FEM models worked well to simulate APs recorded by microelectrodes. 2D and 3D MEAs were compared by analyzing the influence of the geometry on the simulated detected signal. 3D MEA recorded the APs with lower amplitude due to the higher surface area which leads to larger averaging. Furthermore, these 3D structures surrounded by the environment which has a wider range of voltage distribution.

Further, another aim of this thesis was to study the environmental effect of the mentioned microelectrodes on the detected signals. First, several simulations were performed by changing the distance of the neurons from the electrode. The result of these analyses revealed a compatible agreement with the rewritten Maxwell equations for the electromagnetism. The biological factor in the environment was the multiple axons that were targeted for simulation. Recorded APs from multiple axons were investigated based on the simulated measured AP waveforms.

To sum up, the results of these 3D models confirmed that the geometry of the electrodes, as well as the physical and biological environment, influence the final recorded voltage. Description of aforementioned models can provide a good toolset for designing the MEAs as well as predicting the detected signal based on the potential factors will advance the neurophysiological studies such as disease modelling, toxicity testing, drug testing, spike sorting. In future works, it would be interesting to study the more realistic 3D models

based on the Hodgkin-Huxley model via considering run-time, introducing more complex neuronal networks and noise models.

REFERENCES

- [1] A. Bhatti, K. H. Lee, H. G. Chee, and P. Lim, "Series in BioEngineering Emerging Trends in Neuro Engineering and Neural Computation," .
- [2] F. E. Kapucu, "Methods to Enhance Information Extraction from Microelectrode Array Measurements of Neuronal Networks Fikret Emre Kapucu Methods to Enhance Information Extraction from Microelectrode Array Measurements of Neuronal Networks Julkaisu 1438 • Publication 1438," Tampere unoversity of Technology, 2016.
- [3] M. Frega, *In vitro neuronal networks*. 2016.
- [4] A. F. M. Johnstone, G. W. Gross, D. G. Weiss, O. H. U. Schroeder, A. Gramowski, and T. J. Shafer, "Microelectrode arrays: A physiologically based neurotoxicity testing platform for the 21st century," *Neurotoxicology*, vol. 31, no. 4, pp. 331–350, 2010, doi: 10.1016/j.neuro.2010.04.001.
- [5] A. H. Marblestone *et al.*, "Physical principles for scalable neural recording," *Front. Comput. Neurosci.*, vol. 7, no. OCT, pp. 1–34, 2013, doi: 10.3389/fncom.2013.00137.
- [6] Y. Nam and B. C. Wheeler, "In Vitro Microelectrode Array Technology and Neural Recordings," vol. 39, no. 1, pp. 45–61, 2011.
- [7] J. Pine, "Recording action potentials from cultured neurons with extracellular microcircuit electrodes," *J. Neurosci. Methods*, vol. 2, no. 1, pp. 19–31, 1980, doi: 10.1016/0165-0270(80)90042-4.
- [8] G. W. Gross, A. N. Williams, and J. H. Lucas, "Recording of spontaneous activity with photoetched microelectrode surfaces from mouse spinal neurons in culture," *J. Neurosci. Methods*, vol. 5, no. 1–2, pp. 13–22, 1982, doi: 10.1016/0165-0270(82)90046-2.
- [9] K. H. Lee, *Emerging trends in neuro engineering and neural computation*. 2017.
- [10] S. Marom and G. Shahaf, "Development, learning and memory in large random networks of cortical neurons: Lessons beyond anatomy," *Q. Rev. Biophys.*, vol. 35, no. 1, pp. 63–87, 2002, doi: 10.1017/S0033583501003742.
- [11] N. Joye, A. Schmid, and Y. Leblebici, "Electrical modeling of the cell-electrode interface for recording neural activity from high-density microelectrode arrays," *Neurocomputing*, vol. 73, no. 1–3, pp. 250–259, 2009, doi: 10.1016/j.neucom.2009.09.006.
- [12] C. A. Thomas, P. A. Springer, G. E. Loeb, Y. Berwald-Netter, and L. M. Okun, "A miniature microelectrode array to monitor the bioelectric activity of cultured cells," *Exp. Cell Res.*, vol. 74, no. 1, pp. 61–66, 1972, doi: 10.1016/0014-4827(72)90481-8.
- [13] J. T. Robinson, M. Jorgolli, and H. Park, "Nanowire electrodes for high-density stimulation and measurement of neural circuits," *Front. Neural Circuits*, vol. 7, no.

FEBRUARY 2013, pp. 1–5, 2013, doi: 10.3389/fncir.2013.00038.

- [14] V. Emmenegger, M. E. J. Obien, F. Franke, and A. Hierlemann, “Technologies to study action potential propagation with a focus on HD-MEAs,” *Front. Cell. Neurosci.*, vol. 13, no. April, pp. 1–11, 2019, doi: 10.3389/fncel.2019.00159.
- [15] C. Gold, D. A. Henze, C. Koch, and G. Buzsáki, “On the origin of the extracellular action potential waveform: A modeling study,” *J. Neurophysiol.*, vol. 95, no. 5, pp. 3113–3128, 2006, doi: 10.1152/jn.00979.2005.
- [16] S. Zarrabi, “MODELING AND DESIGN OF LOW IMPEDANCE MICROELECTRODES FOR BIOMEDICAL APPLICATIONS,” University of California, 2013.
- [17] N. A. Pelot, B. J. Thio, and W. M. Grill, “Modeling current sources for neural stimulation in COMSOL,” *Front. Comput. Neurosci.*, vol. 12, no. June, pp. 1–14, 2018, doi: 10.3389/fncom.2018.00040.
- [18] M. Böttrich, J. M. A. Tanskanen, and J. A. K. Hyttinen, “Lead field theory provides a powerful tool for designing microelectrode array impedance measurements for biological cell detection and observation,” *Biomed. Eng. Online*, vol. 16, no. 1, pp. 1–17, 2017, doi: 10.1186/s12938-017-0372-5.
- [19] A. Furniturewalla, P. Rustogi, E. Patrick, and J. W. Judy, “Modeling the Recording of Intra-neural Action Potentials with Microelectrodes Using FEM and Point-Source Methods,” *Int. IEEE/EMBS Conf. Neural Eng. NER*, vol. 2019-March, pp. 1191–1194, 2019, doi: 10.1109/NER.2019.8717121.
- [20] R. Appali, K. K. Sriperumbudur, and U. Van Rienen, “3D axonal network coupled to Microelectrode Arrays: A simulation model to study neuronal dynamics,” *Proc. Annu. Int. Conf. IEEE Eng. Med. Biol. Soc. EMBS*, vol. 2015-Novem, pp. 4700–4704, 2015, doi: 10.1109/EMBC.2015.7319443.
- [21] S. Joucla, A. Glière, and B. Yvert, “Current approaches to model extracellular electrical neural microstimulation,” *Front. Comput. Neurosci.*, vol. 8, no. FEB, pp. 1–12, 2014, doi: 10.3389/fncom.2014.00013.
- [22] Orjan G. Martinsen; Sverre Grimnes, *Bioimpedance and Bioelectricity Basic*, 3rd ed. Academic Press, 2014.
- [23] R. Appali, “Modeling the Coupling of Action Potential and Electrodes,” 2013.
- [24] R. P. Jakko Malmivuo, “Active behavior of the membrane,” in *Bioelectromagnetism*, 1995, pp. 66–103.
- [25] C. Lee *et al.*, *K. Arms, P. Camp, Biology*. 1995.
- [26] F. D. Schadé JP, *Basic Neurology*, 2nd ed. Nature Publishing Group.
- [27] P. L. Nunez and R. Srinivasan, *Electric Fields of the Brain: The neurophysics of EEG*. 2009.
- [28] Marc L. DuBois., Ed., *ACTION POTENTIAL : BIOPHYSICAL AND CELLULAR CONTEXT , INITIATION , PHASES AND PROPAGATION*. New York: Nova Science, 2010.

- [29] B. (University of W. Hille, *Ion Channels of Excitable Membranes*, Third. Sunderland, Massachusetts: Sinauer Associates, 2001.
- [30] S. Poliak and E. Peles, "The local differentiation of myelinated axons at nodes of ranvier," *Nat. Rev. Neurosci.*, vol. 4, no. 12, pp. 968–980, 2003, doi: 10.1038/nrn1253.
- [31] J. L. Salzer, P. J. Brophy, and E. Peles, "Molecular domains of myelinated axons in the peripheral nervous system," *Glia*, vol. 56, no. 14, pp. 1532–1540, 2008, doi: 10.1002/glia.20750.
- [32] Thompson CF, *The brain-An Introduction to Neuroscience*. New York: W. H. Freeman, 1985.
- [33] R. J. Reynolds and J. W. Heath, "Patterns of morphological variation within myelin internodes of normal peripheral nerve: quantitative analysis by confocal microscopy.," *J. Anat.*, vol. 187 (Pt 2, pp. 369–78, 1995.
- [34] M. Rydmark and C.-H. Berthold, "Electron microscopic serial section analysis of nodes of Ranvier in lumbar spinal roots of the cat: A morphometric study of nodal compartments in fibres of different sizes," *J. Neurocytol.*, vol. 12, no. 4, pp. 537–565, 1983, doi: 10.1007/BF01181523.
- [35] S. Y. Chiu and J. M. Ritchie, "On the physiological role of internodal potassium channels and the security of conduction in myelinated nerve fibers," *Proc. R. Soc. London - Biol. Sci.*, vol. 220, no. 1221, pp. 415–422, 1984, doi: 10.1098/rspb.1984.0010.
- [36] J. M. Ritchie and R. B. Rogart, "Density of sodium channels in mammalian myelinated nerve fibers and nature of the axonal membrane under the myelin sheath," *Proc. Natl. Acad. Sci. U. S. A.*, vol. 74, no. 1, pp. 211–215, 1977, doi: 10.1073/pnas.74.1.211.
- [37] E. Gagnon, D. A. Schubert, S. Gordo, H. H. Chu, and K. W. Wucherpennig, "Local changes in lipid environment of TCR microclusters regulate membrane binding by the CD3 ϵ cytoplasmic domain," *J. Exp. Med.*, vol. 209, no. 13, pp. 2423–2439, 2012, doi: 10.1084/jem.20120790.
- [38] S. Yorulmaz, J. A. Jackman, W. Hunziker, and N. J. Cho, "Influence of membrane surface charge on adsorption of complement proteins onto supported lipid bilayers," *Colloids Surfaces B Biointerfaces*, vol. 148, pp. 270–277, 2016, doi: 10.1016/j.colsurfb.2016.08.036.
- [39] S. A. Rajasekaran *et al.*, "Na,K-ATPase β -subunit is required for epithelial polarization, suppression of invasion, and cell motility," *Mol. Biol. Cell*, vol. 12, no. 2, pp. 279–295, 2001, doi: 10.1091/mbc.12.2.279.
- [40] L. Li *et al.*, "Expression of the β 3 subunit of Na⁺/K⁺-ATPase is increased in gastric cancer and regulates gastric cancer cell progression and prognosis via the PI3/AKT pathway," *Oncotarget*, vol. 8, no. 48, pp. 84285–84299, 2017, doi: 10.18632/oncotarget.20894.
- [41] C. L. Mann and J. A. Cidlowski, "Glucocorticoids regulate plasma membrane potential during rat thymocyte apoptosis in vivo and in vitro," *Endocrinology*, vol. 142, no. 1, pp. 421–429, 2001, doi: 10.1210/endo.142.1.7904.

- [42] Marc L. DuBois, Ed., *Action potential : biophysical and cellular context, initiation, phases, and propagation*. New York: Nova Science, 2010.
- [43] D. Gradmann and J. Hoffstadt, "Electrocoupling of ion transporters in plants: Interaction with internal ion concentrations," *J. Membr. Biol.*, vol. 166, no. 1, pp. 51–59, 1998, doi: 10.1007/s002329900446.
- [44] Nernst WH, *Zur Kinetik der Lösung befindlichen Körper: Theorie der Diffusion. Z. Phys. Chem.* 3. 1888.
- [45] "Neurons & the Nervous System." .
- [46] D. Gradmann, "'Metabolic' action potentials in Acetabularia," *Membr. Biol.* 29, pp. 23–24, 1976.
- [47] M. Boron, Walter F., MD, PhD; Boulpaep, Emile L., "Electrical Excitability and Action Potentials," in *Medical Physiology*, 23rd ed., New Haven, Connecticut: Elsevier, 2017, pp. 173–203.
- [48] T. L. L. Solomon D. Erulkar, "Action potential," *Encyclopædia Britannica, inc.*, 201AD. .
- [49] H. Dziubińska, K. Trębacz, and T. Zawadzki, "Transmission route for action potentials and variation potentials in *Helianthus annuus* L.," *J. Plant Physiol.*, vol. 158, no. 9, pp. 1167–1172, 2001, doi: 10.1078/S0176-1617(04)70143-1.
- [50] A. Odawara, Y. Saitoh, A. H. Alhebshi, M. Gotoh, and I. Suzuki, "Long-term electrophysiological activity and pharmacological response of a human induced pluripotent stem cell-derived neuron and astrocyte co-culture," *Biochem. Biophys. Res. Commun.*, vol. 443, no. 4, pp. 1176–1181, 2014, doi: 10.1016/j.bbrc.2013.12.142.
- [51] R. C. Barr and R. Plonsey, "Action potentials," in *Bioelectricity, A Quantitative Approach*, Third., Durham, North Carolina: Springer Science+Business Media, 2007, pp. 97–153.
- [52] J. R. Schwarz, G. Reid, and H. Bostock, "Action potentials and membrane currents in the human node of Ranvier," *Pflügers Arch. Eur. J. Physiol.*, vol. 430, no. 2, pp. 283–292, 1995, doi: 10.1007/BF00374660.
- [53] M. Baker, H. Bostock, P. Grafe, P. Martius, and Q. Square, "Function and distribution of three types of rectifying channel in rat spinal root myelinated axons.," *J Phy*, no. 383, pp. 45–67, 1987.
- [54] C. Guyton and John E. Hall, "Membrane Physiology, Nerve, and Muscle," in *Guyton and Hall Textbook of Medical Physiology*, 12th ed., R. Gruliow and L. Stingelin, Eds. Philadelphia: SAUNDERS elsevier, 2011, pp. 57–69.
- [55] R. D. Keynes and P. R. Lewis, "The sodium and potassium content of cephalopod nerve fibres," *J. Physiol.*, vol. 114, no. 1–2, pp. 151–182, 1951, doi: 10.1113/jphysiol.1951.sp004609.
- [56] M. A. Rothenberg, "Studies on permeability in relation to nerve function II. ionic movements across axonal membranes," *BBA - Biochim. Biophys. Acta*, vol. 4, no. C, pp. 96–114, 1950, doi: 10.1016/0006-3002(50)90012-6.

- [57] A. L. Hodgkin and A. F. Huxley, "Currents carried by sodium and potassium ions through the membrane of the giant axon of *Loligo*," *J. Physiol.*, vol. 116, no. 4, pp. 449–472, 1952, doi: 10.1113/jphysiol.1952.sp004717.
- [58] A. L. Hodgkin and A. F. Huxley, "A quantitative description of membrane current and its application to conduction and excitation in nerve," *J. Physiol*, pp. 500–544, 1952.
- [59] R. Plonsey and R. C. Barr, "Impulse Propagation," in *Bioelectricity, A Quantitative Approach*, 2007, pp. 155–185.
- [60] R. Hahn, "Action potential production: AN ION CHANNEL DEPENDENT PROCESS," in *Action potential*, 2010, pp. 99–131.
- [61] R. Appali, "Modeling the Coupling of Action Potential and Electrodes," 2013.
- [62] Y. Zhao, S. A. Billings, Y. Guo, D. Coca, L. L. Dematos, and R. I. Ristic, "Spatio-temporal modeling of wave formation in an excitable chemical medium based on a revised fitzhughnagumo model," 2011.
- [63] R. FitzHugh, "Impulses and Physiological States in Theoretical Models of Nerve Membrane," *Biophys. J.*, vol. 1, no. 6, pp. 445–466, 1961, doi: 10.1016/S0006-3495(61)86902-6.
- [64] J. Nagumo, S. Arimoto, and S. Yoshizawa, "An Active Pulse Transmission Line Simulating Nerve Axon*," *Proc. IRE*, vol. 50, no. 10, pp. 2061–2070, 1962, doi: 10.1109/JRPROC.1962.288235.
- [65] E. B. Postnikov and O. V. Titkova, "A correspondence between the models of Hodgkin-Huxley and FitzHugh-Nagumo revisited," *Eur. Phys. J. Plus*, vol. 131, no. 11, pp. 1–9, 2016, doi: 10.1140/epjp/i2016-16411-1.
- [66] J. J. Tyson and P. Keener, "SINGULAR PERTURBATION (A REVIEW)* John J. TYSON," vol. 32, pp. 327–361, 1988.
- [67] T. Belousov-zhabotinskii, "On Travelling Wave Solutions in a Model for the Belousov-Zhabotinskii Reaction," pp. 329–353, 1976.
- [68] C. Luo and Y. Rudy, "A Dynamic Model of the Cardiac Ventricular Action Potential Simulations of Ionic Currents and Concentration Changes," 1985.
- [69] W. K. Chandler, R. Fitzhugh, and K. S. Cole, "Theoretical Stability Properties of a Space-Clamped Axon," *Biophys. J.*, vol. 2, no. 2, pp. 105–127, 1962, doi: 10.1016/S0006-3495(62)86844-1.
- [70] M. E. Spira and A. Hai, "Multi-electrode array technologies for neuroscience and cardiology," *Nat. Nanotechnol.*, vol. 8, no. 2, pp. 83–94, 2013, doi: 10.1038/nnano.2012.265.
- [71] M. E. J. Obien, K. Deligkaris, T. Bullmann, D. J. Bakkum, and U. Frey, "Revealing neuronal function through microelectrode array recordings," *Front. Neurosci.*, vol. 9, no. JAN, p. 423, 2015, doi: 10.3389/fnins.2014.00423.
- [72] M. S. Fee, P. P. Mitra, and D. Kleinfeld, "Automatic sorting of multiple unit neuronal signals in the presence of anisotropic and non-Gaussian variability," vol. 69, pp. 175–188, 1996.

- [73] E. N. Brown, R. E. Kass, and P. P. Mitra, "Multiple neural spike train data analysis : state-of- the-art and future challenges," vol. 7, no. 5, pp. 456–461, 2004, doi: 10.1038/nn1228.
- [74] G. W. Gross, "Simultaneous Single Unit Recording in vitro with a Photoetched Laser Deinsulated Gold Multimicroelectrode Surface," *IEEE Trans. Biomed. Eng.*, vol. BME-26, no. 5, pp. 273–279, 1979, doi: 10.1109/TBME.1979.326402.
- [75] E. R. McConnell, M. A. McClain, J. Ross, W. R. LeFew, and T. J. Shafer, "Evaluation of multi-well microelectrode arrays for neurotoxicity screening using a chemical training set," *Neurotoxicology*, vol. 33, no. 5, pp. 1048–1057, 2012, doi: 10.1016/j.neuro.2012.05.001.
- [76] G. Buzsáki, C. A. Anastassiou, and C. Koch, "The origin of extracellular fields and currents-EEG, ECoG, LFP and spikes," *Nat. Rev. Neurosci.*, vol. 13, no. 6, pp. 407–420, 2012, doi: 10.1038/nrn3241.
- [77] U. Frey, U. Egert, F. Heer, S. Hafizovic, and A. Hierlemann, "Microelectronic system for high-resolution mapping of extracellular electric fields applied to brain slices," *Biosens. Bioelectron.*, 2009, doi: 10.1016/j.bios.2008.11.028.
- [78] W. L. C. Rutten, T. G. Ruardij, E. Marani, and B. H. Roelofsen, "Neural networks on chemically patterned electrode arrays: Towards a cultured probe," *Acta Neurochir. Suppl.*, vol. 97, no. 97 PART 2, pp. 547–554, 2007, doi: 10.1007/978-3-211-33081-4_63.
- [79] A. Stett *et al.*, "Biological application of microelectrode arrays in drug discovery and basic research," *Anal. Bioanal. Chem.*, vol. 377, no. 3, pp. 486–495, 2003, doi: 10.1007/s00216-003-2149-x.
- [80] G. W. Gross, B. K. Rhoades, D. L. Reust, and F. U. Schwalm, "Stimulation of monolayer networks in culture through thin-film indium-tin oxide recording electrodes," *J. Neurosci. Methods*, vol. 50, no. 2, pp. 131–143, 1993, doi: 10.1016/0165-0270(93)90001-8.
- [81] F. J. L. Arnold, F. Hoffmann, C. P. Bengtson, M. Wittmann, P. Vanhoutte, and H. Bading, "Microelectrode array recordings of cultured hippocampal networks reveal a simple model for transcription and protein synthesis-dependent plasticity," *J. Physiol.*, vol. 564, no. 1, pp. 3–19, 2005, doi: 10.1113/jphysiol.2004.077446.
- [82] M. Chiappalone, P. Massobrio, and S. Martinoia, "Network plasticity in cortical assemblies," *Eur. J. Neurosci.*, vol. 28, no. 1, pp. 221–237, 2008, doi: 10.1111/j.1460-9568.2008.06259.x.
- [83] F. Hofmann and H. Bading, "Long term recordings with microelectrode arrays: Studies of transcription-dependent neuronal plasticity and axonal regeneration," *J. Physiol. Paris*, vol. 99, no. 2–3, pp. 125–132, 2006, doi: 10.1016/j.jphysparis.2005.12.005.
- [84] I. Vajda *et al.*, "Low-frequency stimulation induces stable transitions in stereotypical activity in cortical networks," *Biophys. J.*, vol. 94, no. 12, pp. 5028–5039, 2008, doi: 10.1529/biophysj.107.112730.
- [85] A. J. Cadotte, T. B. DeMarse, P. He, and M. Ding, "Causal measures of structure and plasticity in simulated and living neural networks," *PLoS One*, vol. 3, no. 10,

- 2008, doi: 10.1371/journal.pone.0003355.
- [86] M. Frega, *In Vitro Neuronal Networks*. 2016.
- [87] R. Huys *et al.*, "Single-cell recording and stimulation with a 16k micro-nail electrode array integrated on a 0.18 μm CMOS chip," *Lab Chip*, vol. 12, no. 7, pp. 1274–1280, 2012, doi: 10.1039/c2lc21037a.
- [88] B. Eversmann *et al.*, "A 128 \times 128 CMOS Biosensor Array for Extracellular Recording of Neural Activity," *IEEE J. Solid-State Circuits*, vol. 38, no. 12, pp. 2306–2317, 2003, doi: 10.1109/JSSC.2003.819174.
- [89] M. Hutzler *et al.*, "High-Resolution Multitransistor Array Recording of Electrical Field Potentials in Cultured Brain Slices High-Resolution Multitransistor Array Recording of Electrical Field Potentials in Cultured Brain Slices," no. May 2006, pp. 1638–1645, 2006, doi: 10.1152/jn.00347.2006.
- [90] L. Berdondini, K. Imfeld, A. Maccione, M. Tedesco, and S. Neukom, "Active pixel sensor array for high spatio-temporal resolution electrophysiological recordings from single cell to large scale neuronal networks †," vol. 9, no. 18, 2009, doi: 10.1039/b907394a.
- [91] C. Hassler, T. Boretius, and T. Stieglitz, "Polymers for Neural Implants," vol. i, pp. 18–33, 2011, doi: 10.1002/polb.22169.
- [92] S. F. Cogan, A. A. Guzelian, W. F. Agnew, T. G. H. Yuen, and D. B. McCreery, "Over-pulsing degrades activated iridium oxide films used for intracortical neural stimulation," vol. 137, pp. 141–150, 2004, doi: 10.1016/j.jneumeth.2004.02.019.
- [93] S. F. Cogan, "Neural Stimulation and Recording Electrodes," *Annu. Rev. Biomed. Eng.*, vol. 10, no. 1, pp. 275–309, 2008, doi: 10.1146/annurev.bioeng.10.061807.160518.
- [94] S. Rajaraman *et al.*, "Metal-Transfer-Micromolded Three-Dimensional Brain-Slice Recordings," vol. 20, no. 2, pp. 396–409, 2011.
- [95] and C. S. W. S. A. Boppart, B. C. Wheeler, "A flexible perforated microelectrode array for extended neural recordings m," *IEEE Trans. Biomed. Eng.*, vol. 39, pp. 37–42, 1992.
- [96] Y. Nam, B. C. Wheeler, and M. O. Heuschkel, "Neural recording and stimulation of dissociated hippocampal cultures using microfabricated three-dimensional tip electrode array," *J. Neurosci. Methods*, vol. 155, no. 2, pp. 296–299, 2006, doi: 10.1016/j.jneumeth.2006.01.014.
- [97] A. Vassallo *et al.*, "A multi-laboratory evaluation of microelectrode array-based measurements of neural network activity for acute neurotoxicity testing," *Neurotoxicology*, 2017, doi: 10.1016/j.neuro.2016.03.019.
- [98] J. R. Buitenweg, W. L. C. Rutten, W. P. A. Willems, and J. W. Van Nieuwkastele, "Measurement of sealing resistance of cell-electrode interfaces in neuronal cultures using impedance spectroscopy," *Med. Biol. Eng. Comput.*, vol. 36, no. 5, pp. 630–637, 1998, doi: 10.1007/BF02524436.
- [99] S. M. Potter, D. A. Wagenaar, and T. B. Demarse, *Closing the Loop : Stimulation Feedback Systems for Embodied MEA Cultures From: Advances in Network*

Electrophysiology Using Multi-Electrode Arrays Makoto Taketani and Michel Baudry, Editors *CLOSING THE LOOP : STIMULATION FEEDBACK SYSTEMS FOR EMBODIED ME*, no. January. 2006.

- [100] M. O. Heuschkel, M. Fejtl, M. Raggenbass, D. Bertrand, and P. Renaud, "A three-dimensional multi-electrode array for multi-site stimulation and recording in acute brain slices," *J. Neurosci. Methods*, vol. 114, no. 2, pp. 135–148, 2002, doi: 10.1016/S0165-0270(01)00514-3.
- [101] E. Tomaskovic-Crook *et al.*, "Human Neural Tissues from Neural Stem Cells Using Conductive Biogel and Printed Polymer Microelectrode Arrays for 3D Electrical Stimulation," *Adv. Healthc. Mater.*, vol. 8, no. 15, 2019, doi: 10.1002/adhm.201900425.
- [102] V. Alarautalahti, M. Hiltunen, N. Onnela, S. Nymark, M. Kellomäki, and J. Hyttinen, "Polypyrrole-coated electrodes show thickness-dependent stability in different conditions during 42-day follow-up in vitro," *J. Biomed. Mater. Res. - Part B Appl. Biomater.*, vol. 106, no. 6, pp. 2202–2213, 2018, doi: 10.1002/jbm.b.34024.
- [103] P. Zhang, N. Aydemir, M. Alkaisi, D. E. Williams, and J. Travas-Sejdic, "Direct Writing and Characterization of Three-Dimensional Conducting Polymer PEDOT Arrays," *ACS Appl. Mater. Interfaces*, vol. 10, no. 14, pp. 11888–11895, 2018, doi: 10.1021/acsami.8b02289.
- [104] J. M. Corey, B. C. Wheeler, and G. J. Brewer, "Compliance of hippocampal neurons to patterned substrate networks," *J. Neurosci. Res.*, vol. 30, no. 2, pp. 300–307, 1991, doi: 10.1002/jnr.490300204.
- [105] Y. Nam and B. C. Wheeler, "Imaging locations of neurons vs. glia in low density culture," *2nd Int. IEEE EMBS Conf. Neural Eng.*, vol. 2005, pp. 325–327, 2005, doi: 10.1109/CNE.2005.1419623.
- [106] D. A. Robinson, "The Electrical Properties of Metal Microelectrodes," *Proc. IEEE*, vol. 56, no. 6, pp. 1065–1071, 1968, doi: 10.1109/PROC.1968.6458.
- [107] M. Grattarola and S. Martinoia, "Modeling the Neuron-Microtransducer Junction: From Extracellular to Patch Recording," *IEEE Trans. Biomed. Eng.*, vol. 40, no. 1, pp. 35–41, 1993, doi: 10.1109/10.204769.
- [108] R. Weis and P. Fromherz, "Frequency dependent signal transfer in neuron transistors," *Phys. Rev. E - Stat. Physics, Plasmas, Fluids, Relat. Interdiscip. Top.*, vol. 55, no. 1, pp. 877–889, 1997, doi: 10.1103/PhysRevE.55.877.
- [109] D. J. Bakkum *et al.*, "Tracking axonal action potential propagation on a high-density microelectrode array across hundreds of sites," *Nat. Commun.*, vol. 4, 2013, doi: 10.1038/ncomms3181.
- [110] W. Rutten *et al.*, "Neuroelectronic interfacing with cultured multielectrode arrays toward a cultured probe," *Proc. IEEE*, vol. 89, no. 7, pp. 1013–1029, 2001, doi: 10.1109/5.939810.
- [111] M. J. Nelson, P. Pouget, E. A. Nilsen, C. D. Patten, and J. D. Schall, "Review of signal distortion through metal microelectrode recording circuits and filters," *J. Neurosci. Methods*, vol. 169, no. 1, pp. 141–157, 2008, doi: 10.1016/j.jneumeth.2007.12.010.

- [112] W. Klee, M., Rall, "Computed potentials of cortically arranged populations of neurons," vol. 40, no. 3, pp. 647–666, 1977.
- [113] C. A. Anastassiou, G. Buzsáki, and C. Koch, "Biophysics of extracellular spikes," *Princ. Neural Coding*, pp. 15–36, 2013, doi: 10.1201/b14756.
- [114] M. E. J. Obien, A. Hierlemann, and U. Frey, "Blind Localization of a Stimulation Electrode Using a High-Density Microelectrode Array," *35th Annu. Int. Conf. IEEE EMBS*, p. SaB08.8, 2013.
- [115] G. Grimmes, S., Martinsen, "Geometrical analysis," in *Bioimpedance and Bioelectricity Basic*, Oxford, 2008, pp. 161–204.
- [116] W. Franks, I. Schenker, P. Schmutz, and A. Hierlemann, "Impedance characterization and modeling of electrodes for biomedical applications," *IEEE Trans. Biomed. Eng.*, vol. 52, no. 7, pp. 1295–1302, 2005, doi: 10.1109/TBME.2005.847523.
- [117] J. Esch, "Growing cells atop microelectronic chips: Interfacing electrogenic cells in vitro with CMOS-based microelectrode arrays," *Proc. IEEE*, vol. 99, no. 2, pp. 249–251, 2011, doi: 10.1109/JPROC.2010.2090993.
- [118] L. A. Camuñas-Mesa and R. Q. Quiroga, "A detailed and fast model of extracellular recordings," *Neural Comput.*, vol. 25, no. 5, pp. 1191–1212, 2013, doi: 10.1162/NECO_a_00433.
- [119] S. J. Paik, Y. Park, and D. I. D. Cho, "Roughened polysilicon for low impedance microelectrodes in neural probes," *J. Micromechanics Microengineering*, vol. 13, no. 3, pp. 373–379, 2003, doi: 10.1088/0960-1317/13/3/304.
- [120] M. P. Ward, P. Rajdev, C. Ellison, and P. P. Irazoqui, "Toward a comparison of microelectrodes for acute and chronic recordings," *Brain Res.*, vol. 1282, pp. 183–200, 2009, doi: 10.1016/j.brainres.2009.05.052.
- [121] R. A. Andersen, E. J. Hwang, and G. H. Mulliken, "Cognitive Neural Prosthetics," *Annu. Rev. Psychol.*, vol. 61, no. 1, pp. 169–190, 2010, doi: 10.1146/annurev.psych.093008.100503.
- [122] R. O. Doruk and L. Abosharb, "Estimating the parameters of fitzhugh–nagumo neurons from neural spiking data," *Brain Sci.*, vol. 9, no. 12, 2019, doi: 10.3390/brainsci9120364.
- [123] COMSOL, "Comsol Multiphysics Reference Manual (Version 4.3b)," COMSOL, 2013.
- [124] X. Huang, D. Nguyen, D. W. Greve, and M. M. Domach, "Simulation of microelectrode impedance changes due to cell growth," *IEEE Sens. J.*, vol. 4, no. 5, pp. 576–583, 2004, doi: 10.1109/JSEN.2004.831302.
- [125] T. T. and M. Kurokawa, "Verification of the effect of the axon fluid as a highly dielectric medium in the high-speed conduction of action potentials using a novel axon equivalent circuit," *Biophys. Physicobiology*, vol. 15, pp. 214–228, 2018, doi: 10.2142/biophysico.15.0.
- [126] M. Knudsen, "MEA," 2019. [Online]. Available: <https://www.ntnu.no/wiki/display/cyborg/MEA>. [Accessed: 07-Apr-2020].

- [127] C. M. Lopez *et al.*, “A multimodal CMOS MEA for high-throughput intracellular action potential measurements and impedance spectroscopy in drug-screening applications,” *IEEE J. Solid-State Circuits*, vol. 53, no. 11, pp. 3076–3086, 2018, doi: 10.1109/JSSC.2018.2863952.
- [128] “Mesh quality,” 2009. [Online]. Available: <https://www.afs.enea.it/project/neptunius/docs/fluent/html/ug/node167.htm>. [Accessed: 07-Apr-2020].
- [129] Purves D, Augustine GJ, Fitzpatrick D, “Increased Conduction Velocity as a Result of Myelination,” *Neuroscience. 2nd edition. Sunderland (MA)*, 2001. [Online]. Available: <https://www.ncbi.nlm.nih.gov/books/NBK10921/>. [Accessed: 01-Apr-2020].
- [130] Purves D, Augustine GJ, Fitzpatrick D, *et al.*, “Increased Conduction Velocity as a Result of Myelination,” *neuroscience. 2nd edition. Sunderland (MA): Sinauer Associates*, 2001. [Online]. Available: <https://www.ncbi.nlm.nih.gov/books/NBK10921>. [Accessed: 01-Apr-2020].
- [131] A. D. Reyes, E. W. Rubel, and W. J. Spain, “Membrane properties underlying the firing of neurons in the avian cochlear nucleus,” *J. Neurosci.*, vol. 14, no. 9, pp. 5352–5364, 1994, doi: 10.1523/jneurosci.14-09-05352.1994.
- [132] H. G. Rey, C. Pedreira, and R. Quiñero, “Past, present and future of spike sorting techniques,” *Brain Res. Bull.*, vol. 119, pp. 106–117, 2015, doi: 10.1016/j.brainresbull.2015.04.007.

